Technische Universität München
TUM School of Engineering and Design

A new aerosol profile retrieval algorithm for high-altitude MAX-DOAS measurements and the application to the long-term observation on Zugspitze, Germany

Zhuoru Wang

Vollständiger Abdruck der von der TUM School of Engineering and Design der Technischen

Universität München zur Erlangung eines

Doktors der Ingenieurwissenschaften (Dr.-Ing.)

genehmigten Dissertation.

Vorsitz: Prof. Dr.-Ing. Florian Seitz

Prüfer der Dissertation:

1. Priv.-Doz. Dr.-Ing. habil. Adrian Doicu
2. Prof. Dr.-Ing. habil. Richard H. G. Bamler
3. Prof. Dr. Mark Wenig
    Ludwig-Maximilians-Universität München

Die Dissertation wurde am 17.06.2022 bei der Technischen Universität München eingereicht

und durch die TUM School of Engineering and Design am 04.10.2022 angenommen.

Abstract

In this thesis, a new parametrization multi-axis differential optical absorption spectroscopy (MAX-DOAS) aerosol profile retrieval algorithm was developed to analyze the long-term time series measured by the MAX-DOAS instrument at the Environmental Research Station Schneefernerhaus (UFS), located near Zugspitze. The measurement site is located at an altitude of 2,650 m. As there are no significant emissions at this altitude, it is usually referred as background site.

A cloud screening method was developed to filter out cloudy measurements. This cloud screening method uses the intensity ratio between two wavelength points, also referred as the color index (CI), measured at the zenith direction to determine if the sky is blue (clear) or white (cloudy). The threshold of CI to identify cloudy skies is a function of solar zenith angle and was approximated from the long-term statistic of calibrated CIs. Details of the cloud screening method are presented in Chapter 4. This cloud screening method was applied to the entire measurement period from Feb 2012 to Feb 2016.

As conventional optimal estimation algorithms are not suitable to be applied to high altitude measurements due to the poor signal to noise ratio of the differential slant column densities (DSCDs) of O_4, a new parametrization MAX-DOAS aerosol profile retrieval algorithm dedicated for high altitude measurements was developed and the detail is presented in Chapter 5. The sensitivity of O_4 absorption to several parameters was first investigated. Aerosol profiles were parametrized as the aerosol extinction coefficients of three layers. We defined a profiles set which is assumed to include all possible aerosol profiles under cloud-free conditions. DSCDs of O_4 at 360 and 477 nm were simulated with all the profiles in the profile set and all possible viewing geometries. The simulated data were stored in a look-up table (LUT), which was used as the forward model. In the retrieval of each measurement cycle, simulated O_4 DSCDs corresponding to all the possible profiles were obtained from the LUT. The cost function (χ^2) of each possible profile was then calculated according to the simulated and measured O_4 DSCDs as well as the measurement uncertainties. We performed a comprehensive error analysis to estimate the total uncertainty, in which seven error sources were considered. Valid profiles were selected according to the cost functions. The optimal solution was defined as the weighted mean of all the

valid profiles. Based on the assumption that the LUT covers all possible profiles, we determined O_4 DSCD scaling factors for different elevations and wavelengths. The retrieval algorithm was applied to synthetic measurement data, and the retrieved profiles can reproduce the true profiles. In addition, the retrieval is insensitive to measurement noise. The aerosol optical densities (AODs) retrieved from the long-term measurements correlates well with the sun photometer measurements at the UFS, with correlation coefficients (R) of 0.733 and 0.798 for measurements at 360 and 477 nm, respectively. However, especially in summer the sun photometer AODs are systematically higher than the MAX-DOAS results by a factor of ~2. The MAX-DOAS measurements indicate the aerosol extinction decreases with increasing altitude during all seasons, which agrees with the co-located ceilometer measurements. The results show maximum AOD and maximum Ångström exponent in summer, which is consistent with the observations at an Aerosol Robotic Network (AERONET) station near the UFS.

The zenith measurements during twilight periods were used to determine the total vertical column densities (VCDs) of O_3 and NO_2. Details of the retrieval and total column results can be found in Chapter 6. The air mass factors (AMFs) of O_3 and NO_2 were obtained from LUTs developed at the Belgian Institute for Space Aeronomy (BIRA-IASB). Langley plots (DSCDs versus AMFs) of O_3 and NO_2 were applied to the long-term measurements. For most measurements, the AMFs of O_3 are highly correlated with the DSCDs; while for NO_2, the correlation is on average weaker. For both O_3 and NO_2, the SCDs of the reference spectrum (S_{ref}) derived from individual Langley plots vary in large ranges. The values of $\langle S_{ref} \rangle$ were determined from the long-term results using Gaussian fits. The VCDs of O_3 and NO_2 were then calculated by directly dividing the SCDs (derived by adding $\langle S_{ref} \rangle$ to the twilight DSCDs) by the AMFs. The long-term VCDs of O_3 and NO_2 derived by both Langley plots and direct dividing were compared to satellite measurements. The comparisons show that the VCDs of O_3 measured by MAX-DOAS in both mornings and evenings agree well with the satellite results, and the results calculated using direct dividing agree with the satellite data better than the results derived by Langley plots. For the comparison of NO_2, the agreement is weaker than O_3, regardless of the calculation method. The long-term measurements show that the VCD of O_3 is highest in spring and lowest in autumn, while the VCD of NO_2 is highest in summer and lowest in winter. The VCD of NO_2 has a much larger yearly amplitude than that of O_3.

Zusammenfassung

Im Rahmen dieser Arbeit wurde ein Algorithmus zur Parametrisierung von Aerosol Profilen bei Multi-axis Differential Optical Absorption Spectroscopy (MAX-DOAS) Messungen entwickelt und erfolgreich auf die Zeitreihe der MAX-DOAS Messungen an der Umweltforschungsstation Schneefernerhaus (UFS) nahe der Zugspitze angewendet. Die Station liegt auf 2.650 m Höhe und ist eine Hintergrundstation die normalerweise von unverschmutzter Luft angeströmt wird.

Um wolkenfreie Messungen zu suchen, wurde ein Wolken-Screening-Verfahren entwickelt. Dieses verwendet das Intensitätsverhältnis zwischen zwei Wellenlängen, auch bekannt als Farbindex (CI), der Zenitmessungen. Daran erkannt man, ob der Himmel blau (wolkenlos) ist oder weiß (bedeckt). Wir haben CI-Schwellenwerte für das Wolken-Screening für verschiedene Sonnenzenitwinkel (SZAs) gemäß der langfristigen Häufigkeitsverteilung der kalibrierten CIs bestimmt. Einzelheiten zum Wolken-Screening-Verfahren werden in Kapitel 4 vorgestellt. Dieses Wolken-Screening-Verfahren wurde erfolgreich auf den gesamten Messzeitraum von Februar 2012 bis Februar 2016 angewendet.

In Kapitel 5 stellen wir unseren Algorithmus zur Bestimmung von Aerosolprofilen vor. Wir haben erkannt, dass die bekannten Algorithmen, die auf der optimalen Schätzmethode basieren, nicht für Höhenmessungen geeignet sind. Daher haben wir einen neuen Algorithmus entwickelt, der auf einem Parametrisierungsansatz basiert. Zunächst wurde mittels synthetischer Messdaten die Empfindlichkeit der O_4-Absorption gegenüber unterschiedlichen Parametern untersucht. Aerosolprofile wurden als Aerosol-Extinktionskoeffizienten von drei Höhenschichten parametrisiert. Wir nehmen an, dass der von uns definierte Profilsatz alle notwendigen Aerosolprofile enthält, die die realen Bedingungen unter wolkenfreiem Himmel beschreiben. Die differentiellen schrägen Säulendichten (DSCDs) von O_4 bei 360 und 477 nm wurden mit dem kompletten Profilsatz und allen real auftretenden Betrachtungsgeometrien simuliert. Die simulierten Daten wurden in einer Nachschlagetabelle (LUT) gespeichert. Diese wurde anschließend als Vorwärtsmodell verwendet. Für jeden Messzyklus wurden die simulierte O_4-DSCDs für diese Beobachtungsgeometrie und alle Profile aus der Tabelle abgerufen. Unser Algorithmus bestimmt eine Kostenfunktion (χ^2) für jedes Profils gemäß den simulierten und gemessenen O_4-DSCDs sowie den Messunsicherheiten.

Zur Abschätzung der Gesamtunsicherheit haben wir eine umfassende Fehleranalyse durchgeführt, bei der wir sieben Hauptfehlerquellen berücksichtigt haben. Gültige Profile wurden gemäß den Kostenfunktionen mittels Schwelwerten ausgewählt. Die optimale Lösung berechnet sich als gewichteter Mittelwert aller gültigen Profile. Basierend auf der Annahme, dass die LUT alle realen Aerosolprofile ausreichend beschreibt, haben wir O_4-DSCD-Skalierungsfaktoren für verschiedene Beobachtungsgeometrien und Wellenlängen bestimmt. Die Anwednung des Algorithmus auf synthetische Messdaten ergab eine sehr gute Übereinstimmung mit den wahren Profilen. Die Robustheit unseres Algorithmus gegenüber Messrauschen macht ihn besonders geeignet für die Messungen in großer Höhe. Die aus den Langzeitmessungen gewonnenen aerosoloptischen Dichten (AODs) korrelierten sehr gut mit den Sonnenphotometermessungen an der UFS, mit Korrelationskoeffizienten (R) von 0,733 und 0,798 für Messungen bei 360 bzw. 477 nm. Allerdings liegen die Sonnenphotometer-AODs gerade im Sommer mit einem Faktor ∼2 deutlich über den MAX-DOAS-Ergebnissen. Die MAX-DOAS-Messungen zeigen, dass die Aerosol-Extinktion mit zunehmender Höhe zu allen Jahreszeiten abnimmt, was mit den Messungen des UFS-Ceilometers übereinstimmt. Nach unseren Beobachtungen treten die maximale AOD und der maximalen Ångstrom-Exponenten im Sommer auf. Das stimmt auch mit den Beobachtungen an einer Station des Aerosol Robotic Network (AERONET) in der Nähe der UFS überein.

Abschließend präsentieren wir Messungen der totalen vertikalen Säulendichten (VCDs) von O_3 und NO_2 aus den Zenithbeobachtungen während der Dämmerungsperioden. Die Luftmassenfaktoren (AMFs) von O_3 und NO_2 wurden aus LUTs erhalten, die am Belgischen Institut für Weltraum-Aeronomie (BIRA-IASB) entwickelt wurden. Aus Langley-Korrelationen oder -Plots (DSCDs gegen AMFs) lässt sich die totale VCD bestimmen. Auf die gesamte Zeitreihe angewendet zeigen die Langley-Plots von O_3, dass die AMFs für die meisten Messungen stark mit den DSCDs korrelieren; die Korrelation für NO_2 ist dabei im Durchschnitt schwächer als bei O_3. Sowohl für O_3 als auch für NO_2 variieren die SCDs des Referenzspektrums (S_{ref}), die von Langley-Plots abgeleitet wurde, in großen Bereichen. Mittels Gauß-Fits haben wir aus den einzelnen Referenz SCDs einen Mittelwert $\langle S_{ref} \rangle$ bestimmt. Dann haben wir die VCDs von O_3 und NO_2 berechnet, indem wir die SCDs (abgeleitet durch Addieren von $\langle S_{ref} \rangle$ zu den Dämmerungs-DSCDs) direkt durch die AMFs dividiert haben. Für den Vergleich mit Satellitenbeobachtungen haben wir die Langley-Plots morgens und Abends sowie die Methode der direkten AMF-Division herangezogen. Zusammenfassen können wir

dabei sagen, dass die von MAX-DOAS sowohl morgens als auch abends gemessenen VCDs von O_3 gut mit den Satellitenergebnissen übereinstimmen. Die beste Übereinstimmung mit den Satellitendaten erreichten jedoch die durch direkte Division berechneten Ergebnisse. Beim Vergleich von NO_2 ist die Übereinstimmung unabhängig von der Berechnungsmethode schwächer als bei O_3. Die Langzeitmessungen zeigen, dass die O_3 VCD im Frühjahr am höchsten und im Herbst am niedrigsten ist. Die stratosphärische NO_2 VCD ist hingegen im Sommer am höchsten und im Winter am niedrigsten ist. Die NO_2 VCD hat eine viel größere Jahresamplitude als die von O_3.

Contents

List of Figures

Chapter 1

Introduction

1.1 Atmospheric constituents

Figure 1.1: Vertical temperature profile of the atmosphere (U.S. standard atmosphere 1976).

The earth's atmosphere consists of five major layers, which are distinguished by the average temperature profile with altitude, see Figure 1.1. The lowest layer of the atmosphere is called troposphere, it extends from the earth's surface up to the tropopause. The altitude of the tropopause varies between 10 and 15 km, depending on the latitude and the season. In the troposphere, the temperature decreases with increasing altitude, and rapid vertical mixing of air therefore exists in the layer. The layer above the troposphere is the stratosphere, it extends from the tropopause up to the stratopause. The stratopause is usually located from 45 to 55 km above the earth's surface. The stratosphere is characterized by increasing temperature with altitude and relative slow vertical mixing. The third

layer is the mesosphere which extends from the stratopause up to the mesopause. The mesopause is located at $\sim$80–90 km above ground, and it is the coldest point of the atmosphere. The layer above the mesopause is the thermosphere. The temperature of the thermosphere is very high due to the absorption of short wavelength radiation by nitrogen (N_2) and oxygen (O_2). Photoionization occurs in the lower thermosphere and upper mesosphere, and the ionosphere is therefore formed. The outermost layer of the atmosphere is the exosphere where gas molecules with sufficient energy can escape from gravity. The exosphere is located between 700 and 10000 km.

1.1.1 Troposphere

The troposphere extends from the earth's surface to the altitude of about 8 km at the poles to 18 km at the equator. The troposphere contains $\sim$80% of the total mass of the atmosphere and $\sim$99% of the total mass of water vapor and aerosols (Levine, 1984). It is also the layer where most weather phenomena occur. In the layer, the temperature decreases with increasing altitude at a rate of 6–10 K/km, depending on the humidity (Lampel, 2014). At middle latitudes, the temperature in the troposphere decreases from an average value of $\sim$288 K at sea level to $\sim$220 K at the tropopause (Lydolph et al., 1985). Due to the temperature gradient, strong vertical convection exists in the layer.

The troposphere can be further subdivided into the planetary boundary layer (PBL) and the free troposphere.

1.1.1.1 Planetary boundary layer

The planetary boundary layer (PBL), also known as the atmospheric boundary layer (ABL), is the lowest part of the atmosphere. The behavior of the PBL is directly influenced by its contact with the ground surface. The formation of the PBL is mainly due to the roughness of the ground surface. On the one hand, the obstacles on the surface can directly reduce the wind speed; on the other hand, the obstacles can introduce random turbulence and convection which can also reduce the wind speed (Ahrens and Henson, 2021). In addition, the turbulence can cause vertical mixing between the air moving horizontally at one level and the air at the neighboring levels, which is important in dispersion of pollutants and in soil erosion. The height of the PBL varies depending on the solar energy input and the surface roughness. It varies between 50 m in Polar Regions and up

to 2 km under tropical conditions (Lampel, 2014).

1.1.1.2   Free troposphere

The free troposphere is the layer of the atmosphere between the PBL and the tropopause. The free troposphere is the location of important weather and climate processes. In this layer, horizontal and vertical transport of energy, mass, and momentum take place. In addition, the layer holds greenhouse gases, water vapor and clouds. Therefore, the free troposphere plays an important role in global climate feedback processes. Comparing to the PBL, the free troposphere is less influenced by the ground surface. However, strong turbulent mixing in the PBL couples the surface and free troposphere, resulting in the material and energy vertical transport and redistribution (Jin et al., 2021). Materials in the PBL can also be transported into the free troposphere through large biomass burning such as wild fires, through sand storms in the desert or volcanic eruptions (Jurgschat, 2011).

1.1.2   Stratosphere

The stratosphere is the second layer of the atmosphere. It extends from the tropopause at 8–18 km to the stratopause at the height of $\sim$50 km. The stratosphere contains the ozone layer and it is therefore heated by the solar ultraviolet (UV) radiation. In this layer, the temperature rises with increasing altitude by 2–5 K/km. The temperature ranges from an average of $\sim$220 K at the tropopause to an average of $\sim$260 K near the mesosphere. The temperature inversion strongly reduces air exchange in the vertical direction and makes the stratosphere a stable layer with low convection and mixing. However, winds in the stratosphere can be much stronger than those in the troposphere, the speed can be up to $\sim$60 m/s in the Southern polar vortex.

1.1.3   Aerosols in the atmosphere

Aerosols refer to the fine solid particles or liquid droplets suspending in the air. The diameter of aerosol particles usually varies from 1 nm to tens of micrometers (Seinfeld and Pandis, 2016). Atmospheric aerosols can be from either natural or anthropogenic sources, and can be composed by many different materials and chemicals.

Aerosols are usually classified into two main categories by their size. Particles with diameter varies from 2.5 to $10\,\mu$m are identified as coarse particles (PM_{10}). They are usually found in near roadways and industrial area. Particles with diameter less than $2.5\,\mu$m are identified as fine particles ($PM_{2.5}$). They are mostly likely to be emitted directly from sources.

Atmospheric aerosols play an important role in the climate and weather system. They influence the atmospheric radiation budget directly by absorbing and scattering radiation and indirectly by providing nuclei for cloud formation (Charlson et al., 1992; Hansen et al., 1997; Li and Kou, 2011; Li, 1998; Haywood and Boucher, 2000; Ramanathan and Crutzen, 2003; Bellouin et al., 2005; Heald et al., 2014). In addition, as fine particles are small enough to be inhaled into the lung, atmospheric aerosols have adverse effects on human health (Ghio and Devlin, 2001; Valavanidis et al., 2008; Brook et al., 2010; Li et al., 2010a).

Aerosols are not only released to the atmosphere through direct emissions, but also possible to be secondarily formed through gas to particle conversion and photochemical processes (Hinds, 2012). In the recent decades, a significant increasing amount of anthropogenic aerosols and precursors have been released into the atmosphere, which makes it one of the largest uncertainties in assessments of climate change (IPCC, 2012). Natural and anthropogenic particles emitted into the atmosphere do not only have local impacts, but also influence regions far from the sources through transportation (Schütz et al., 1981; Ganor and Mamane, 1982; Hsu et al., 2009; Wiegner et al., 2011; Almeida-Silva et al., 2013; Lee et al., 2013; Tsai et al., 2014; Zhang et al., 2014; Chan and Chan, 2017; Chan, 2017).

Moreover, the spatial distribution of aerosols varies strongly with time. Therefore, it is crucial to measure the spatial and temporal variations of aerosols in order to provide a better understanding of physical and chemical processes of aerosols in the atmosphere. Aerosols can be measured by in situ instruments such as aerosol mass spectrometer (AMS), differential mobility analyzer (DMA), electrical aerosol spectrometer (EAS), aerodynamic particle sizer (APS), aerodynamic aerosol classifier (AAC), wide-range particle spectrometer (WPS), condensation particle counter (CPC), etc., as well as remote sensing instruments such as sun photometer, ceilometer, Lidar, imaging spectroscopy and multi-axis differential optical absorption spectroscopy (MAX-DOAS). This study mainly focuses on the measurement of aerosol optical extinction profiles by MAX-DOAS. In addition, sun photometer and ceilometer measurements were used as auxiliary data (see Chapters 3 and 5).

1.1.4   Trace gases in the atmosphere

The major chemical components of the atmosphere are nitrogen (N_2), oxygen (O_2), water vapor(H_2O), noble gases (mainly Ar) and carbon dioxide (CO_2). Besides these major constituents, there are many kinds of trace gases with mixing ratios in the order of 1 part per millions parts of air by volume (ppmv, $10^{-6}\,m^3/m^3$) down to less than 1 part per trillions parts of air by volume (pptv, $1^{-12}\,m^3/m^3$). Despite their low abundances, trace gases like ozone (O_3), nitrogen oxides (NO_x) and halogens play important roles in the physical and chemical processes in the atmosphere. These trace species are responsible for many important phenomena in the atmosphere, such as photochemical smog, ozone layer depletion, acid deposition and climate change.

The composition of the atmosphere is changing. The atmospheric concentration of many gaseous pollutants (e.g. SO_2, NO_x) and greenhouse gases (e.g. CO_2, CH_4, N_2O) were reported to be increasing remarkably after the industrial revolution. These changes are altering the physical and chemical processes in the atmosphere and affecting the conditions of lives on the earth.

In this PhD work, the total column densities of NO_2 and O_3 were measured by MAX-DOAS instrument(see Chapter 6).

1.1.4.1   Nitrogen dioxide (NO_2)

Nitrogen dioxide (NO_2) is a reddish-brown gas with a pungent, acrid odor. It is one of the several kinds of nitrogen oxides and also a member of the so-called NO_x family ($NO_x = NO_2 + NO$), as NO_2 and NO can rapidly convert into each other in the atmosphere.

NO_2 has negative influence on human health and ecosystem. It can irritate the mucous membranes of eyes, nose, throat and respiratory tract. Exposure to low concentrations of NO_2 can cause bronchial allergies and aggravate asthma patients' reactions to allergens. In addition, NO_2 can also worsen the condition of patients with chronic respiratory diseases. Prolonged exposure to NO_2 may weaken lung function and reduce the ability of the respiratory system to fight disease. NO_2 is also a precursor of the formation of photochemical smogs, which are more harmful than NO_2 itself.

NO_x are of great importance for chemical processes in the atmosphere as they have a strong impact on the oxidative capacity of the atmosphere by influencing the abundance and distribution of HO_x radicals ($HO_x = OH + HO_2$). Moreover,

they can act as a catalyst in the formation of ozone (O_3) in the troposphere. However, in the stratosphere, NO_x can enhance the degradation of the ozone layer (Crutzen, 1970). NO_x in the atmosphere are mostly removed in the form of nitric acid (HNO_3), which is an important component of acid rain.

The largest source of atmospheric NO_x is combustion. Anthropogenic fossil fuel combustion in industrial activities and traffic plays the most important part in the global inventory of NO_x emission (Lee et al., 1997). NO_x can be generated by either the burning of nitrogenous compounds in the fuel or the reaction of atmospheric nitrogen and oxygen at high temperature. Atmospheric NO_x can also come from soil emission, thunderstorms, etc. In addition, NO_x can diffuse from the stratosphere into the troposphere.

NO_2 can be measured by various techniques such as spectrophotometry, chemi-luminescence (CL), tunable diode laser absorption spectroscopy (TDLAS), Lidar, as well as different kinds of differential optical absorption spectroscopy (DOAS) instruments (e.g., long-path DOAS, zenith sky DOAS, MAX-DOAS, satellite borne DOAS). In the past decade, the global distribution of NO_2 has been measured by several satellites such as Global Ozone Monitoring Experiment (GOME) on board ERS-2 (Burrows et al., 1999) satellite, Scanning Imaging Absorption SpectroMeter for Atmospheric ChartographY (SCIAMACHY) (Bovensmann et al., 1999) on Envisat, Ozone Monitoring Instrument (OMI) (Levelt et al., 2006) on EOS-Aura, GOME-2 (Callies et al., 2000; Munro et al., 2016) on MetOp and Tropospheric Monitoring Instrument (TROPOMI) (Veefkind et al., 2012) on Sentinel-5 Precursor.

1.1.4.2 Ozone (O_3)

Ozone (O_3) is a colorless gas with a distinctively pungent smell. It is a powerful oxidant and plays an important role in the atmospheric chemistry and physics. As shown in Figure 1.2, $\sim$90% of the atmospheric ozone is located in the stratosphere, and the concentration peaks between 20 and 25 km. This layer is called the ozone layer. Ozone in the stratosphere can absorb the radiation in UV-B band (280–315 nm) which is harmful to the ecosystem but cannot be absorbed by other constituents of the atmosphere. The depletion of the ozone layer has been a worldwide concern since the 1970s. However, ozone near ground is harmful to human, animals, crops and other materials. Exposure to high concentrations of ozone can cause physical discomfort and damage to the respiratory system.
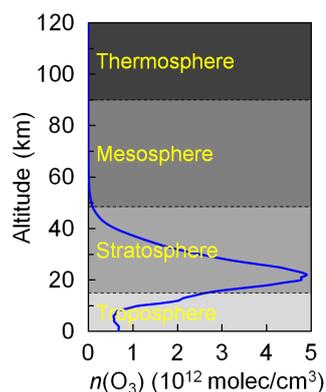
Figure 1.2: Vertical profile of the number density of atmospheric ozone (U.S. standard atmosphere 1976).

Sunlight in UV band can photolyze ozone and generates excited singlet oxygen atoms [$O(^1D)$]:

$$O_3 + h\nu\,(\lambda\,<\,336\,\text{nm}) \longrightarrow O_2 + O(^1D) \tag{1.1}$$
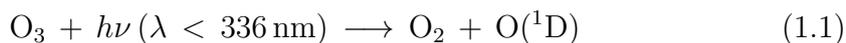
$O(^1D)$ can then combine with water vapor and produce OH radicals:

$$O(^1D) + H_2O \longrightarrow 2OH \tag{1.2}$$

This is the most important source of atmospheric OH radicals, which are important intermediates and catalysts of many atmospheric reactions (Warneck, 1999).

The formation mechanisms of ozone are different in troposphere and stratosphere. Stratospheric ozone is produced by photo dissociation of oxygen molecules (O_2), however, ozone can also be destroyed by photolysis. The net production of ozone depends on the available photons for photolysis and the ambient pressure. This process is called Chapman-cycle, which was first described by Chapman (1930):

$$O_2 + h\nu\,(\lambda\,<\,242\,\text{nm}) \longrightarrow 2O(^3P) \tag{1.3}$$

$$O(^3P) + O_2 + M \longrightarrow O_3 + M \tag{1.4}$$

$$O_3 + h\nu\,(\lambda\,<\,320\,\text{nm}) \longrightarrow O_2 + O(^1D) \tag{1.5}$$

$$O(^1D) + M \longrightarrow O(^3P) + M \tag{1.6}$$

$$O_3 + h\nu\,(\lambda\,<\,1180\,\text{nm}) \longrightarrow O_2 + O(^3P) \tag{1.7}$$

$$2O(^3P) + M \longrightarrow O_2 + M \tag{1.8}$$

$$O(^3P) + O_3 \longrightarrow 2O_2 \tag{1.9}$$
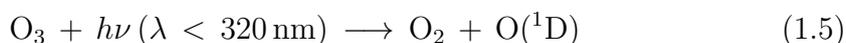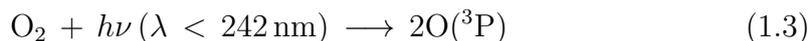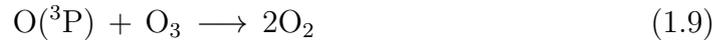
Reactive halogen species (RHS) (e.g., Chlorofluorocarbons) in the atmosphere can shift the equilibrium by introducing another ozone destruction mechanism and hence lead to the depletion of ozone layer.

In the troposphere, ozone is mainly produced by the photochemical reactions of oxygen and nitrogen oxides. NO_2 can be photolysed by photons at low energies, producing NO and atmoic oxygen [$O(^3P)$], which can produce O_3 by the combination with O_2. On the other hand, NO can also destroy ozone, hence there is an equilibrium between $NO_2 + O_2$ and $NO + O_3$:

$$NO_2 + h\nu \longrightarrow NO + O(^3P) \tag{1.10}$$

$$O(^3P) + O_2 + M \longrightarrow O_3 + M \tag{1.11}$$

$$O_3 + NO \longrightarrow NO_2 + O_2 \tag{1.12}$$
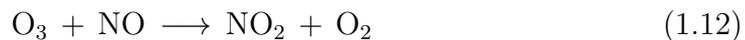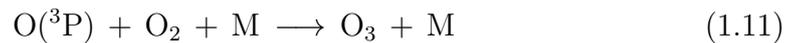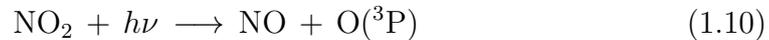
When a compound (e.g., certain volatile organic compounds) which can remove NO exists, the equilibrium will be shifted towards higher ozone levels.

Ozone can be measured by in-situ methods such as spectrophotometry, UV absorption spectroscopy, CL, Fourier transform infrared (FTIR) spectroscopy, as well as remote sensing methods such as different kinds of DOAS. Since the launch of Global Ozone Monitoring Experiment (GOME) (Burrows et al., 1999), the DOAS measurement technique has been successfully applied on satellite-based remote sensing measurements. Several DOAS-based satellite instruments have been launched, such as SCIAMACHY (Bovensmann et al., 1999), Optical Spectrograph and InfraRed Imager System (OSIRIS) (Murtagh et al., 2002), Improved Limb Atmospheric Spectrometer (ILAS) (Sasano et al., 1995), OMI (Levelt et al.,

2006), etc.

1.2   Thesis outline

This study is based on the MAX-DOAS measurements at the Environment Research Station Schneefernerhaus (UFS), Germany.

Chapter 2 presents the principle of DOAS method.

Chapter 3 presents the information about the measurement site and the MAX-DOAS instrument, as well as auxiliary measurements.

Chapter 4 presents a new cloud screening method developed by us.

Chapter 5 presents how the aerosol extinction profiles are retrieved from MAX-DOAS measurements. As we found the commonly used retrieval algorithms are not suitable for the high-altitude site, we developed a new algorithm based on the parametrization approach.

Chapter 6 presents the retrieval of the total VCDs of O_3 and NO_2 from the MAX-DOAS zenith measurements during twilight periods.

Chapter 7 summarizes the results and findings of this work and provides directions for future research.

Chapter 2

Differential Optical Absorption Spectroscopy (DOAS)

DOAS (Differential Optical Absorption Spectroscopy) is a technique for measuring the concentration or amount of trace gases along a light path. It is widely used because of the advantages of high sensitivity, good selectivity, low cost, as well as the possibility to measure certain kinds of trace gases and free radicals which are difficult to be measured by in situ instruments (Sigrist et al., 1994). DOAS technique was first demonstrated in the late 1970s for the simultaneous measurement of CH_2O, O_3, and NO_2 in the atmosphere (Platt et al., 1979; Platt and Perner, 1983). In the past decades, DOAS technique has been applied to the first measurements of many kinds of trace gases and free radicals in the atmosphere, such as OH (Perner et al., 1976), HONO (Perner and Platt, 1979), NO_3 (Platt et al., 1980), BrO (Frieß et al., 2011), IO (Alicke et al., 1999), CHOCHO (Volkamer et al., 2005a), etc.

2.1 Scattering processes in the atmosphere

As the atmosphere consists of molecules and particles, when a light beam travels through the atmosphere, the photons may encounter several kinds of scatterings. The main scattering processes in the atmosphere are Rayleigh and Raman scatterings by air molecules and Mie scattering by aerosol, cloud or ice particles.

2.1.1 Rayleigh Scattering

Rayleigh scattering is the elastic scattering caused by air molecules. Elastic scattering means the scattering does not change the photon's energy (i.e., the wavelength or frequency). In spectroscopy studies, Rayleigh scattering is usually treated as an absorption process, although it is not really an absorption process. The cross section of Rayleigh scattering $\sigma_R(\lambda)$ in cm^2 can be described as (Rayleigh, 1899):

$$\sigma_R(\lambda) = \frac{24\pi^3}{\lambda^4 N_{air}^2} \cdot \frac{[n_0^2(\lambda) - 1]^2}{[n_0^2(\lambda) + 2]^2} \cdot F_K(\lambda), \tag{2.1}$$

where λ is the wavelength in cm, $n_0(\lambda)$ is the wavelength-dependent index of the refraction of air, N_{air} is the number density of air in $molec/cm^3$, and $F_K(\lambda) \approx 1.061$ is a correction factor for the anisotropy of air molecules. Since $n_0 \approx 1$,

$$\sigma_R(\lambda) \approx \frac{8\pi^3}{3\lambda^4 N_{air}^2} \cdot [n_0^2(\lambda) - 1]^2 \cdot F_K(\lambda). \tag{2.2}$$

Note that $[n_0(\lambda) - 1] \propto N_{air}$, therefore $[n_0^2(\lambda) - 1] \approx 2[n_0(\lambda) - 1] \propto N_{air}$, hence $\sigma_R(\lambda)$ is almost independent of N_{air}.

For simple estimations, $\sigma_R(\lambda)$ can be calculated as

$$\sigma_R(\lambda) \approx \sigma_{R0} \cdot \lambda^{-4}, \tag{2.3}$$

where $\sigma_{R0} \approx 4.4 \times 10^{-16} cm^2 \cdot nm^4$ for air.

Rayleigh scattering is very sensitive to the wavelength, and the scattering is strong for short wavelength. As blue light has shorter wavelength than red light, the clear sky is blue.

2.1.2 Mie Scattering

Mie scattering refers to the elastic scattering of radiation by particles. Radiation can be both absorbed and scattered by particles in the atmosphere, and these processes are described by the absorption coefficient $\varepsilon_a(\lambda)$ and the scattering coefficient $\varepsilon_s(\lambda)$:

$$dI_a = -I(\lambda) \cdot \varepsilon_a(\lambda) \cdot ds, \tag{2.4}$$

$$dI_s = -I(\lambda) \cdot \varepsilon_s(\lambda) \cdot ds, \tag{2.5}$$

where $I(\lambda)$ is the radiation flux, and $dI(\lambda)$ is the change of $I(\lambda)$ after passing through a layer of aerosol of thickness ds. The single scattering albedo of the aerosol is defined as:

$$A_{\mathrm{S}} = \frac{\varepsilon_{\mathrm{s}}(\lambda)}{\varepsilon_{\mathrm{a}}(\lambda) + \varepsilon_{\mathrm{s}}(\lambda)}, \qquad (2.6)$$

And the Mie scattering extinction coefficient is defined as:

$$\varepsilon_{\mathrm{M}}(\lambda) = \varepsilon_{\mathrm{a}}(\lambda) + \varepsilon_{\mathrm{s}}(\lambda). \qquad (2.7)$$

Mie scattering was first described by Gustav Mie (Mie, 1908). It was defined as the interaction of light with particles of sizes comparable to the wavelength of the incident light. It can be regarded as the radiation resulting from a large number of coherently excited molecules in a particle. As the linear dimension of the particle is comparable to the wavelength of the incident light, interference effects occur. The most noticeable differences of Mie scattering compared to Rayleigh scattering are the much weaker wavelength dependence (typically proportional to $\lambda^{-1.3}$) and a strong dominance of the forward direction in the scattered light. Therefore, the cloudy sky is white or gray.

The calculation of the Mie scattering cross-section can be very complicated, however, the Mie theory has been well developed and a number of numerical models can calculate the scattering phase functions and extinction coefficients for given aerosol types and particle size distributions (van de Hulst, 1980). The computational effort can be greatly reduced by the introduction of a parametrized expression of the scattering phase function, which only depends on a few observable parameters. The most commonly used parametrized expression is the Henyey-Greenstein (Henyey and Greenstein, 1941) function:

$$p(\theta) = \frac{1}{4\pi} \cdot \frac{1 - g^2}{[1 + g^2 - 2g \cdot \cos(\theta)]^{3/2}}, \qquad (2.8)$$

where $p(\theta)$ is the scattering probability for scattering angle θ, which is the angle between the directions of the photon before and after a scattering event. θ is 0 and π for forward and backward scattering, respectively. g is the asymmetry factor, which is defined as

$$g \equiv \langle \cos(\theta) \rangle = \int_0^\pi \cos(\theta) \cdot p(\theta) \cdot 2\pi \cdot \sin(\theta) \cdot d\theta. \qquad (2.9)$$

The Henyey-Greenstein phase function only depends on the asymmetry factor. For isotropic scattering, $p(\theta)$ is constant, and $g = 0$. For complete forward scattering, g would be 1. Typical values of g for tropospheric aerosols are between 0.6 and 0.7. Parameters for typical aerosol scenarios can be found in the LOWTRAN database (Isaacs et al., 1987), which includes the extinction coefficients and the asymmetry factors, as well as their spectral dependence.

Particles of different dimensions show different wavelength dependencies. The wavelength dependence is expressed by the Ångström coefficient α:

$$\varepsilon_{\mathrm{M}}(\lambda) = \varepsilon_{\mathrm{M0}} \cdot \lambda^{-\alpha}, \tag{2.10}$$

α is inversely related to the mean aerosol particle radius. α typically varies between 0.5 and 2.5, with an average value of $\sim$1.3 (Ångström, 1930), however, very low values were found at certain high-altitude sites (see Section 5.11.5).

2.1.3 Raman Scattering

Raman scattering is the inelastic scattering of photons by matter, which means there is both an exchange of energy and a change in the light's direction during the scattering process. The photon either transfers a part of its energy to the molecule (Stokes lines, $\Delta J = +2$, S-branch) or takes over a part of the molecule's excitation energy (Anti-Stokes, $\Delta J = -2$, O-branch). If only the rotational excitation is affected ($\Delta \nu = 0$), the scattering is called rotational Raman scattering (RRS). On the other hand, if the vibrational state also changes ($\Delta \nu = \pm 1$), then the scattering is called rotational vibrational Raman scattering (RVRS).

Only discrete amounts of energy given by the difference between the discrete excitation levels can be transferred between the photons and the molecules. For air molecules (mainly N_2 and O_2), RRS frequency shifts of up to $\pm 200\,\mathrm{cm}^{-1}$ occur; for RVRS, a vibrational shift of $\pm 2331\,\mathrm{cm}^{-1}$ for N_2 and $\pm 1555\,\mathrm{cm}^{-1}$ for O_2 needs to be added (Burrows et al., 1996; Haug, 1996; Sioris and Evans, 1999). As the RRS is one order of magnitude stronger than the RVRS, it dominates the Raman scattering and the RVRS can be neglected in calculating the Ring spectrum (see Section 2.5.2). Comparing to Rayleigh scattering, Raman scattering accounts to a few per cent and depends on the wavelength (Haug, 1996). As Raman scattering does not play an important role in the radiative transfer, it is not taken into account in the radiative transfer model (see Section 5.1.2) in this study.

2.2   Principle of DOAS method
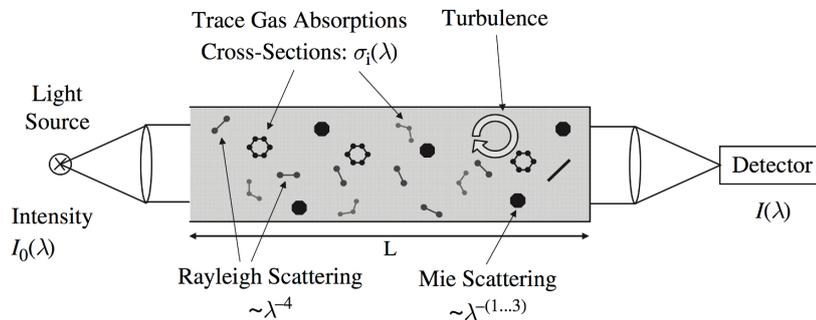
Figure 2.1: Sketch of an experiment to measure trace gas absorptions in the open atmosphere (Platt and Stutz, 2008).

DOAS method is an application of the Beer-Lambert Law, which describes the attenuation of light to the properties of the material through which the light is travelling. As illustrated in Figure 2.1, light intensity (denoted as a function of wavelength) can be changed (usually decreased) mainly due to molecular absorption, Rayleigh scattering and Mie scattering. The change can be described as the following equation:

$$\ln\left[\frac{I_0(\lambda)}{I(\lambda)}\right] = \int_0^L \left[\sum \sigma_i(\lambda) \cdot n_i(s) + k_{\mathrm{R}}(\lambda, s) + k_{\mathrm{M}}(\lambda, s) + b(\lambda)\right] \mathrm{d}s, \quad (2.11)$$

where λ denotes the wavelength, $I_0(\lambda)$ refers to the intensity of the incident light at the wavelength λ, while $I(\lambda)$ is the intensity of the transmitted light. The left part of the equation is also called optical density and can be denoted as $D(\lambda)$. The right part of the equation refers to the absorption, where L is the length of the light path, σ_i is the molecular absorption cross section of the ith absorption species, $n_i(s)$ is the number density of the ith absorption species at the position s, k_{R} and k_{M} are the coefficients of Rayleigh scattering and Mie scattering, respectively, and b represents the instrumental effects.

The key idea of DOAS method is to filter out the broad band structures (i.e., the structures vary slowly with the wavelength) from both sides of Eq. (2.11) and derive the absorption information only from the narrow band structures (i.e., the structures vary fast with the wavelength). The separation is done with a mathematical filter, usually by dividing both parts by a polynomial of appropriate

degree and/or applying a high-pass filter (Stutz and Platt, 1996). In the right part of Eq. (2.11), k_R, k_M and b are broad band structures and can be filtered out. Molecular absorption cross sections consists of both broad band and narrow band structures, which can be described as:

$$\sigma_i(\lambda) = \sigma_{0,i}(\lambda) + \sigma_i'(\lambda), \qquad (2.12)$$

where σ_0 represents the broad band structure, while σ' refers to the narrow band (or differential) structure. Correspondingly, the optical density can also be described as the sum of broad band and narrow band parts:

$$D(\lambda) = \ln\left[\frac{I_0(\lambda)}{I(\lambda)}\right] = D_0(\lambda) + D'(\lambda), \qquad (2.13)$$

where D_0 represents the broad band part, and D' is the narrow band part, i.e., differential optical density. After broad band structures are removed from both sides of Eq. (2.11) in the same way, the left part would become the differential optical density, and only the differential molecular absorptions would remain in the right part. The relation between them can be described as:

$$D'(\lambda) = \int_0^L \left[\sum \sigma_i'(\lambda) \cdot n_i(s)\right] ds. \qquad (2.14)$$

As shown in Figure 2.2, many kinds of trace gas molecules have optical absorption cross sections in UV – VIS (visible) band. The accurate value of $\sigma(\lambda)$ can be determined in the laboratory, and the data of common atmospheric species are available from literature. DOAS method takes advantage of the characteristic differential absorption cross sections. In DOAS measurements, $I_0(\lambda)$ and $I(\lambda)$ are measured by the same spectrometer, and D' is then calculated. With the absorption cross sections of the major absorbers included in the retrieval, the concentration or amount of each absorber can be determined by least-square fitting.

In DOAS measurements, the light intensities at a number of individual wavelengths are measured, therefore the measurement result is less influenced by the spectrum noise comparing to the traditional spectroscopy measurements methods which are based on the measurements at only one or a few wavelengths. As the differential absorption cross section of each absorption species is unique like a fingerprint, the retrieval has good selectivity. In addition, since the broad band absorptions are filtered out, the measurement is hardly influenced by scattering
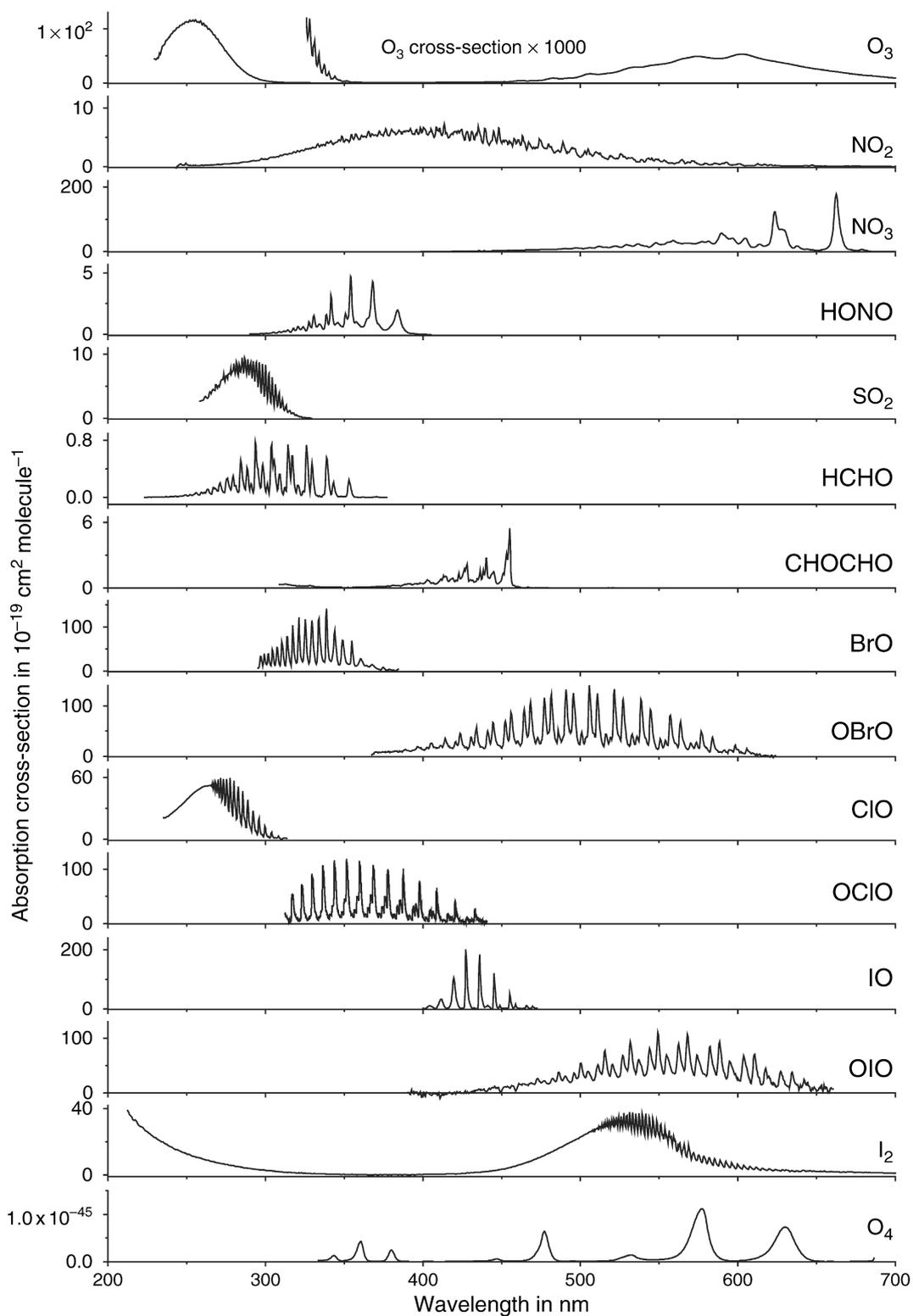
Figure 2.2: Absorption cross sections of some molecules (Platt and Stutz, 2008).

or instrument function.

2.3   Example of DOAS evaluation

An example of DOAS evaluation is shown in Figure 2.3. In the case, the concentration of SO_2 is to be retrieved from the spectra measured by an active long-path DOAS instrument. The instrument uses a Xenon short-arc lamp as the light source, and has a fixed light path of 1.36 km in the atmosphere. The fitting window is selected as 291.5–305 nm, since SO_2 has strong differential absorption in this band and it can be hardly influenced by other atmospheric species (see Figure 2.2). Panel (a) shows the spectra of the light before and after it travels through the atmosphere, which are I_0 (purple curve) and I (blue curve), respectively. Each spectrum is an array of light intensities at 54 wavelength points, as the fitting window covers 54 channels of the photodetector of the spectrometer. Then, the optical density D can be calculated by taking the logarithm of I_0/I, shown as the blue curve in Panel (b). By applying a $3^{\rm rd}$ order polynomial regression to D and λ, D_0 — the broad band optical density — is derived, shown as the gray curve in Panel (b). Correspondingly, the difference between D_0 and D is the differential optical depth D', shown as the blue curve in Panel (c).

On the other hand, the cross section of SO_2 molecules obtained from literature (Vandaele et al., 2009) is shown in Panel (d). As the resolution of the standard cross section is much higher than the spectrometer of the DOAS instrument, it is first convolved with the instrument function, so that it is comparable to the measured optical depth. The convolved standard cross section is then converted to the reference optical density $D_{\rm ref}$, which refers to the optical density corresponding to an average SO_2 VMR of 1 ppbv (part per billion by volume, i.e., $10^{-9}\,{\rm m}^3/{\rm m}^3$) and the same light path of the instrument (1.36 km). As the number density of air at 273.15 K and 1 atm is 2.6868×10^{25} molec/m³, the number density corresponding to 1 ppbv is

$$n_{\rm ref} \,=\, 2.6868 \times 10^{25} \cdot 10^{-9} \,=\, 2.6868 \times 10^{16}\ {\rm molec/m}^3. \qquad (2.15)$$

Therefore the conversion factor between the reference optical density $D_{\rm ref}$ and the convolved standard cross section $\sigma_{\rm conv}$ (in cm²/molec) is
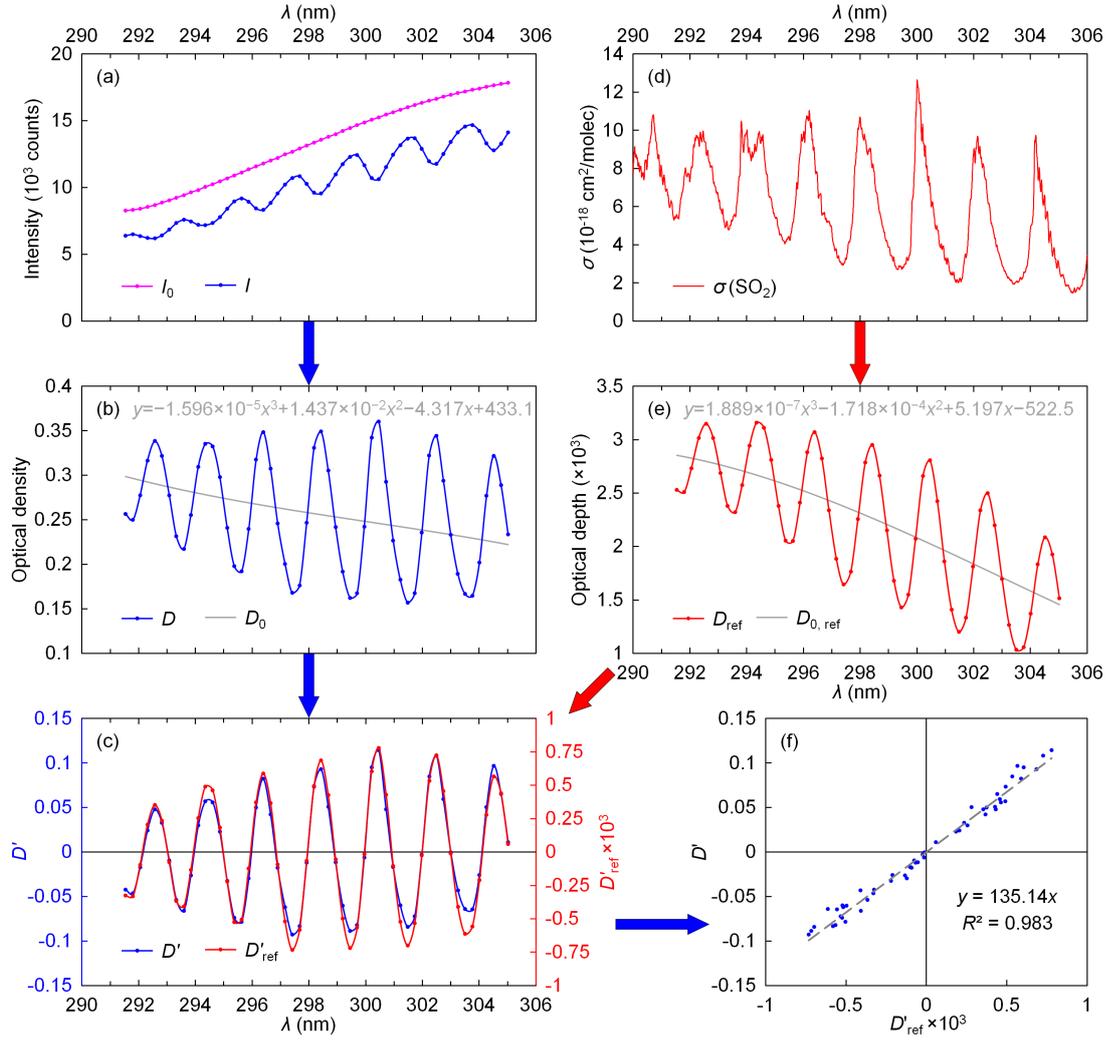
Figure 2.3: An example of DOAS evaluation, the process of the retrieval of SO_2 concentration from an active long-path DOAS measurement. (a) Spectra of the light before (I_0) and after (I) transmitting in the air. (b) Optical depth (D) and its broad band part (D_0). The equation shown in the panel is the equation of D_0. (c) Differential optical depth (D') and reference differential optical depth (D'_{ref}, which refers to the differential optical density corresponding to an average SO_2 VMR (volume mixing ratio) of 1 ppbv and the same light path of the instrument). (d) Standard cross section (σ) of SO_2 obtained from literature. (e) Reference optical depth (D_{ref}) and its broad band part ($D_{0,ref}$). The equation shown in the panel is the equation of $D_{0,ref}$. (f) Scattered plot of D' against D'_{ref} and the linear regression result.

$$
\begin{aligned}
\frac{D_{ref}}{\sigma_{conv}} &= L \cdot n_{ref} \\
&= 1.36 \, \text{km} \, \cdot \, 2.6868 \times 10^{16} \, \text{molec/m}^3 \\
&= 1.36 \times 10^5 \, \text{cm} \, \cdot \, 2.6868 \times 10^{10} \, \text{molec/cm}^3 \\
&= 3.654 \times 10^{15} \, / (\text{cm}^2/\text{molec}).
\end{aligned}
\tag{2.16}
$$

D_{ref} is shown as the red curve in Panel (e). Using the same method as D_0 and D', the broad band part $D_{0,\text{ref}}$ and narrow band part D'_{ref} are separated from D_{ref}, shown as the gray curve in Panel (e) and the red curve in Panel(c), respectively. As SO_2 is the only major absorber in this wavelength range, it can be seen that $D'(\lambda)$ and $D'_{\text{ref}}(\lambda)$ have similar shapes, but only different 'amplitudes'. In Panel (f), the data points of D' are plotted against the data points of D'_{ref}. The linear regression shows very good correlation ($R^2 = 0.983$), and the slope of the trend line is 135.14, which implies that the average SO_2 VMR along the light path is 135.14 times as high as the reference, i.e., 135.14 ppbv.

In most cases, the fitting process is more complicated than this example. For instance, more than one absorbers may contribute to the absorption in the DOAS fitting range, and both spectra and cross sections can be slightly shifted or stretched due to the change of temperature or pressure. There can be quite a few variable parameters in actual DOAS fittings, however, the key idea is still the same — to make the fitting residual as low as possible. The fitting window also need to be optimized for a better retrieval.

2.4 Applications of DOAS technique

Based on the basic principle of DOAS method, several different types of DOAS experimental setups have been developed during the past decades. According to the light source, the experimental setups can be distinguished to active and passive DOAS.

Active DOAS instruments use man-made light sources. They have the advantage that the light can be available all the time, while passive measurements rely on natural light sources which are only available under certain circumstances, e.g. daytime, cloud free condition, etc. In addition, the spectral range of the man-made light sources can be customized for different applications. For example, there is virtually no available sunlight below 280 nm on the ground due to the absorption of the atmosphere, and therefore measurement in the deep UV range is only available by using man-made light source.

Passive DOAS instruments use natural light sources, usually the sun. The main advantage of passive DOAS is the ability to measure trace gases at unreachable areas such as the free troposphere and the stratosphere. In addition, passive DOAS instruments are able to measure the total column densities of trace gases and radicals.

2.4.1   Long-path DOAS (LP-DOAS)

Long-path DOAS (LP-DOAS) is the simplest experimental setup of active DOAS. It measures the concentration of trace gases in the troposphere by using a man-made broad wavelength band light source and measures the optical absorption over a designed long optical path in the open atmosphere. The length of the optical path varies from several hundred meters up to several kilometers. LP-DOAS technique was first demonstrated in the late 1970s for measuring the concentration of atmospheric CH_2O, O_3 and NO_2 (Platt et al., 1979; Platt and Perner, 1983).
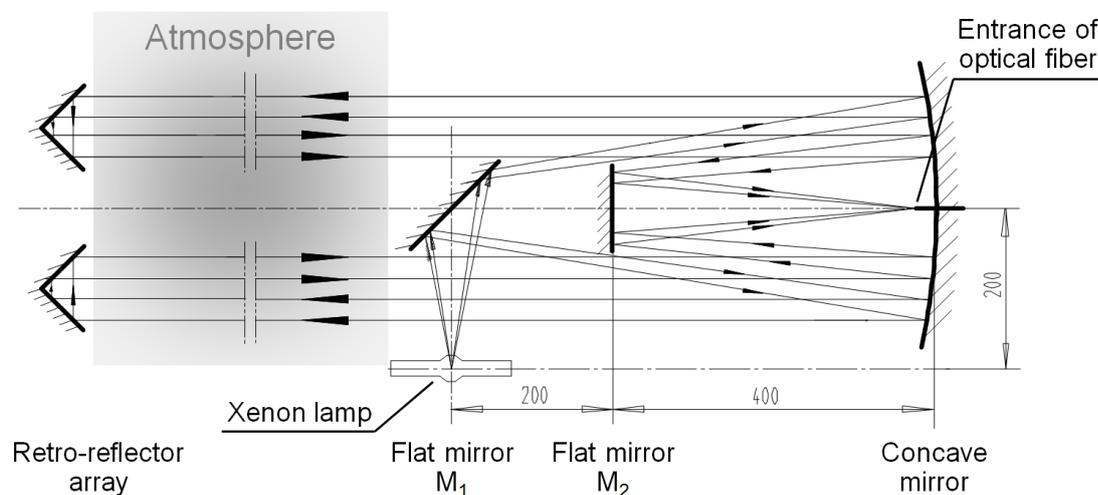
Figure 2.4: Schematic diagram of a coaxial LP-DOAS setup with combined transmitting and receiving optics in a single telescope (Wang et al., 2011).

Typical LP-DOAS instrument includes a transmitting unit which consists of an artificial light source and an emitting telescope, as well as a receiving unit which usually regards to a receiving telescope and a spectrograph. In the transmitting unit, light from the light source is coupled to the emitting telescope and sent out to the atmosphere. In the receiving unit which is at the end of the light path, the transmitted light is collected by the receiving telescope and redirected to the spectrometer. In practice, the transmitting and receiving units are usually located at the same side, and the light beam is folded back by a retro-reflector or a retro-reflector array. This design is called coaxial LP-DOAS. Figure 2.4 shows the schematic diagram of a coaxial LP-DOAS (Wang et al., 2011). The flat mirror M_1 and the concave mirror constitutes a Newtonian telescope. The xenon
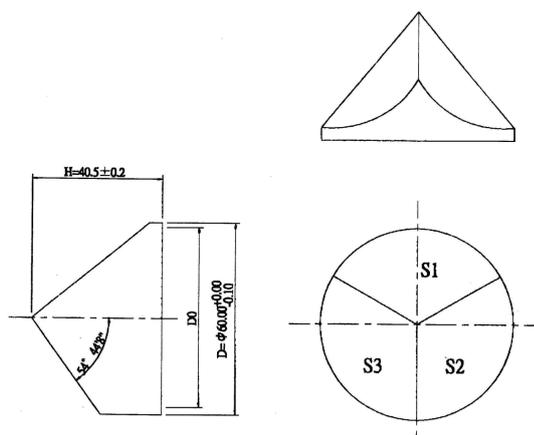
Figure 2.5: Drawing of a quartz corner cube reflector.

short-arc lamp is located at the focal point of the telescope, therefore the light is collimated to a parallel ray and projected to the retro-reflector array. The retro-reflector array consists of a few corner cube reflectors. As shown in Figure 2.5, each corner cube reflector is a quartz-glass prism with three perpendicular intersecting flat surfaces. Light can be reflected by the surfaces by total internal reflection, and its shape ensures that the reflected ray is parallel to the incident ray, but not in the same way. Therefore, the reflected light is still in a parallel ray which can reach the telescope, but would not return to the lamp; instead, some of the returned light can be reflected by the flat mirror M_2. M_2 folds the light focused by the concave mirror back, so that the returned light would not be blocked by M_1. The entrance of optical fiber is at the focal point, and the returned light is transmitted to the spectrometer. The design of combining the transmitting and receiving telescopes together can not only lower down the cost of the instrument, but also simplify the maintenance of the instrument, as only the retro-reflector is installed at the remote side. In addition, coaxial LP-DOAS allows the measurement of the spectrum of the light source (I_0) by simply laying a retro-reflector near the telescope.

2.4.2   Cavity-enhanced DOAS (CE-DOAS)

LP-DOAS measures the optical absorption over a long optical path in the open atmosphere, however, the reliance on the long optical path makes it infeasible for small-scale measurements such as indoor measurements and mobile measurements. In order to overcome such limitation, another kind of active DOAS in-

strument, Cavity-enhanced DOAS (CE-DOAS) was developed, which provides an alternative option for small-scale measurements (Platt et al., 2009). CE-DOAS produces a long light path with an optical resonator, so as to enhance the absorption signal within a limited space (Engeln et al., 1998; Brown, 2003; Ball et al., 2004; Fiedler et al., 2003).
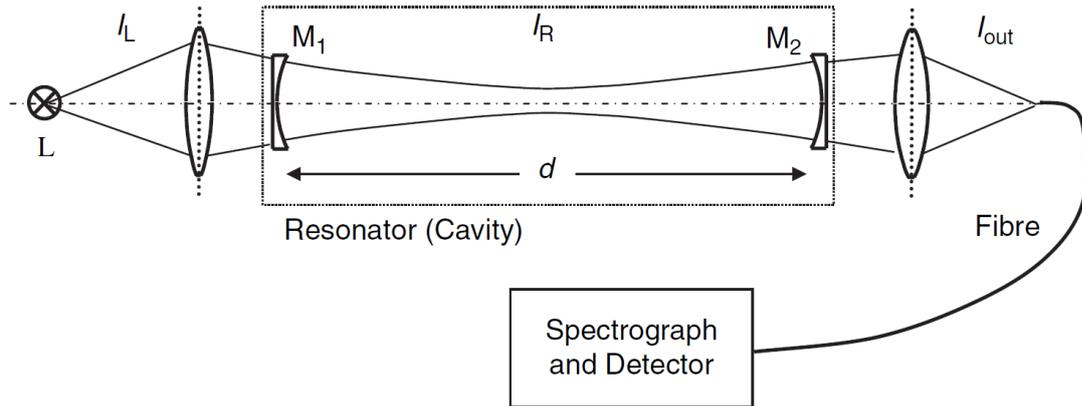
Figure 2.6: Sketch of a CE-DOAS system (Platt and Stutz, 2008).

As shown in Figure 2.6, a typical CE-DOAS system consists of a light source, an optical resonator and a spectrometer. The optical resonator consists of two mirrors with reflectivity R. Light from the light source (intensity denoted as I_L) is coupled into the resonator through a focusing lens at one side of the resonator (M_1), and only a fraction of $1 - R$ of the light will enter the resonator. If other losses are neglected, light in the resonator would be reflected $1 / (1 - R)$ times in the cavity. Half of the light will leave the resonator through the mirror at the other side (M_2) and be coupled to the spectrometer for spectra measurement. The intensity of the transmitted light can be described as

$$I_{\text{out}}(\lambda) = I_L(\lambda) \cdot \frac{1 - R(\lambda)}{2}. \tag{2.17}$$

If additional (broad band) extinction is considered, the average length of the absorption path would be:

$$\overline{L} = \frac{d}{(1 - R) + \varepsilon_B \cdot d}, \tag{2.18}$$

where ε_B denotes the broadband extinctions due to Mie and Rayleigh scattering as well as trace gas broad band absorption, and d is the length of the resonator.

Presently, mirrors with $R > 0.9999$ can be manufactured. By using such mirrors with $d = 1\,\mathrm{m}$, the average light path $\overline{L}$ would be larger than $10\,\mathrm{km}$, and the intensity of the transmitted light (I_{out}) would be about 5×10^{-5} times of the initial light intensity (I_{L}). The transmitted fraction seems to be small but it is indeed comparable to LP-DOAS in the open atmosphere. In order to have accurate measurements, the effective optical path length of CE-DOAS need to be calibrated, e.g. by measuring an absorbing gas sample with known concentration (Langridge et al., 2006; Venables et al., 2006).

2.4.3 Zenith scattered light DOAS (ZSL-DOAS)
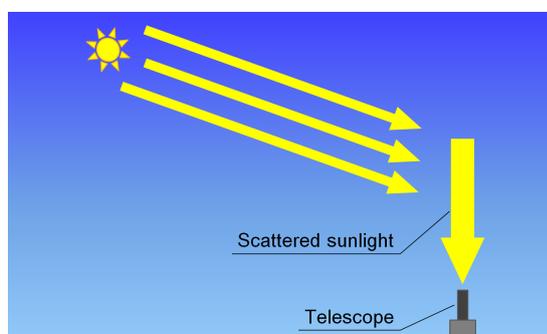
Figure 2.7: Schematic diagram of zenith scattered light DOAS.

Zenith scattered light DOAS (ZSL-DOAS) is the simplest application of passive DOAS. ZSL-DOAS measures the spectra of scattered sunlight at the zenith direction. A schematic diagram of zenith scattered light DOAS is shown in Figure 2.7. The system consists of a receiving telescope pointing to the zenith and a spectrometer. The light collected by the telescope is transmitted to the spectrometer through an optical fiber. In order to cover a wider wavelength range, some ZSL-DOAS instruments have more than one spectrometer (Hönninger and Platt, 2002).

ZSL-DOAS has several advantages in atmospheric measurements. First, the experimental setup is relatively simple, as it consists of only a spectrograph and a receiving telescope, and adjustment of the telescope is not required. Second, tropospheric trace species can be measured, even if they are distributed over the entire troposphere. Third, ground-based zenith DOAS measurements are sensitive to trace gases in the stratosphere even in the presence of cloud cover. However, these advantages come along with the rather complicated radiative

transfer calculations of the effective optical path in the atmosphere. In addition, correction has to be made to compensate for the effects due to light scattering process in the atmosphere.

ZSL-DOAS has been widely used for the measurement of vertical column densities (VCDs) of trace gases and free radicals in the past a few decades, such as O_3, NO_2 (Pommereau, 1982; Mount et al., 1987; Wahner et al., 1990; Johnston et al., 1992; Chen et al., 2009; Roscoe et al., 2010; Constantin et al., 2013), NO_3 (Sanders et al., 1987; Solomon et al., 1989a), OClO (Solomon et al., 1987a; Schiller et al., 1990; Perner et al., 1991; Kreher et al., 1996; Otten et al., 1998), BrO (Solomon et al., 1989b; Kreher et al., 1997; Eisinger et al., 1997; Richter et al., 1999; Hendrick et al., 2007) and O_4 (Sarkissian et al., 1991; Erle et al., 1995; Wang et al., 2012a).

Since ZSL-DOAS instruments can be made portable and do not rely on fixed light paths, they can be installed on vehicles or ships, and hence mobile measurements are available. Mobile ZSL-DOAS measurements can provide information on the spatial distribution of air pollutants (Wu et al., 2013; Zhu et al., 2016). Moreover, the total pollutant emission from a certain region can be estimated from circular mobile-DOAS measurements in combination with meteorological data (Wang et al., 2012b).

Chapter 6 of this thesis presents the retrieval of the total VCDs of O_3 and NO_2 from the zenith measurements of the MAX-DOAS instrument at the UFS. In such measurements, the MAX-DOAS is virtually used as a ZSL-DOAS.

2.4.4   Multi-axis DOAS (MAX-DOAS)

Multi-axis differential optical absorption spectroscopy (MAX-DOAS) is the variant of ZSL-DOAS. MAX-DOAS measures the spectra of scattered sunlight at not only the zenith direction, but also off-zenith directions. Since measurements at different observation angles have different sensitivities to trace gases at different altitudes, MAX-DOAS can provide more information about the vertical distribution of trace gases comparing to ZSL-DOAS.

A simplified MAX-DOAS measurement sketch is illustrated in Figure 2.8. Typical MAX-DOAS instrument consists of a spectrometer and a receiving telescope equipped with one or two stepper motors, so that the viewing direction of the telescope can be precisely adjusted. Usually, the telescope scans in a predefined cycle which includes several different viewing angles, and each cycle takes
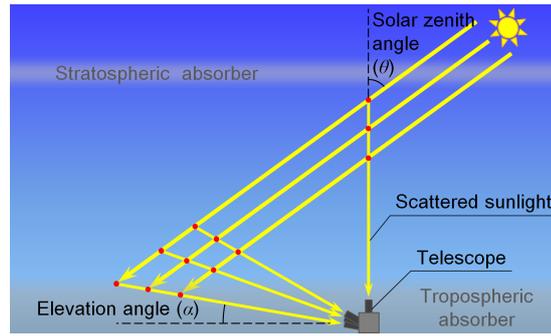
Figure 2.8: Schematic diagram of MAX-DOAS measurement in the single scattering case. The red points indicate scattering events along the line of sight of the telescope.

a few minutes. Since it is impossible to measure the spectrum of the initial sunlight, typical MAX-DOAS retrieval treats the zenith spectrum as the reference spectrum (I_0), while the spectra measured at other elevations (I) are divided by the zenith reference spectrum before applying the DOAS retrieval. Subsequently, a logarithm is taken to convert the quotient to the optical density. By applying DOAS evaluation to the optical density, the differential slant column densities (DSCDs, ΔS) of trace gases are derived, which refer to the differences between the slant column densities (SCDs, S) along the off-zenith and the zenith measurements. According to the definitions of SCD and DSCD, the DOAS equation Eq. (2.14) can be written as:

$$D'(\lambda) = \sum \sigma_i'(\lambda) \cdot \Delta S_i, \qquad (2.19)$$

and

$$\Delta S_i = S_i - S_{\text{ref},i} = \int_0^L n_i(s)\mathrm{d}s - \int_0^{L_{\text{ref}}} n_{\text{ref},i}(s)\mathrm{d}s, \qquad (2.20)$$

where S_i, L and n_i are the SCD, light path length and number density of the ith absorber of the off-zenith measurement, while $S_{\text{ref},i}$, L_{ref} and $n_{\text{ref},i}$ are those of the zenith reference measurement.

The red points in Figure 2.8 illustrate the scattering of the sunlight in the line of sight of the MAX-DOAS telescope. In this figure, the single scattering case is assumed, i.e., each photon is scattered only once in the atmosphere. In reality, multiple scattering may also occur. The upper and lower gray layers in the figure refer to atmospheric absorbers in the stratosphere and the troposphere,

respectively. As illustrated in the figure, if the zenith and off-zenith spectra are measured at the same time or within a short time span (e.g., in the same scanning cycle), their absorptions in the stratosphere are supposed to be the same. Therefore, the stratospheric absorptions are canceled in the above-mentioned DSCDs, and the DSCDs are only sensitive to tropospheric absorptions. In addition, since the scattered sunlight observed at lower elevations usually has longer light paths in the troposphere, the absorption intensities of trace gases are stronger at lower elevations and hence lead to larger DSCDs.

As DSCDs are affected by the effective light path in the atmosphere, they cannot directly reflect the real concentration or amount of atmospheric trace gases and need to be converted. The effective light path in the atmosphere depends on the radiation transfer in the atmosphere in which aerosols play an important role. Accurate retrieval of aerosol information requires the inversion of a series of underlying radiative transfer equations which cannot be linearized. Commonly, aerosol information is retrieved by fitting the forward simulated DSCDs of an absorber with well-known and stable concentration profile — the oxygen dimer complex, O_4 — to the measurements (Wagner et al., 2002; Hönninger et al., 2004; Wagner et al., 2004; Sinreich et al., 2005; Frieß et al., 2006). This study is based on the MAX-DOAS measurements at the UFS, and the principle of aerosol optical extinction profile retrieval is presented in detail in Chapter 5.

As the experimental setup of MAX-DOAS is relatively simple and inexpensive, it has been widely used to measure the vertical distribution of atmospheric aerosols and trace gases in the past two decades (e.g., Hönninger et al., 2004; Irie et al., 2008; Li et al., 2010b; Clémer et al., 2010; Frieß et al., 2011; Halla et al., 2011; Irie et al., 2011; Vlemmix et al., 2011; Wagner et al., 2011; Li et al., 2013; Ma et al., 2013; Wang et al., 2014a; Chan et al., 2015; Jin et al., 2016; Wang et al., 2016; Chan et al., 2017).

2.4.5   Satellite borne DOAS

The DOAS measurement technique has also been applied in satellite-based remote sensing measurements. Several DOAS-based satellite instruments have been launched in the past decades, such as the Global Ozone Monitoring Experiment (GOME) (Burrows et al., 1999), the Scanning Imaging Absorption Spectrometer for Atmospheric Chartography (SCIAMACHY) (Bovensmann et al., 1999), the Optical Spectrograph and InfraRed Imager System (OSIRIS) (Murtagh et al.,

2002), the Improved Limb Atmospheric Spectrometer (ILAS) (Sasano et al., 1995)
and the Ozone Monitoring Instrument (OMI) (Levelt et al., 2006).
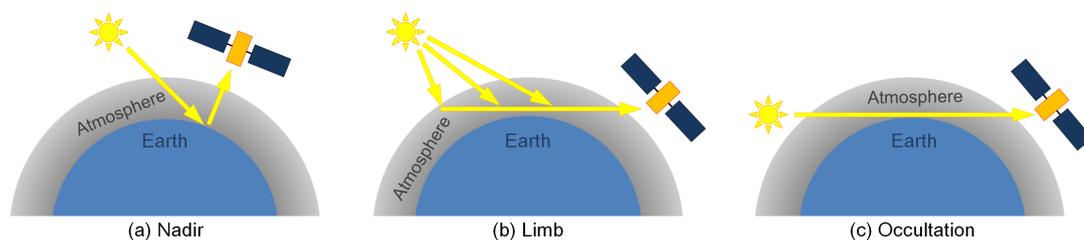
Figure 2.9: Different viewing geometries of satellite measurements, (a) Nadir,
(b) Limb, and (c) Occultation.

As shown in Figure 2.9, different viewing geometries are used in satellite-
based DOAS observations. The most commonly used satellite viewing geometry
is the nadir view (Figure 2.9a), which means looking down from space towards
the earth's surface in the nadir direction and measuring the reflected solar ra-
diation from the surface or atmosphere of the earth. Nadir observation can be
used to measure the column densities of atmospheric trace gases. Several satel-
lite instruments including GOME, ILAS and OMI use nadir viewing geometry in
atmospheric measurements. Other satellite viewing geometries include limb and
occultation geometries. Limb geometry means measuring the scattered light from
the atmosphere (Figure 2.9b), while occultation viewing geometry means mea-
suring the direct solar radiation through the atmosphere during sunrise or sunset
(Figure 2.9c). These two viewing geometries are useful for the measurements
of the vertical profiles of trace gases. The SCIAMACHY instrument combines
all the three viewing geometries (Beirle et al., 2010). By applying the limb-nadir
matching, the stratospheric contribution of total slant columns of NO_2 can be cor-
rected from the total slant columns retrieved from nadir measurements (Hilboll
et al., 2013).

Satellite measurements are important for atmospheric studies in providing the
spatial distribution of atmospheric trace gases (Burrows et al., 1999; Bovensmann
et al., 1999; Callies et al., 2000; Levelt et al., 2006). The spatial coverage and res-
olution of satellite measurements have been improved a lot in the recent decades.
Nadir-view satellites can provide a global coverage in six days for SCIAMACHY,
three days for GOME and one day for OMI. The spatial resolutions of these satel-
lite instruments have also been improved by more than 10 times, which are form
$\sim 3200 \, \text{km}^2$ ($40 \, \text{km} \times 80 \, \text{km}$) for GOME, $\sim 1800 \, \text{km}^2$ ($30 \, \text{km} \times 60 \, \text{km}$) for SCIA-

MACHY to $\sim 320\,\mathrm{km}^2$ ($13\,\mathrm{km} \times 24\,\mathrm{km}$) for OMI. These satellite measurements have been widely used in the studies of the emissions and dynamics of trace gases from both natural and anthropogenic sources (Wenig et al., 2003; Richter et al., 2005; Zhang et al., 2007; van der A et al., 2008; Pujadas et al., 2011).

2.5 Passive DOAS Characteristics

2.5.1 Fraunhofer lines

Most passive DOAS instruments use sunlight as the light source. The shape of solar spectrum at the top of the earth's atmosphere is determined by the physical and chemical composition of the sun's surface, especially its atmosphere. As a first approximation, the solar radiation can be described as the emission of a black body with a surface temperature of $\sim 5800\,\mathrm{K}$. However, this continuous spectrum is overlaid by many strong absorption lines which are caused by the selective absorption and re-emission of radiation in the sun's photosphere. These absorption structures are called the Fraunhofer lines (first discovered by Joseph von Fraunhofer, 1787–1826). Fraunhofer lines can cause strong variations in the intensity of the solar spectrum. In the UV-VIS wavelength range (300–600 nm), the optical densities of the Fraunhofer lines are typically two to three orders of magnitude higher than the optical densities of the trace gas absorptions in the earth's atmosphere.

In passive DOAS studies, in order to minimize the influence from the Fraunhofer lines, a Fraunhofer reference spectrum (which also serves as I_0) should be always included in the DOAS fitting process. For MAX-DOAS, as the off-zenith and reference spectra are measured within a short time span, the influence from Fraunhofer lines does not play an important role. A sample of Fraunhofer spectrum is shown in Figure 2.10.

2.5.2 The Ring effect

The Ring effect (Grainger and Ring, 1962) describes a reduction of the observed optical densities of the Fraunhofer lines. The Ring effect is primarily caused by the inelastic rotational Raman scattering of photons with air molecules (Fish and Jones, 1995; Burrows et al., 1996) (see Section 2.1.3). Such scattering processes cause changes in not only the photons' directions but also their wavelengths,
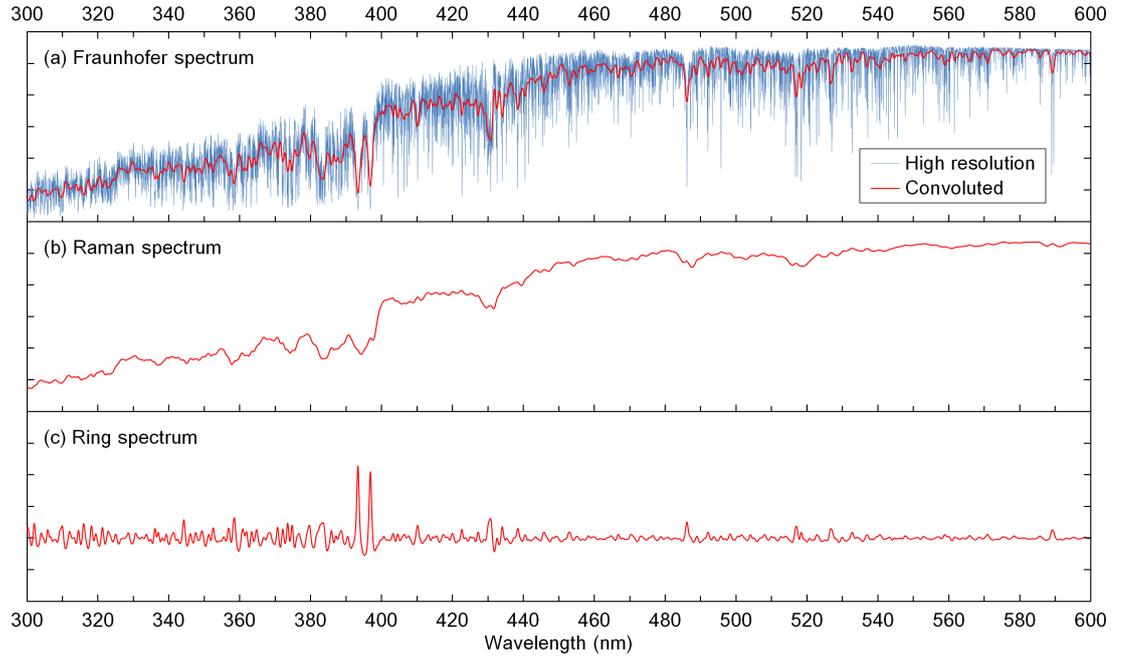
Figure 2.10: Samples of Fraunhofer, Raman and Ring spectra. In Panel (a), the blue curve shows the high resolution Fraunhofer spectrum, and the red curve shows the Fraunhofer spectrum convolved with a Gaussian slit function with 0.75 nm FWHM (full width at half maximum). In Panel (b), the Raman spectrum is convolved with the same function. In Panel (c), the Ring spectrum is calculated from the convolved Raman and Fraunhofer spectra.

therefore the spectrum of scattered sunlight is smoothed, and the Ring effect is also called 'filling-in' of Fraunhofer lines. In addition, the intensity of the Ring effect increases with longer atmospheric light paths and accordingly with larger solar zenith angles (SZAs).

The Ring effect can significantly affect passive DOAS measurements, therefore it must be thoroughly corrected from the spectra of scattered sunlight. Usually, the Ring effect is treated as a pseudo absorber, and a so-called Ring spectrum is included in the DOAS fitting process.

The scattered sunlight measured by passive DOAS instruments comes from either elastic scattering processes (Rayleigh and Mie scattering) or Raman scattering. Their intensities can be written as:

$$
\begin{aligned}
I_{\mathrm{meas}} &= I_{\mathrm{Rayleigh}} + I_{\mathrm{Mie}} + I_{\mathrm{Raman}} \\
&= I_{\mathrm{elastic}} + I_{\mathrm{Raman}}.
\end{aligned}
\tag{2.21}
$$

As presented in Section 2.2, the logarithm of the measured spectrum need to be taken for the DOAS evaluation, therefore,

$$
\begin{aligned}
\ln(I_{\mathrm{meas}}) &= \ln(I_{\mathrm{elastic}} + I_{\mathrm{Raman}}) \\
&= \ln(I_{\mathrm{elastic}}) + \ln(1 + \frac{I_{\mathrm{Raman}}}{I_{\mathrm{elastic}}}).
\end{aligned}
\tag{2.22}
$$

Since $I_{\mathrm{Raman}} << I_{\mathrm{elastic}}$,

$$
\ln(I_{\mathrm{meas}}) \approx \ln(I_{\mathrm{elastic}}) + \frac{I_{\mathrm{Raman}}}{I_{\mathrm{elastic}}}.
\tag{2.23}
$$

Then the Ring spectrum can be calculated as:

$$
I_{\mathrm{Ring}} = \frac{I_{\mathrm{Raman}}}{I_{\mathrm{elastic}}}.
\tag{2.24}
$$

Ring reference spectrum can be derived by either measurement or modeling. The the rotational Raman scattered intensity can be obtained by measuring scattered sunlight spectra at different viewing directions, and therefore a Ring spectrum can be derived (Solomon et al., 1987b). However, this method can be interfered by Mie scattering, and it is also dependent on the polarization direction. On the other hand, by including Raman scattering into radiative transfer models, the cross section of rotational Raman scattering can be calculated from the known energies of the rotational states of O_2 and N_2 (Fish and Jones, 1995; Chance and Spurr, 1997). In this way, the shortcomings of measured Ring spectrum can be overcome. Moreover, modeled Ring spectrum was found to be consistent with highly resolved atmospheric observations (Aben et al., 2001). In this study, modeled Ring spectra were used in the DOAS evaluation. The calculation of Ring spectra was performed by the the spectra evaluation software QDOAS developed at BIRA-IASB (Belgian Institute for Space Aeronomy, http://uv-vis.aeronomie.be/software/QDOAS/). A sample of Raman and Ring spectra is shown in Figure 2.10.

2.5.3 The I_0 effect

In DOAS measurements, the resolution of measured spectra is limited by the spectral resolution of the spectrometer, which typically varies from a few tenths to several nanometers. Accordingly, the absorption cross sections of trace gases also need to be convolved with the same slit function. Therefore, the natural line

widths of the Fraunhofer spectrum and the atmospheric absorptions cannot be resolved. Since both $I(\lambda)$ and $I_0(\lambda)$ in the DOAS equation (Eq. 2.11) have been filtered by the slit function before taking the ratio, the Fraunhofer structures can not be totally removed, introducing the so-called I_0 effect (Johnston, 1996).

The I_0 effect can be corrected in the following way: First, a highly resolved solar spectrum $I_0(\lambda)$ is convolved with the slit function of the DOAS instrument (the convolved spectrum is denoted as $I_0^*(\lambda)$). In the next step, a modeled absorption spectrum is calculated from the highly resolved solar spectrum and a highly resolved absorption cross section, and the modeled spectrum is then convolved with the slit function as well (the convolved spectrum is denoted as $I^*(\lambda)$). In the calculation, an atmospheric SCD of the trace gas (S) need to be assumed. Finally, the I_0 corrected cross section is derived as:

$$\sigma_{\text{corrected}}(\lambda, S) = -\ln\left[\frac{I^*(\lambda)}{I_0^*(\lambda)}\right] \cdot \frac{1}{S}. \qquad (2.25)$$

In principle, the I_0 corrected absorption cross section perfectly matches the absorptions in the measured spectrum only if the SCD used for the calculation matches the actual SCD in the atmosphere. However, in most studies, fixed SCD values which are typical of the maximum were used for I_0 corrections, and the errors were found to be insignificant (Aliwell et al., 2002). In addition, the I_0 effect is only significant for strong absorbers, while it can be neglected for weak absorbers. In this study, we followed the common settings of other studies that only NO_2 and O_3 were corrected for I_0 effect, and fixed SCDs were used.

Chapter 3

Instrumentation

In this section, we present the information about the measurement site and the MAX-DOAS instrument, as well as auxiliary measurements.

3.1 Measurement site — the UFS

The Environmental Research Station Schneefernerhaus (UFS, German: Umwelt-forschungsstation Schneefernerhaus) (47.417°N, 10.980°E) is located close to the summit of the Zugspitze (2962 m above sea level), at an altitude of 2,650 m above sea level (a.s.l.). As it is surrounded by the mountainous area of Alps and there are no significant emissions at this altitude, the ambient air around the UFS is mostly clean and unpolluted. Therefore the station is usually referred as a background site. The UFS is located in the free troposphere and allows measurements above the PBL, which is very special for atmospheric environment study. The location of the UFS is shown in Figure 3.1 and Figure 3.2.
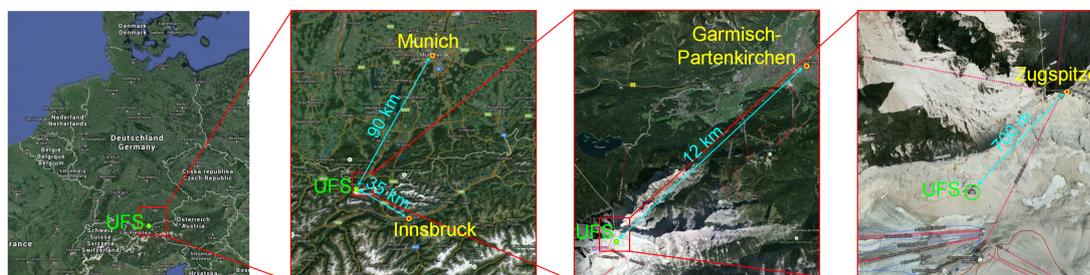
Figure 3.1: Location of the UFS. Images captured from Google Maps.

Figure 3.2: The Environmental Research Station Schneefernerhaus, seen from the cable car station on Zugspitzplatt. The red circle indicates the location of the MAX-DOAS telescope.

Zugspitze is the highest peak of the Wetterstein Mountains and also the highest mountain in Germany. It lies in the northern Alps and to the southwest of Garmisch-Partenkirchen. The Austria-Germany border runs over its western summit. South of the mountain is the Zugspitzplatt, a high karst plateau with numerous caves. The UFS is located on the south slope of Zugspitze, around 250 m below the summit. The closest populated area is the town of Garmisch-Partenkirchen which is located ~12 km away in the northeast direction. The big cities of Innsbruck and Munich are located about 35 and 90 km away, respectively.

The Schneefernerhaus (literally means 'snow far house') was originally a tourist hotel and the top station of the rack railway from Garmisch-Partenkirchen (Bayerische Zugspitzbahn). It was opened in 1931 together with a short cable car that took the guests all the way to the summit. When the Schneeferner glacier retreated in the 1960s, the slope below Schneefernerhaus became too steep for most skiers. A fatal avalanche in 1965 marked the beginning of the decline of the hotel. After a new rack railway station was opened on the Zugspitzplatt in 1988 and the restaurant SonnAlpin enlarged in 1989, the hotel was finally closed

in 1992 due to the lack of guests. In 1992, the Rio Earth Summit addressed for the first time the issue of climate change and 172 nations agreed on the Climate Change Convention. As a result, the former hotel Schneefernerhaus was modified to become a modern research station in 1993. The research station was officially opened in 1999 after about 8 million Euros had been spent.

The station is currently operated by the Betriebsgesellschaft UFS GmbH (Operating Company of UFS Co., Ltd.) and supported by the Umweltministerium Bayern (Bavarian Environment Ministry). Scientists from many different institutions carry out continuous measurements or work on research projects at the station. The UFS is not only a center for environment and climate research and observatory, but also a communication and conference center for teaching, education and sustainability strategies.

3.2 MAX-DOAS instrumental setup
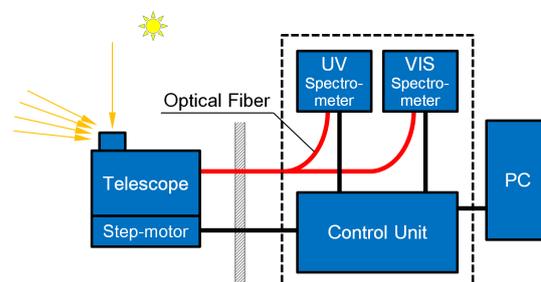
Figure 3.3: Schematic view of the MAX-DOAS instrument operated at the UFS.

This study is mainly based on the long-term MAX-DOAS measurements at the UFS. Figure 3.3 shows the components of the MAX-DOAS instrument operated at the UFS. The instrument includes a scanning telescope and two spectrometers. The control unit and the spectrometers are installed in a 19-inch rack. Scattered sunlight collected by the telescope is redirected by a prism reflector and then transmitted to the spectrometers through an optical fiber bundle. A desktop PC controls the entire instrument and can be remotely accessed. The instrument started operation in 2011.

3.2.1   Telescope

The telescope was set up on the roof of the UFS, about 20 m above ground level, see Figure 3.2. In a previous study (Jurgschat, 2011), the field of view (FOV) of the telescope was measured to be 0.98°. As shown in Figure 3.4, the lens of the telescope is driven by two stepper motors and can allow a 360° azimuth and elevation movement. One motor moves the upper part of the telescope around the optical axis, while the other one is mounted on the upper part and can rotate the incoming prism with its enclosure. The light collected by the telescope is redirected by the two prisms and then focused by a concave mirror with a diameter of 25.4 mm and a focal length of 76.2 mm. The entrance of the optical fiber bundle is placed at the focal point. There is a moveable sand-blasted glass shutter which can be placed in front of the fiber entrance, so as to block the moon and starlight when measuring the dark current and offset spectra at night (see Section 3.2.5). The shutter can also be used for direct-sun measurements when required. In addition, the telescope can also be directed to the built-in mercury and halogen lamps, so as to measure the Hg-Ne spectra which are useful in the pixel-to-wavelength calibration.

(a) Schematic view   (b) Photo
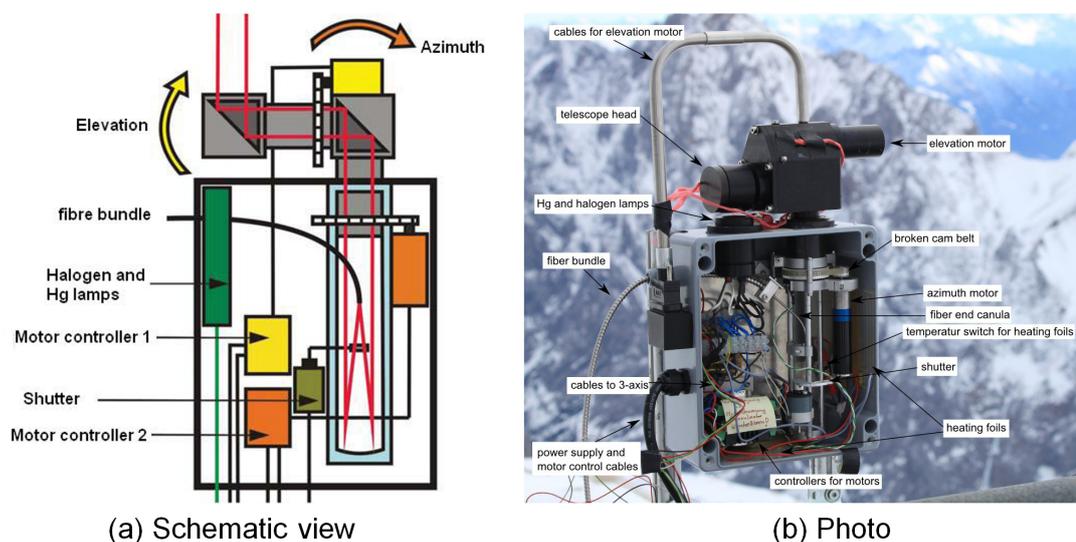
Figure 3.4: Components of the MAX-DOAS telescope. (a) Schematic view, from Niebling (2010); (b) Photo, from Jurgschat (2011).

In the study, the telescope always looked to the due south (180°) and scanned only in vertical direction. This viewing azimuth was least influenced by the surrounding mountains. As shown in Figure 3.5, with an FOV of 0.98° considered,

the telescope could see the unblocked sky when the elevation angle varies between 1° and 90°. The horizon of the telescope was mostly above the mountainous area of the Alps, see Figure 3.6.
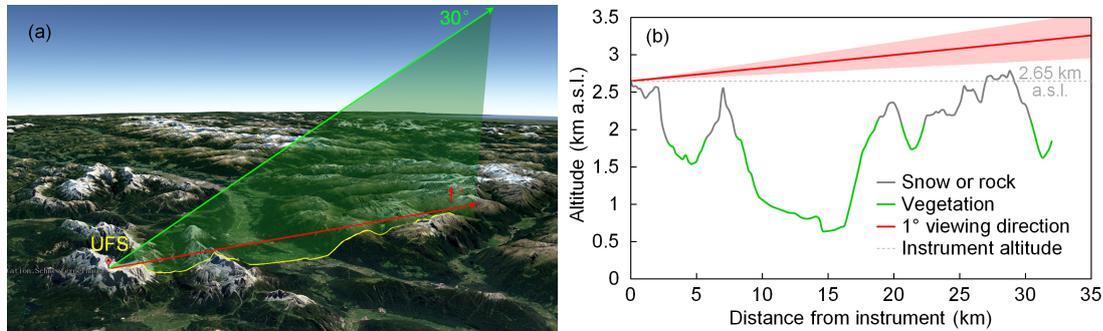
Figure 3.5: Topography around the UFS. (a) Image of the land around the UFS from Google Earth in 3D view, together with the viewing directions of 1° and 30°. The yellow curve indicates the projection of the viewing direction on the ground. (b) Altitude and type of the ground surface under the viewing direction, altitude data are obtained from Google Earth. The shadow beside the line of 1° viewing direction indicates the FOV of the telescope which was measured to be 0.98°.

Figure 3.6: View from the MAX-DOAS observation azimuth. The red arrow indicates the viewing direction of the MAX-DOAS telescope.

3.2.2 Optical fiber bundle

The light collected by the telescope is transmitted to the two spectrometers through an optical fiber bundle. The optical fibers are made of hydrogen-doped quartz, so as to minimize the solarization degradation. As shown in Figure 3.7,

the bundle consists of 19 separate $200\,\mu$m fibers and has one entrance and four exits. At the entrance, the 19 fibers are arranged as a round cluster. At three of the four exits, each exit has six fibers linearly arranged; at the other exit, there is only one fiber. The exits can be coupled with the entrance slits of spectrometers.

In our observations, the two spectrometers worked simultaneously, one measured the spectra at the UV band and the other measured at the VIS band. Since the light intensity and the photodetectors' quantum efficiency at the VIS band are both much higher than those at the UV band, the UV spectrometer was coupled with an exit with six fibers, while the VIS spectrometer was coupled with the exit with only one fiber. In this way, the difference between the intensity counts of the two spectrometers is minimized.

Figure 3.7: Drawing of the optical fiber bundle, taken from manufacture's manual.

3.2.3 Spectrometers

In the study, two Czerny-Turner (Czerny and Turner, 1930) type spectrometers manufactured by OMT Instruments (OMT ctf-60) were used to measure the spectra. As illustrated in Figure 3.8, the optical system of each spectrometer consists of an optical fiber coupler, an entrance slit, a diffraction grating, two concave cylindrical mirrors and a linear CCD (charge coupled device) photodetector. The incident light is split to linear spectrum by the diffraction grating, and the linear CCD photodetector is placed at the focal plane of the optical system. Each photodetector includes 2,040 pixels, so that the light intensities at 2,040 wavelength points are measured. During the read out, the light intensities are converted to digital signal and each spectrum is recorded as an array of 2,040 integers. 16-bit A/D converters are used in both spectrometers, therefore the readouts range

Table 3.1: Parameters of the two spectrometers used in the study.

Code name	UV	VIS
Grating	1800 / nm	1302 / nm
Wavelength range (nm)	~320–478	~427–649
Width of entrance slit (μm)	75	50
FWHM (nm)	~1.1	~0.6

from 0 to 65,535 ($2^{16} - 1$). The spectrometers were temperature-stabilized to 258 K by Peltier coolers during the measurement, so as to lower down the dark current of photodetectors, as well as to avoid the change of the actual wavelength calibration caused by the thermal expansion of the optical bench.
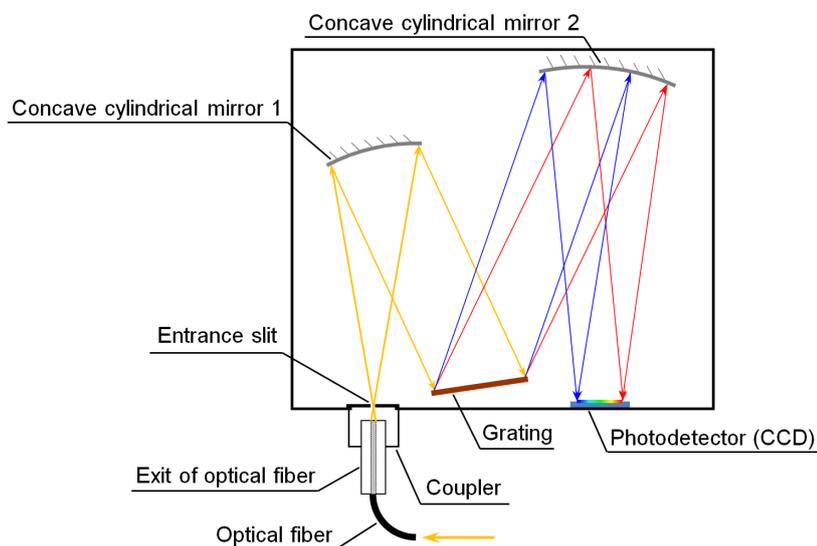
Figure 3.8: Schematic view of the optical system of the OMT ctf-60 spectrometer.

The UV and VIS spectrometers have the same design, but only differ in the diffraction grating and the width of entrance slit, hence they have different wavelength ranges and different instrument functions. Table 3.1 shows the parameters of the two spectrometers.

3.2.4   Software

All the components of the MAX-DOAS instrument — including the stepper-motors, photodetector, Peltier cooler, etc. — were controlled by the computer program MS-DOAS developed by the Institute of Environmental Physics of Heidelberg University.

During daytime (SZA < 85°), the instrument ran with a fixed cycle. Each cycle consists of measurements of scattered sunlight spectrum at elevation angles (α) of 1°, 2°, 5°, 10°, 20°, 30° and 90° (zenith). A single measurement at each elevation lasts for $\sim$1 min, and a full scanning cycle takes about 10 min. The recorded spectrum of each measurement is the sum of many readouts during the measurement period. In order to optimize the measurement signal-to-noise ratio (SNR), avoid saturation, and achieve a constant signal level, the data acquisition software automatically adjusts the exposure time of each readout to make the maximum count close to 70% of saturation level (65,535 counts). Depending on the intensity of received light, the exposure time of each readout varies from tens of milliseconds to a few seconds. The measurements of UV and VIS bands were taken by the two spectrometers simultaneously, but their exposure times were adjusted individually. The instrument took measurements continuously during daytime, but during the noon (175° < SAA (solar azimuth angle) < 185°) and twilight periods (85° < SZA < 92°), the instrument took only zenith measurements. At each night, the instrument measured five offset spectra and five dark current spectra (see Section 3.2.5).

3.2.5   Offset and dark current correction

The counts in the spectrum files directly obtained from the spectrometers contain offset and dark current. These two components bring bias to the spectrum, therefore they need to be corrected from the spectra, so that the counts can reflect the light intensity more precisely. Figure 3.9 and Figure 3.10 show examples of offset and dark current correction for a UV spectrum and a VIS spectrum, respectively.

Offset is a semi-constant value added to the photodetector in order to make sure that the measured light intensity is always positive, since the A/D converter can only work with positive analog signals, while it is possible to encounter negative signals due to detector noise. Offset spectra can be measured in dark (either cover the lens of the telescope or block the light path by the shutter) with very short exposure time and very large number of measurements so as to minimize the noise. In this study, offset spectra were measured with an exposure time of 13 ms per scan and each spectrum is the sum of 1,000 continuous scans. Figure 3.9 (b) and Figure 3.10 (b) show the offset spectra of UV and VIS bands measured on 07 December 2015. Since an offset is added to each scan, the measured spectra
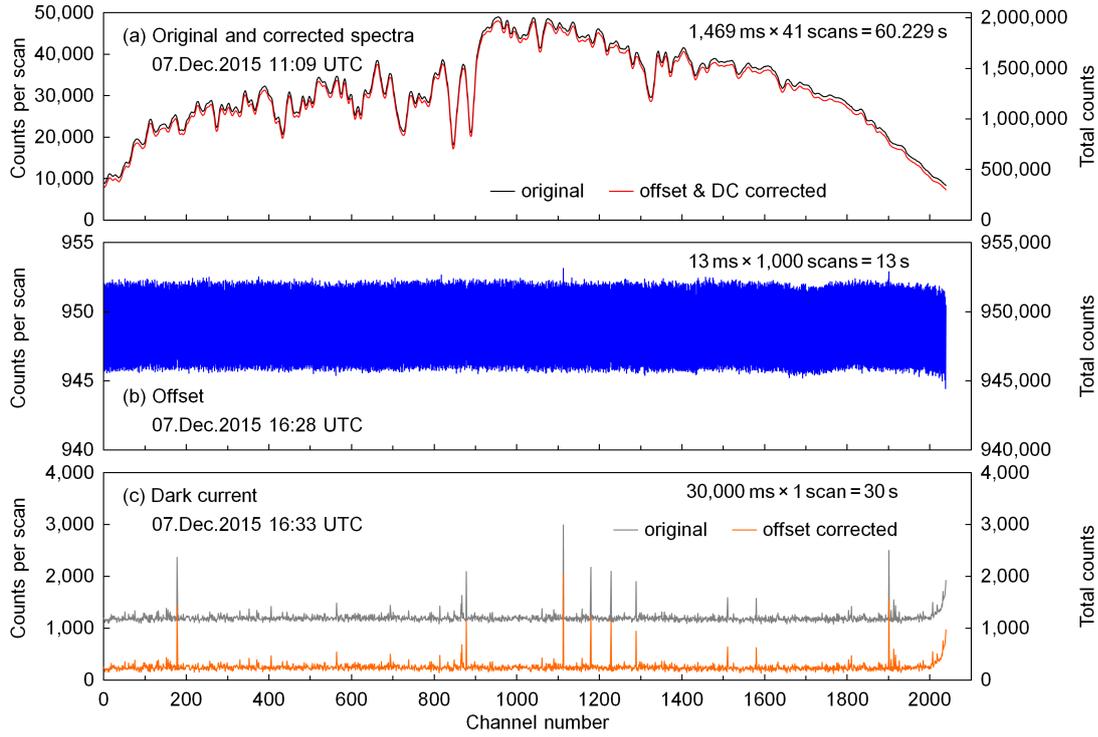
Figure 3.9: Example of offset and dark current correction for a UV spectrum measured on 07 Dec 2015. (a) Measured spectrum, before (black) and after (red) offset and dark current correction; (b) Offset spectrum; (c) Dark current spectrum, before (gray) and after (orange) offset correction. The y-axes on the left side refer to the counts per each scan, while the y-axes on the right side refer to the total counts of each spectrum.

are corrected with the following equation,

$$I_{\text{OFS\_corrected}}(n) \; = \; I(n) \; - \; \frac{N_{\text{meas}}}{N_{\text{ofs}}} \; \cdot \; O(n), \tag{3.1}$$

where n is the channel number, $I(n)$ and $I_{\text{OFS\_corrected}}(n)$ are the light intensity counts of the original and corrected spectra at the nth channel, respectively. N_{meas} is the number of scans of the measured spectrum, and N_{ofs} is the number of scans of the offset spectrum, which is 1,000 in the study. $O(n)$ is the total intensity count of the offset spectrum at the nth channel, which is the sum of N_{ofs} scans.

Dark current is the result of thermal excitation of the electrons in the valence band of the semiconducting CCD into the conduction band without the influence of photons. Dark current spectra can also be measured in dark but with very long exposure time, so as to accumulate the influence from dark current. In
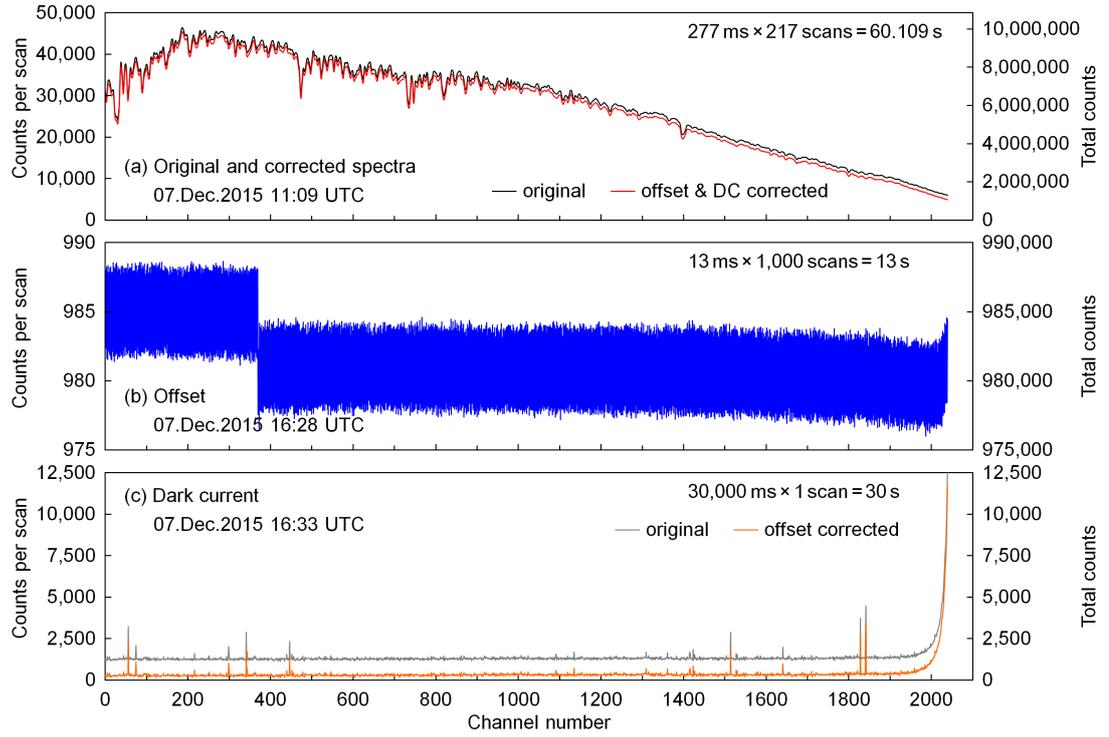
Figure 3.10: Same as Figure 3.9, but for a VIS spectrum measured on 07 Dec 2015.

this study, offset spectra were measured with an exposure time of 30 s and each offset spectrum records the result of only one scan. The dark current spectra also contain offset and need to be firstly corrected with Eq. (3.1), where N_{meas} is 1. (But it is unnecessary to correct dark current from the offset spectra, because the influence from dark current is already minimized.) Figure 3.9 (c) and Figure 3.10 (c) show the dark current spectra of UV and VIS bands measured on 07 December 2015, the gray and orange curves show the offset spectra before and after offset correction, respectively. Dark current is assumed to be proportional to exposure time, therefore the offset-corrected spectra are then corrected for dark current with the following equation,

$$I_{\mathrm{OFS\&DC\_corrected}}(n) = I_{\mathrm{OFS\_corrected}}(n) - \frac{t_{\mathrm{meas}}}{t_{\mathrm{DC}}} \cdot D_{\mathrm{OFS\_corrected}}(n), \qquad (3.2)$$

where t_{meas} and t_{DC} are the total exposure times of the measured spectrum and the dark current spectrum, respectively. $D_{\mathrm{OFS\_corrected}}(n)$ is the offset-corrected intensity count of the dark current spectrum at the nth channel. $I_{\mathrm{OFS\&DC\_corrected}}(n)$

represents the light intensity count of the measured spectrum at the nth channel after both offset and dark current corrections.

Figure 3.9 (a) and Figure 3.10 (a) show examples of UV and VIS spectra before and after the offset and dark current correction. The black curves represent the original spectra, while the red curves refer to the corrected spectra. The corresponding offset and dark current spectra are shown in Figure 3.9 (b, c) and Figure 3.10 (b, c).

Offset and dark current may slightly change from time to time, therefore we measure offset and dark current spectra every night, and the spectra measured during daytime are corrected with the offset and dark current measured on the same day.

3.2.6   Wavelength calibration

Each data point of the spectrum represents the light intensity at a certain wavelength. However, the exact wavelength corresponding to each point is unknown from the raw data. Usually, wavelength information can be obtained from the spectrum of the light with well-known structures like the sunlight or the light from mercury-vapor lamp. In this study, our calibrations were preformed by fitting measured solar spectrum to literature solar reference. Comparing to mercury-vapor lamp, the solar spectrum is continuous and has much more characteristic points, so that the calibration can be more accurate.

Figure 3.11 shows an example of wavelength calibration for the UV spectrometer. The blue curve in Panel (a) shows the high-resolution (0.01 nm) solar spectrum obtained from literature (Chance and Kurucz, 2010). It was first convolved with the slit function of the spectrometer, which is a Gaussian function with FWHM $= 1.1$ nm. The convolved spectrum is shown as the red curve in Panel (a). Panel (b) shows the spectrum of scattered sunlight measured by the UV spectrometer on 07 December 2015 at 11:09 UTC, which has a similar structure as the convolved solar spectrum in Panel (a). The characteristic peaks of the measured spectrum can be mapped with the corresponding points of the convolved solar spectrum. In this way, we selected 41 characteristic points and obtained their corresponding wavelengths from the literature spectrum, marked as gray lines in Figure 3.11. As shown in Figure 3.12, a 3rd order polynomial regression was applied between the channel numbers of the characteristic points and their corresponding wavelengths. The regression function and the correlation
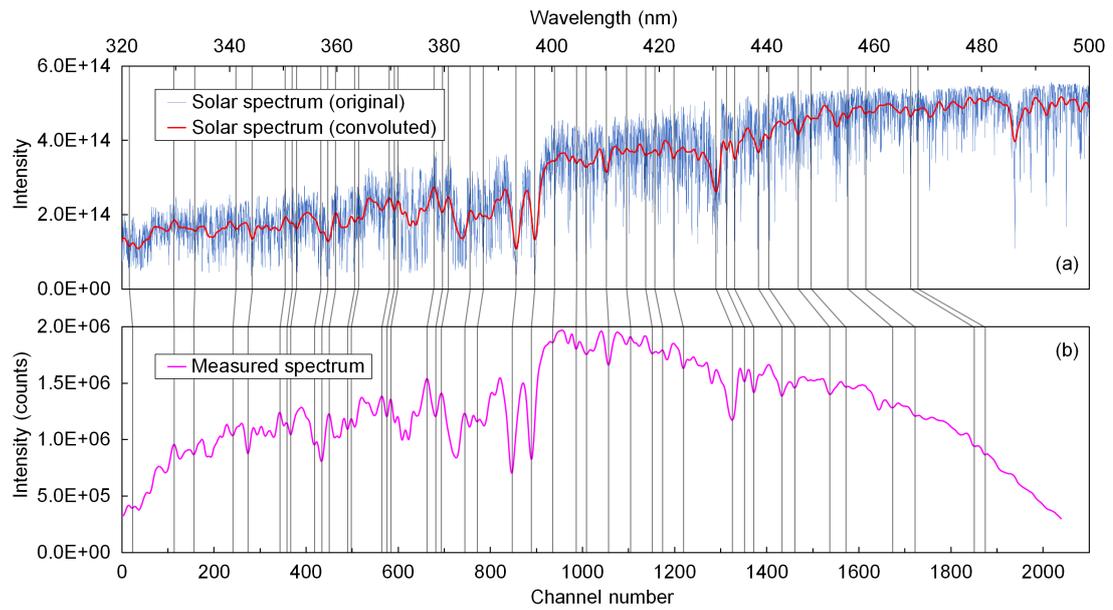
Figure 3.11: An example of wavelength calibration. (a) Standard solar spectrum from literature (Chance and Kurucz, 2010), the blue curve shows the original high-resolution (0.01 nm) spectrum, the red curve shows the spectrum convolved with the slit function of the UV spectrometer (a Gaussian function with FWHM = 1.1 nm); (b) Scattered sunlight spectrum measured by the UV spectrometer on 07 Dec 2015 at 11:09 UTC. The gray lines mark the correspondence between the characteristic points of the measured spectrum and the convolved literature spectrum.
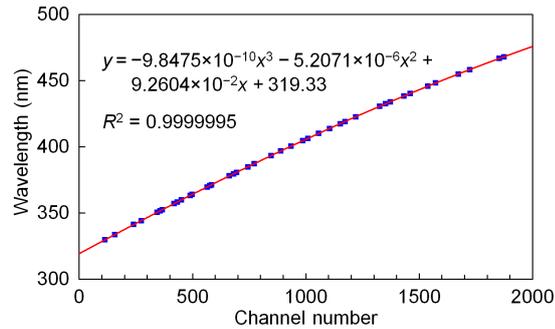
Figure 3.12: 3rd order polynomial regression of the channel numbers of the selected characteristic points shown in Figure 3.11 versus their corresponding wavelengths.

coefficient are shown in the figure. The regression shows very good correlation, therefore the accurate wavelengths corresponding to all the photodetector channels can be derived from the regression function. The VIS spectrometer was

calibrated in the same way.

3.3   Auxiliary measurements

3.3.1   Sun photometer

Next to the MAX-DOAS instrument, a sun photometer was installed at the UFS, which provided measurements of radiances at 12 wavelengths between 340 and 1640 nm with a temporal resolution of 1 s. The instrument was developed at the Meteorological Institute of Ludwig Maximilian University of Munich (LMU) based on a system operated in the framework of the SAMUM campaigns (Toledano et al., 2009, 2011) but with improved electronics and data acquisition developed by Physikalische Messsysteme Ltd.
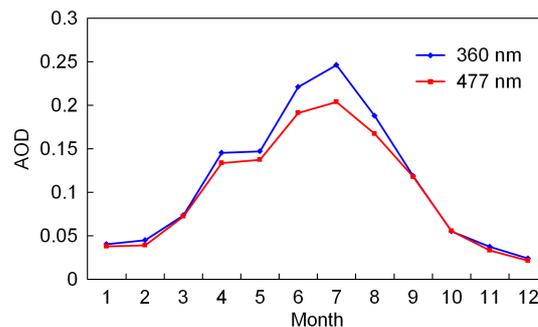
Figure 3.13: Annual variation pattern of AODs measured by the sun photometer at the UFS, averaged from the data from Jan 2012 to Feb 2016. Only the data from 10:00 to 14:00 UTC and under cloud-free conditions were used. The data of 360 nm were interpolated from the measurements at 340 and 380 nm, while the data of 477 nm were interpolated from the measurements at 440 and 500 nm.

In this study, the AODs derived from sun photometer measurements applying the well-established Rayleigh calibration method were used for the intercomparison with the MAX-DOAS retrieval. For this purpose, AOD measurements at 340 and 380 nm were interpolated to 360 nm while AODs at 477 nm were interpolated from the measurements at 440 and 500 nm. The interpolation followed the Ångström exponent method. Measurements were given as hourly averages. Due to the reduced accuracy under large SZAs, only the measurements between 10:00 and 14:00 UTC each day were used. In order to ensure the data quality, only cloud-free conditions and periods of stable aerosol abundance (variability

of radiances below 5% within 1 h) were considered. These requirements reduce the number of available sun photometer measurements considerably. Note that the AOD is often below 0.02 at the relevant wavelengths with an uncertainty on the order of ± 0.015 due to calibration errors, Rayleigh correction, and radiometric accuracy. Figure 3.13 shows the annual variation pattern of the interpolated AODs at 360 and 477 nm. The results show that the AOD at the UFS is high in summer and low in winter. For both wavelengths, the average AOD in July is higher than that in December by a factor of ~ 10. In addition, the AOD at 360 nm is slightly higher than the one at 477 nm.

As the uncertainty of the AOD measured by the sun photometer is relatively large, the uncertainty of the Ångström exponent would be further amplified. Consequently, they were not used in this study.

3.3.2   Aerosol optical property data from AERONET

The aerosol optical property data such as the single scattering albedos and phase functions are also required by the radiative transfer simulation for the MAX-DOAS aerosol retrieval. However, they were not available from the sun photometer at the UFS. In this study, these data were estimated from the AERONET (Aerosol Robotic Network, Holben et al. (1998); Dubovik et al. (2000)) measurements at Hohenpeißenberg (47.802°N, 11.090°E), which is located at an altitude of 980 m and approximately 43 km north of the UFS, see Figure 3.14.
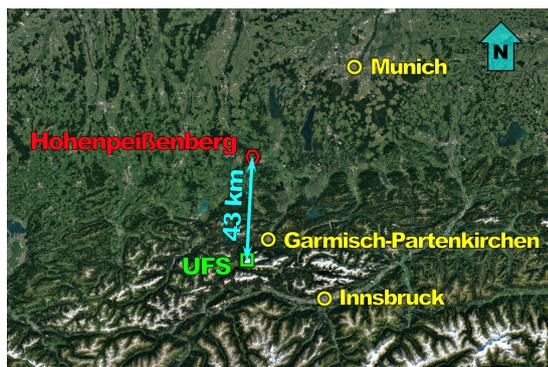
Figure 3.14: Location of the Hohenpeißenberg AERONET station, satellite image from Google Earth.

AERONET is a network of ground-based sun photometers which provides the spectral AODs from direct sun observations. The AERONET project has been

initiated by NASA (National Aeronautics and Space Administration, USA) and
expanded by the federation with many other institutions. For more than two
decades, AERONET has provided long-term, continuous and readily accessible
database of aerosol optical, microphysical and radiative properties, which pro-
vides valuable information for aerosol research and characterization, validation of
satellite retrievals, as well as the synergism with other databases.

The measurement system of the AERONET consists of the CIMEL Electron-
ique CE318 multiband sun photometers. The latest CE318-T model has been
employed since 2014, which also performs lunar measurements during nighttime.
Each sun photometer consists of a sensor head fitted with a 25 cm collimator,
which is attached to a 40 cm robot base that systematically points the sensor
head at the sun, the sky and the moon according to a preprogrammed routine.
The other components including the control unit, batteries, and Sutron satellite
transmission equipment are deployed in a weatherproof plastic case.

The AERONET data are available at 440, 675, 870 and 1,020 nm, however,
the data at 360 and 477 nm are needed in our study. Therefore, the data at
360 nm were extrapolated, while the data at 477 nm were interpolated.

3.3.3   Ceilometer

The UFS was also equipped with a Lufft (previously Jenoptik) ceilometer (model:
CHM15kx, see Wiegner and Geiß (2012)) operated by the German Weather Ser-
vice (DWD). Ceilometers are single-wavelength backscatter lidars, and the re-
ceived signals follow the well-known lidar equation (Wiegner et al., 2014). The
CHM15kx is eye-safe and fully automated which allows unattended 24/7 oper-
ation. It can be used to monitor aerosol layers (e.g., volcanic ash, see Schäfer
et al. (2011)), validating meteorological and chemistry transport models (see,
e.g., Emeis et al. (2011)), and is foreseen for model assimilation (e.g., Wang
et al., 2014b; Warren et al., 2018; Chan et al., 2018).

The CHM15kx ceilometer is equipped with a diode-pumped Nd:YAG laser
emitting laser pulses at 1,064 nm. The received backscatter signals are stored in
1,024 range bins with a resolution of 15 m. The temporal resolution was set to
15 s. The signals were corrected for incomplete overlap by a correction function
provided by the manufacturer.

A strict retrieval of the particle extinction coefficient from ceilometer measure-
ments is not possible due to the unknown lidar ratio; furthermore, exploitation
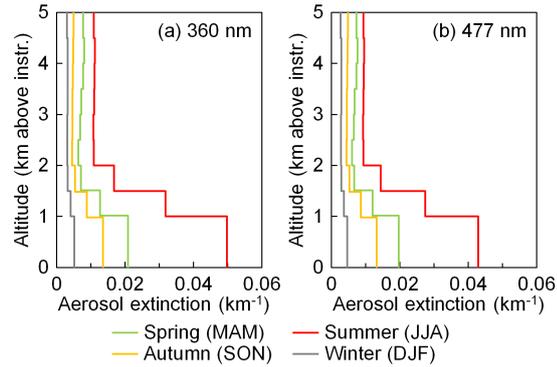
Figure 3.15: Seasonal average aerosol extinction profiles extracted from ceilometer measurements.

of the signal in the range of incomplete overlap is subject to errors. Thus, in order to convert the ceilometer measurements to aerosol extinction profiles, we followed an approach mentioned in Wagner et al. (2019). The range corrected attenuated backscatter data from July 2016 to December 2017 were seasonally averaged. Data of the altitude between 500 m and 5 km above instrument were averaged with a vertical grid resolution of 500 m. Data below 500 m were assumed to be constant, following the values at 500 m. The extinction coefficients were first calculated by scaling the attenuated backscatter profiles (β^*) to the seasonal average AODs at 360 and 477 nm obtained from the sun photometer. The extinction profiles were then used to correct for the attenuation of the backscatter profiles following the lidar equation (Klett, 1981; Fernald, 1984). The corrected backscatter profiles (β) were then scaled to the AODs at 360 and 477 nm measured by the sun photometer to obtain the extinction profiles, see Figure 3.15. Note that the ceilometer measures at 1,064 nm and the optical properties of aerosols depend on the wavelength. Therefore, the uncertainties of these profiles are very large and they should be considered as qualitative only.

The results shown in Figure 3.15 indicate that the aerosol load at the UFS is highest in summer (June, July and August) and lowest in winter (December, January and February). The seasonal results also indicate large variations of the aerosol load from the surface up to 2 km. The variability of aerosol extinction above 2 km is smaller, however, their contribution to the total column is still substantial ($\sim$30 – 50%).

Chapter 4

Cloud screening

The aerosol profile retrieval requires the forward simulation of the radiative transfer in the atmosphere. As the radiative transfer is rather complicated for cloudy sky condition, the forward simulation usually assumes a cloud-free atmosphere. The aerosol retrieval might result in large uncertainty under cloudy or foggy conditions. Therefore, it is important to filter out the measurements taken under cloudy or foggy conditions. In this study, we developed a new cloud screening method based on the color index (CI) (Wagner et al., 2014, 2016) in order to filter out cloudy measurements.

4.1 Definition of color index

In this study, CI is defined as the ratio between the radiative intensities at 330 and 390 nm. Larger CI indicates the UV/VIS intensity ratio is higher, hence, the sky is bluer. Lower CI on the other hand indicates the UV intensity is much smaller than the VIS intensity, hence the sky is white (cloudy).

Measured CIs (denoted as CI_{meas}) were calculated from the zenith UV spectra (offset and dark current corrected) by taking the ratio of the counts at 330 and 390 nm. Figure 4.1 shows the time series of CI_{meas} calculated from all the zenith spectra with $30° < \mathrm{SZA} < 70°$ during the entire study. The results show that the variation range of CI_{meas} is stable within the two periods. However, the optical throughput of the instrument in the UV spectral range has been enhanced after a regular maintenance of the optical system in 2013. Hence, the CI increased systematically in the second period. Therefore, calibration of CI_{meas} is necessary in order to make the CI_{meas} measured during the two periods comparable to each
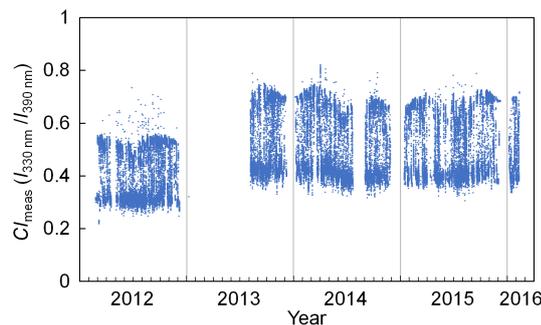
Figure 4.1: Time series of CI_{meas} (measured color indices) calculated from the zenith UV spectra measured during the entire study with $30° < \mathrm{SZA} < 70°$.

other.

4.2   Calibration of color index

The calibration followed the method suggested in Wagner et al. (2016), with which CI_{meas} under overcast skies were fitted to the simulated minimum CIs ($CI_{\mathrm{sim,\ min}}$). In this way, measured CIs would also be comparable with simulated values. Simulated CIs were calculated using the radiative transfer model LIDORT (see Section 5.1.2). Intensities at 330 and 390 nm were simulated under given aerosol profiles and measurement geometries, and simulated CIs (CI_{sim}) were then derived by taking the ratios of the simulated intensities at 330 and 390 nm. The other simulation parameters followed the settings used in the aerosol retrieval: the single scattering albedo was set to 0.93, the phase function was defined as the 'median' phase function (see Section 5.6.3), the surface albedo was set to 0.1, and the ground was defined as a flat surface at the altitude of 2,650 m. For each integer SZA between 24° and 85°, we calculated the CI_{sim} with profiles corresponding to cloud optical depths (CODs) of 2, 3, 4, 8, 12 and 50, and the minimum CI_{sim} is used as $CI_{\mathrm{sim,\ min}}$. The cloud layer was defined as a homogeneous aerosol layer between 1 and 2 km above instrument. $CI_{\mathrm{sim,\ min}}$ under different SZAs are shown as the red curve in Figure 4.2. When SZA varies between 30° and 60°, $CI_{\mathrm{sim,\ min}}$ varies within a very narrow range of 0.83986 ± 0.00088. This result mostly agrees with the result reported in Wagner et al. (2016), that CI_{sim} varies between 0.816 and 0.847 when SZA varies between 30° and 60°.

For each period, all the CI_{meas} with with $30° < \mathrm{SZA} < 60°$ were divided by the $CI_{\mathrm{sim,\ min}}$ under the corresponding SZA, and the results are denoted as
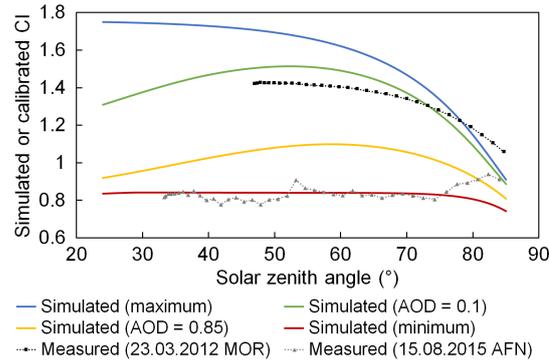
Figure 4.2: Comparison of CI_{sim} (simulated color indices) and CI_{cal} (calibrated measured color indices). The blue curve shows the maximum CI_{sim} under different SZAs, which were simulated with an aerosol-free profile. The green curve shows the CI_{sim} for AOD = 0.1, simulated with a homogeneous aerosol layer between 0 and 1 km above ground. The orange curve shows the CI_{sim} for AOD = 0.85, simulated with a homogeneous aerosol layer between 0 and 1 km above ground. The red curve indicates the $CI_{\mathrm{sim,\,min}}$ (minimum simulated color indices) under different SZAs, derived from the minimum value among the CI_{sim} for CODs of 2, 3, 4, 8, 12 and 50. The black square markers show the CI_{cal} on the morning of 23 Mar 2012 which was cloud-free, and the AOD measured by the sun photometer around the noon was $\sim$0.1. The gray triangle markers show the CI_{cal} on the afternoon of 15 Aug 2015, during which the site was covered by heavy fog.
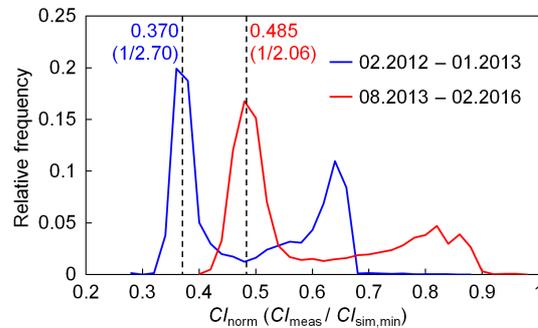
Figure 4.3: Frequency distribution (for bins of 0.02) of CI_{norm} (normalized color indices) with $30° < \mathrm{SZA} < 60°$. CI_{norm} is the ratio between CI_{meas} and $CI_{\mathrm{sim,\,min}}$ under the same SZA.

CI_{norm}. The frequency distribution of the CI_{norm} during the two periods are shown in Figure 4.3. During each period, there is a clear peak at the lower CI_{norm} value, corresponding to measurements under overcast skies. For each period, the inverse of the peak value was used as the CI correction factor β, and CI_{meas} was converted to CI_{cal} by multiplying the factor:

$$CI_{\mathrm{cal}} = CI_{\mathrm{meas}} \cdot \beta. \tag{4.1}$$

By fitting each peak to a Gussian function, β was determined to be 2.70 and 2.06 for the periods of 02.2012–01.2013 and 08.2013–02.2016, respectively. For each period, the CI_{meas} of all the zenith measurements (also including the measurements with SZA $< 30°$ or $> 60°$) were calibrated with the same factor.

4.3 Definition of cloud screening threshold

Wagner et al. (2016) suggested to use the CI_{sim} under AOD $= 0.85$ as the threshold for distinguishing a cloud covered sky. However, comparing to the CI_{cal} measured at the UFS, it is found that CI_{sim} is significantly underestimated under large SZAs. As shown in Figure 4.2, when the SZA is larger than 80°, CI_{cal} measured under clear sky (the black curve) can exceed the maximum CI_{sim} (the blue curve, simulated under aerosol free condition), and CI_{cal} measured in foggy weather (the gray curve) can also exceed CI_{sim} under AOD $= 0.85$ (the yellow curve). Therefore, we have to either use another threshold or further calibrate the measured CIs.
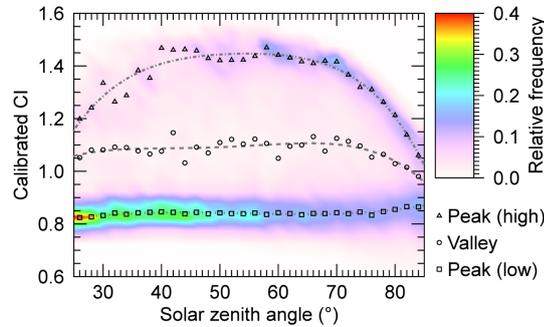
Figure 4.4: Distribution pattern of CI_{cal} (calibrated color indices) during the entire study. Data were grouped by SZA with an interval of 2°. For each group, frequency was counted for bins of 0.05. Peak and valley values (shown as markers) were determined by Gaussian fit. The curves are the results of 4th order polynomial regressions of each data series.

In order to determine the threshold for cloud screening, we first analyzed the distribution pattern of CI_{cal} from the long-term data, see Figure 4.4. The CI_{cal} from the long-term measurement were grouped by SZA with a step size of 2°. The relative frequency distributions are color coded in Figure 4.4. Regardless of the

SZA, CI_{cal} shows bimodal frequency distributions. The two peaks with lower and higher CI (square and triangle markers) correspond to the measurements under overcast and clear skies, respectively. This pattern is similar to the CI measured on Jungfraujoch (a mountain saddle in the Swiss Alps, located at an altitude of 3,570 m a.s.l) reported in Gielen et al. (2014), but different from the results measured at the low-altitude sites reported in Gielen et al. (2014) and Wagner et al. (2016). This is because the high-altitude sites are seldom influenced by anthropogenic aerosols, hence the sky is either clear or covered by clouds or fog during most of the time.

Based on this feature, we defined SZA-dependent CI thresholds for cloud screening according to the long-term frequency distribution of CI_{cal}. For each SZA (24°–85°), the threshold was defined as the CI_{cal} with the minimum probability (i.e., the valley of distribution) between the two distribution peaks, denoted as $CI_{\text{cal, valley}}$. $CI_{\text{cal, valley}}$ was determined by fitting the probability density function to a Gaussian function. The circle markers shown in Figure 4.4 indicate the determined $CI_{\text{cal, valley}}$. In order to minimize the noise, the SZA-$CI_{\text{cal, valley}}$ curve was smoothed by a 4$^{\text{th}}$ order polynomial fitting, shown as dashed curve in Figure 4.4. Finally, the smoothed $CI_{\text{cal, valley}}$ at each SZA was used as the threshold of CI_{cal} for cloud screening. The threshold values can be calculated as

$$
\begin{aligned}
CI_{\text{threshold}}(\theta) = {}& -1.304 \times 10^{-7}\theta^4 + 2.551 \times 10^{-5}\theta^3 - 1.822 \times 10^{-3}\theta^2 \\
& + 5.699 \times 10^{-2}\theta + 0.4246,
\end{aligned}
\tag{4.2}
$$

where θ is the SZA in degrees.

4.4   Summary of results

The cloud screening results during the entire measurement period (SZA $< 85°$) are summarized in Table 4.1. Among the four seasons, the percentage of cloudy measurements is highest in summer and lowest in winter. In total, about 60% of the zenith measurements were identified as cloudy scenes, and the corresponding scanning cycles were not used in the aerosol profile retrieval.

Table 4.1: Summary of cloud screening results (SZA $< 85°$).

Season	Number of measurements	Number of cloudy measurements	Percentage of cloudy measurements
Spring (Mar, Apr, May)	17,728	10,677	60.2%
Summer (Jun, Jul, Aug)	21,360	14,259	66.8%
Autumn (Sep, Oct, Nov)	24,259	13,519	55.8%
Winter (Dec, Jan, Feb)	17,007	9,264	54.5%
Annual	80,354	47,719	59.4%

Chapter 5

Retrieval of aerosol profiles

In this chapter, we present the retrieval of aerosol extinction profiles from MAX-DOAS measurements. We found the algorithms based on the optimal estimation method are not suitable for the measurements at the UFS. Therefore, we developed a new aerosol profile retrieval algorithm based on the parametrization approach.

5.1   Basic principle of aerosol profile retrieval

5.1.1   Influence of aerosols on O_4 absorption
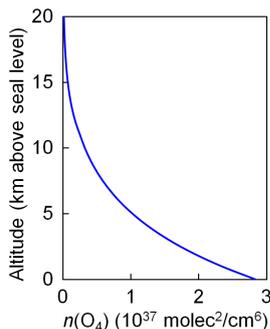
Figure 5.1: Vertical profile of O_4 (oxygen dimer) in the atmosphere (Anderson et al., 1986).

As already mentioned in Section 2.4.4, the retrieval of aerosol profiles from MAX-DOAS measurements takes advantage of O_4 absorption. O_4, also denoted as O_2-O_2, is the dimmer of oxygen molecule (O_2), and its concentration is in
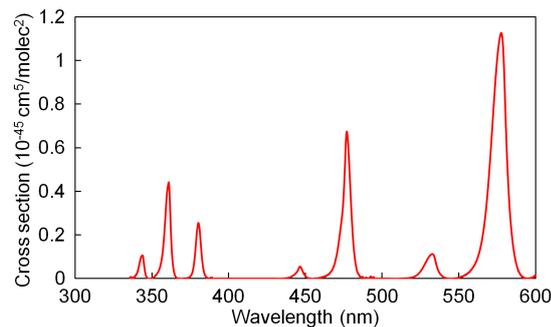
Figure 5.2: Absorption cross section of O_4 at $273\,K$ (Thalman and Volkamer, 2013).

direct proportion to the square of the concentration of O_2. As the actual concentration of O_4 is unknown, the concentration of O_4 is usually denoted as the square of the concentration of O_2 (i.e., $(molec/cm^3)^2 = molec^2/cm^6$) in atmospheric studies. Therefore, the commonly used unit of O_4 SCD and DSCD is $molec^2/cm^5$, which comes from $(molec^2/cm^6) \cdot cm$. As the vertical distribution of O_2 in the atmosphere is stable and well-known, the vertical profile of O_4 is also stable and well-known, see Figure 5.1. In addition, the concentration of O_4 decreases with increasing altitude more rapidly than that of O_2. O_4 molecules have optical absorption peaks at 360, 477, 577 and $630\,nm$ (see Figure 5.2), and the absorption can be detected by DOAS instruments. Since MAX-DOAS instruments measure the spectra of scattered sunlight at the bottom of the atmosphere, O_4 can be used as the tracer of the light path of the received photons.

Unlike direct sun instruments, all the photons received by MAX-DOAS telescopes are scattered by atmospheric molecules and aerosols. As illustrated in Figure 5.3, the total light path of the received photons can be divided into three segments:

a. In Segment (1), the incident sunlight penetrates into the atmosphere along a direct path. The penetration depth is determined by the optical depth with respect to Rayleigh and Mie scattering. It is in general larger for larger wavelength (due to the wavelength dependence of Rayleigh scattering), lower aerosol load and smaller SZA.

b. In Segment (2), the photons might enter a multiple scattering layer. Especially inside thick clouds, multiple Mie-scattering can cause extended layers of diffuse radiation in which the direction of photons would become random, see Figure 5.3 (a). However, when there are very few particles in the atmosphere, the
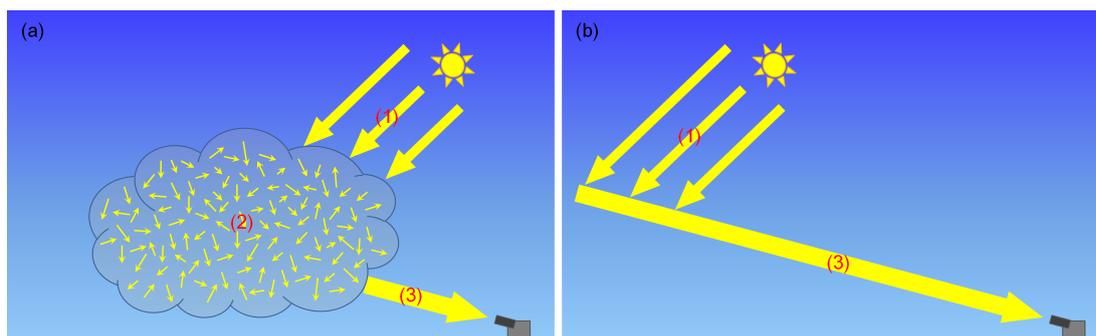
Figure 5.3: Scheme of the different segments of the atmospheric light paths for MAX-DOAS observations. Panel (a) shows the situation in an atmosphere with aerosol scattering, and Panel (b) shows the situation in an atmosphere without aerosol scattering. In each panel, (1) refers to the segment of incident direct solar radiation, (2) refers to the segment of diffuse photon scattering caused by aerosols, and (3) refers to the line of sight of the telescope.

optical depth of the atmosphere would be rather small and no significant multiple scattering layer would be established, see Figure 5.3 (b).

c. In Segment (3), the photons are scattered into the field of view of the telescope. Similar to the first segment, the length of the direct light path along the line of sight of the telescope depends on the optical depth with respect to Rayleigh and Mie scattering. For low elevations, the length of the direct light path along the line of sight is directly related to the visibility of the atmosphere close to the ground.

In a word, atmospheric aerosols can change the light path of the photons received by the MAX-DOAS telescope. Since the concentration of O_4 decreases rapidly with increasing altitude, different light paths in the atmosphere would result in different O_4 absorptions measured by MAX-DOAS instruments. The influence also differs at different measurement geometries. As the majority of the atmospheric O_4 is distributed close to the ground, the observed O_4 absorption is mostly correlated to the length of the direct line of sight of the telescope (Segment (3) mentioned above), especially for low elevations. Comparing Panel (a) to Panel (b) of Figure 5.3, additional aerosol scattering would decrease the length of the direct line of sight and hence decrease the O_4 absorption. In addition, the reduction is more significant for low elevations. On the other hand, aerosols can increase the number of scattering events, especially in the case of extended clouds. This effect would result in a simultaneous increase of the O_4 absorptions measured

at all elevations. Moreover, the characteristic distribution of atmospheric O_4 makes MAX-DOAS O_4 measurements sensitive to the vertical distribution of atmospheric aerosols. The quantitative influence of aerosols on O_4 absorption is shown in Sections 5.6.4, 5.6.5, and 5.6.6.

In order to observe the vertical distribution of aerosols in the atmosphere, MAX-DOAS instruments measure the spectra at the zenith direction and several off-zenith directions in each scanning cycle. In the retrieval, the zenith spectrum of each scanning cycle is used as the reference spectrum, and the DSCDs of O_4 are derived from the off-zenith spectra using the DOAS method. The aerosol extinction profile is then retrieved from the DSCDs of O_4.

5.1.2 Radiative transfer modeling

In order to retrieve aerosol extinction profiles from MAX-DOAS O_4 measurements, it is necessary to obtain simulated O_4 DSCDs corresponding to given atmosphere scenarios. In MAX-DOAS studies, the simulation is based on radiative transfer modeling.

The radiative transfer in the atmosphere is determined by the interactions of radiation with the atmospheric compounds and the surface of the earth. These interactions include absorption, scattering, refraction, thermal emission and reflection. The Radiative Transfer Equation (RTE) (e.g., Chandrasekhar, 1960; Stamnes et al., 1988) describes their influences on the radiance intensity. Radiative transfer models (RTMs) are aimed at solving the RTE in order to calculate the radiance intensity acquired by a specific instrument under a certain atmospheric scenario. For O_4 and other optically thin absorbers, simulated SCDs can be derived by the following equation:

$$S = \frac{\ln\left[\frac{I_0(\lambda)}{I(\lambda)}\right]}{\sigma(\lambda)}, \tag{5.1}$$

where $I_0(\lambda)$ denotes the radiance intensity at the wavelength λ simulated without the absorber of interest considered but with all the other absorbers considered, while $I(\lambda)$ refers to the intensity simulated with all absorbers considered. $\sigma(\lambda)$ is the absorption cross section of the absorber of interest. According to the definition of DSCD, simulated DSCDs can be obtained by subtracting the simulated SCD at the zenith viewing angle from the simulated SCDs at off-zenith viewing angles.

In this study, the Linearized Discrete Ordinate Radiative Transfer (LIDORT)

model (Spurr et al., 2001; Spurr, 2008) was used to simulate O_4 DSCDs and radiance intensities (except the three-dimensional simulations carried out in Section 5.5). LIDORT solves the RTE based on the discrete ordinate method. This model considers a pseudo-spherical multi-layered atmosphere which includes several anisotropic scatters. The formulation implemented corrects for the atmosphere curvature in the solar and single-scattered beams, however the multiple scattering term is treated in the plane-parallel approximation. The properties of each of the atmospheric layers are considered homogenous. Using finite differences for the altitude derivatives, this linearized code converts the problem into a linear algebraic system. Through first-order perturbation theory, it is able to provide radiance field and radiance derivatives with respect to atmospheric and surface variables (Jacobians) in a single call. LIDORT has been used in several MAX-DOAS studies to retrieve vertical profiles of aerosols or trace gases (e.g., Clémer et al., 2010; Hendrick et al., 2014; Franco et al., 2015; Wang et al., 2014a).

5.2 Retrieval based on the optimal estimation method

In most of the other MAX-DOAS studies (e.g. Frieß et al. (2006); Clémer et al. (2010); Frieß et al. (2011); Irie et al. (2011); Wang et al. (2014a, 2016); Chan et al. (2017), aerosol profiles were retrieved using the optimal estimation method (OEM) (Rodgers, 2000).

5.2.1 Principle

In OEM-based retrievals, the aerosol profile is regarded as the state parameter ($\boldsymbol{x}$), the measured O_4 DSCDs of each scanning cycle are regarded as the measurement vector ($\boldsymbol{y}$), the simulation of O_4 DSCDs is described as the forward model ($\boldsymbol{F}$), and the profile retrieval is an inverse problem. As the sensitivity of O_4 DSCD to aerosol extinction varies strongly with altitude, the retrieval is a non-linear problem. Moreover, the inverse problem is ill-posed, which means the information contained in the observation is insufficient to determine a unique solution.

The inversion of the aerosol profile is solved iteratively using the Gauss-Newton method,

$$\boldsymbol{x}_{i+1} = \boldsymbol{x}_i + (\mathbf{S}_{\mathrm{a}}^{-1} + \mathbf{K}_i^{\mathrm{T}}\mathbf{S}_{\epsilon}^{-1}\mathbf{K}_i)^{-1} \cdot [\mathbf{K}_i^{\mathrm{T}}\mathbf{S}_{\epsilon}^{-1}(\boldsymbol{y} - \boldsymbol{F}(\boldsymbol{x}_i)) - \mathbf{S}_{\mathrm{a}}^{-1}(\boldsymbol{x}_i - \boldsymbol{x}_{\mathrm{a}})], \quad (5.2)$$

where $\boldsymbol{x}_i$ denotes the state vector of the ith iteration, and $\boldsymbol{x}_{\mathrm{a}}$ is the a priori profile. $\mathbf{K}_i$ is the weighting function matrix (Jacobi matrix) of the ith iteration, which describes the sensitivity of the O_4 DSCDs to the changes in the aerosol profile. $\mathbf{S}_{\mathrm{a}}$ and $\mathbf{S}_{\epsilon}$ are the uncertainty covariance matrices of a priori and measurements, respectively. $\mathbf{S}_{\mathrm{a}}$ and $\mathbf{S}_{\epsilon}$ have different definitions in different studies (Frieß et al., 2016). In the retrieval of each scanning cycle, the state vector is first set as the a priori profile ($\boldsymbol{x}_0 = \boldsymbol{x}_{\mathrm{a}}$). The forward model is then applied to the state vector, and the state vector is corrected with Eq. (5.2). A cost function which is used to judge the convergence of the iteration is usually defined as

$$\chi^2 = [\boldsymbol{y} - \boldsymbol{F}(\boldsymbol{x})]^{\mathrm{T}} \cdot \mathbf{S}_{\epsilon}^{-1} \cdot [\boldsymbol{y} - \boldsymbol{F}(\boldsymbol{x})] + (\boldsymbol{x} - \boldsymbol{x}_{\mathrm{a}})^{\mathrm{T}} \cdot \mathbf{S}_{\mathrm{a}}^{-1} \cdot (\boldsymbol{x} - \boldsymbol{x}_{\mathrm{a}}). \quad (5.3)$$

The inversion works iteratively until the cost function is smaller than a pre-defined threshold.

5.2.2 Limitations

The MAX-DOAS aerosol profile retrieval algorithms based on the OEM have some limitations. First, as the retrieval is ill-posed and errors exist in the measurement and simulation, the profile with the lowest cost function may not be the one closest to the true profile. In addition, due to the limitation of computing power, the iteration stops once the cost function is smaller than a pre-defined threshold, which means the retrieved profile is actually not the one with the lowest cost function.

An a priori profile is needed in the OEM-based retrieval. The a priori profile not only provides the initial state vector for the iteration, but also plays a part in calculating the cost function. According to Eq. (5.3), the cost function is determined by both the difference between the measured and simulated O_4 DSCDs and the difference between the state vector and the a priori profile. This means the retrieval minimizes both of the two differences. As a result, if the a priori profile is largely different from the true profile, the retrieval might be misled. Moreover, as the measurement sensitivity decreases rapidly with increasing altitude, the

higher part of the retrieved profile is mostly dominated by the a priori profile. The constrain from the a priori profile can be adjusted by changing the definition of its uncertainty covariance matrix $\mathbf{S}_a$. The constrain should be neither too strong nor too weak. If the constrain is too strong, the retrieval would be much too dependent on the a priori profile; on the other hand, a weak constrain might result in unreasonable results with large vibrations. The optimal definition of $\mathbf{S}_a$ differs for different sites and different aerosol loads. In some cases, the balance between freedom and restrain can hardly be reached.

At the UFS and other high-altitude sites, the aerosol profile retrieval is more challenging for several reasons:

a. Due to the high altitude, the O_4 concentration is much lower than the typical low-altitude sites, therefore the measurement sensitivity is systematically lower. The O_4 concentration at the altitude of the UFS is 41% lower than at sea level.

b. The complicated ground topography at mountainous sites can also bring errors to the radiative transfer simulations (see Section 5.5).

c. It is found in many MAX-DOAS studies that O_4 DSCDs need to be corrected by a scaling factor (see Section 5.10). However, the scaling factors for high altitude measurements are unclear.

d. The aerosol load at high-altitude sites is usually much lower than urban areas, so that the vertical gradient of aerosol extinction is also much smaller and the influence from aerosols above the retrieval height is hence much stronger.

As a result, the SNR of such high-altitude MAX-DOAS measurements is often insufficient to have a stable retrieval.

5.2.3   Retrieval of synthetic measurement data

In order to test the performance of OEM-based aerosol profile retrieval algorithms for the MAX-DOAS measurements at the UFS, we generated some synthetic O_4 DSCDs and then retrieved aerosol profiles from the synthetic data using an OEM-based algorithm.

With each true aerosol extinction profile, O_4 DSCDs at 360 and 477 nm and at the elevations of 1°, 2°, 5°, 10°, 20° and 30° were first simulated using LIDORT. In the simulation, the ground surface was defined as a flat surface at the altitude of the UFS, i.e., 2,650 m above sea level. The definitions of surface albedo, single scattering albedo, phase function and climatology followed the common settings

of the further simulations in this chapter, listed in Table 5.5. For the example shown in this section, the solar position was set as $\text{SZA} = 60°$ and RAA (relative solar azimuth angle) $= 60°$.

Aerosol profiles were then retrieved from the synthetic O_4 DSCDs using the BePRO profiling tool developed at BIRA-IASB (Clémer et al., 2010; Hendrick et al., 2014). BePRO uses LIDORT as the forward model, which is the same as the RTM used in generating the synthetic data. The parameters related to forward simulation were also defined as same as those in generating the synthetic data. The retrieval grid was defined as 20 layers of 200 m thickness each.

BePRO constructs the uncertainty covariance matrix of a priori ($\mathbf{S}_a$) as follows: in each iteration, the diagonal element of $\mathbf{S}_a$ corresponding to the bottom layer, $\mathbf{S}_a(1,1)$, is set as the square of a scaling factor β times the maximum partial AOD of the profiles; the other diagonal elements decrease linearly with increasing altitude to $0.2 \times \mathbf{S}_a(1,1)$; the off-diagonal elements are defined using Gaussian functions with a correlation length γ:

$$\mathbf{S}_a(i,\, j) \,=\, \sqrt{\mathbf{S}_a(i,\, i) \,\cdot\, \mathbf{S}_a(j,\, j) \,\cdot\, \exp\left[-\, (\ln 2) \,\cdot\, \left(\frac{z_i \,-\, z_j}{\gamma}\right)^2 \right]}, \qquad (5.4)$$

where z_i and z_j are the altitudes of the ith and j^{th} layers, respectively (Clémer et al., 2010; Wang et al., 2014a). The constrain from a priori profile can be adjusted by changing β and γ.
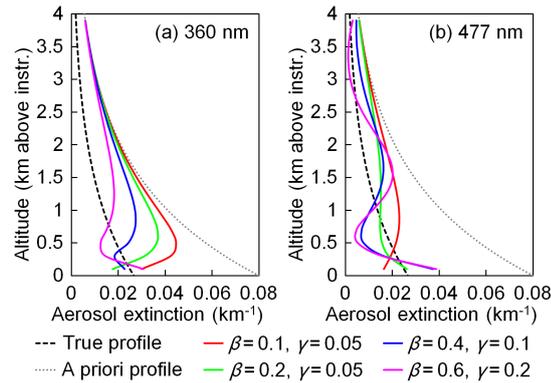
Figure 5.4: Retrieval results of a set of synthetic data at (a) 360 nm and (b) 477 nm, retrieved using BePRO. In each chart, the black dashed curve shows the true profile, the gray dotted curve shows the a priori profile of retrieval, and the solid curves in four different colors show the aerosol profiles retrieved with four different definitions of the uncertainty covariance matrix of a priori ($\mathbf{S}_a$).

Figure 5.4 shows an example of the retrieval. Panels (a) and (b) show the results of 360 and 477 nm, respectively. In each panel, the black dashed curve shows the true profile, with which the synthetic O_4 DSCDs were simulated. In this example, the true profile is an exponential profile of which the total AOD (τ) is 0.04 and the scaling height (SH) is 1.5 km. The aerosol extinction at each altitude follows the following expression:

$$\sigma(z) = \frac{\tau}{SH} \cdot \exp\left(-\frac{z}{SH}\right), \tag{5.5}$$

where $\sigma(z)$ is the aerosol extinction coefficient at z km above the MAX-DOAS instrument (2,650 m above sea level). Therefore, the surface aerosol extinction coefficient is $0.0267 \, \text{km}^{-1}$. The gray dotted curve shows the a priori profile of retrieval, which was defined as an exponential profile with $\tau = 0.12$ and SH = 1.5 km. The solid curves in four different colors show the aerosol profiles retrieved with four different definitions of $\mathbf{S}_a$. Among the four profiles, the red curve was retrieved with the strongest constrain from the a priori profile, while the magenta curve was retrieved with the weakest constrain.

The results show that at both of the two bands, none of the retrieved profiles can reproduce the true profile. Especially at higher altitudes, even if the constrain from the a priori is set to be rather weak, the retrieved profile is still dominated by the a priori. This is because the MAX-DOAS measurements can provide very limited information for the aerosols at higher altitude. At lower altitudes, the true profile cannot be well reproduced with any of the four settings, either. In real retrievals, due to the existence of error and noise in measurement and simulation, it is even more difficult to get reliable results.

5.3   Retrieval using the parametrization approach

Besides the OEM-based algorithms, in some other MAX-DOAS studies (e.g., Lee et al., 2009; Li et al., 2010b; Vlemmix et al., 2011; Wagner et al., 2011; Wang, 2012; Sinreich et al., 2013), aerosol profiles were retrieved using the parametrization approach. Based on the fact that the information content of each MAX-DOAS measurement cycle is typically limited to only 2–3 independent pieces of information for the retrieved vertical profiles (Frieß et al., 2006; Clémer et al., 2010), aerosol profiles were simplified as a few parameters in these studies. These retrieval algorithms are usually based on the look-up table (LUT) method, which

means the O_4 DSCDs corresponding to a limited number of aerosol profiles and viewing geometries (with discrete values of the profile parameters and viewing geometry) are pre-calculated and stored. The LUT was used as the forward model, so that the computational effort can be reduced.

In the study of Li et al. (2010b), it was assumed that the the aerosol extinction coefficient within the PBL does not change with the altitude, while the aerosol extinction coefficient in the free troposphere exponentially decreases with the increasing altitude with a fixed SH. Aerosol profiles were defined by only three parameters: the AOD, the fraction of aerosols in the PBL, and the height of the PBL. The modeled O_4 DSCDs corresponding to 720 possible aerosol profiles and 13 SZA-RAA combinations were pre-calculated and stored in a LUT. The aerosol profiles were retrieved by minimizing the difference between modeled and measured O_4 DSCDs. The minimization procedure was conducted using the Levenberg-Marquardt algorithm.

In the study of Wagner et al. (2011), aerosol profiles were also defined by three parameters: the AOD, the layer height, and the shape parameter which describes the relative shape of aerosol profiles. Profiles with elevated layers were also considered. A LUT which includes 250,000 O_4 DAMF (differential air mass factor, in direct proportion to DSCD) data was created. In the aerosol profile inversion process, only the AOD and the layer height were varied, while the shape parameter was fixed. In a first step, the optimum AOD was determined for the discrete values of the aerosol layer height defined for the LUT. In a second step, a low order polynomial as a function of the aerosol layer height was fitted to the determined residual sum of squares between the measured and modeled O_4 DAMFs. The optimum AOD and layer height were derived according to the minimum of the polynomial. The fitting process was conducted for different shape parameters.

Comparing to the optimal estimation approach, the parametrization approach was found to be more stable and robust, however, it cannot retrieve complex profiles (Wagner et al., 2011). In this chapter, we present a new aerosol profile retrieval algorithm developed by us. The algorithm is also based on the parametrization approach, and the LUT method is used in the retrieval.

5.4 O_4 DSCD calculation

O_4 DSCDs were retrieved from both UV and VIS spectra using the DOAS method (see Chapter 2). The fitting windows were determined according to both the absorption signal of O_4 and the SNR of the spectrometer. The fitting window of the UV spectra was defined as 338–370 nm, which is the same as most of the other MAX-DOAS studies, and it covers the strong absorption peak at 360.8 nm and a weak absorption peak at 344 nm. For the VIS spectra, because the spectral range of our spectrometer starts from 427 nm and the SNR near the border is low, the fitting window was determined to be 440–490 nm, which is somewhat narrower than the fitting window of 425–490 nm commonly used in other MAX-DOAS studies (e.g., Clémer et al., 2010; Chan et al., 2017; Kreher et al., 2019). The VIS fitting window covers the strong absorption peak at 477 nm and a weak absorption peak at 446.5 nm.

In the aerosol profile retrieval, the DSCD is defined as the difference between the SCD of each off-zenith spectrum (elevation angle $\alpha \neq 90°$) and the SCD of the zenith spectrum ($\alpha = 90°$) measured at the same time. As the off-zenith and zenith spectra could not be measured simultaneously in the real measurements, we temporally interpolated the zenith spectra before and after each scanning cycle to the measurement time of each off-zenith spectrum, and the interpolated spectrum was used as the reference spectrum.

Details of the DOAS fit settings for both bands are listed in Table 5.1. The broad band spectral structures caused by Rayleigh and Mie scattering were removed by including a low order polynomial in the DOAS fit. Absorption cross sections of several trace gases as well as a synthetic Ring spectrum were included in the DOAS fit (See Section 2.5.2). The so-called intensity offset refers to the Fraunhofer reference spectrum included in the DOAS fit, which is used to minimize the influence from the Fraunhofer lines (see Section 2.5.1). As the temperature at the UFS typically varies between 263 K and 279 K (Risius et al., 2015), trace gas absorption cross sections measured at 273 K were used in the DOAS fit. For NO_2 and O_3, as their absorption cross sections vary strongly with the temperature, two cross sections at different temperatures were included in the fitting. This setting was first suggested in Van Roozendael et al. (2002) and commonly used in other MAX-DOAS studies. Small shift and squeeze of the wavelengths were allowed in the wavelength mapping process in order to compensate small uncertainties caused by the instability of the spectrograph. In this study, the

spectra evaluation software QDOAS (version 3.2) developed at BIRA-IASB was used for the spectral fitting analysis.

The root mean square (RMS) of fitting residual was used to evaluate the performance of the DOAS fit. DSCDs with a residual RMS larger than 1×10^{-3} were filtered out in the following analysis. Under cloud-free conditions, the residual RMS of most of the UV spectra varies between 5×10^{-4} and 9×10^{-4}, while the residual RMS of most of the VIS spectra varies between 2×10^{-4} and 5×10^{-4}. This is because both the light intensity and the O_4 absorption are stronger at the VIS band; hence the measurement SNR is higher.

Figure 5.5 and Figure 5.6 show examples of the DOAS fitting in the UV and VIS bands, respectively. In each figure, the off-zenith spectrum ($\alpha = 1°$) is shown as the red curve in Panel (a), and the reference spectrum (i.e., the interpolated zenith spectrum at the same time) is shown as the blue curve. Both of the two spectra have been corrected for offset and dark current. In Panel (b), the red curve is the total optical density (D), which is the negative of the logarithm of the ration between the off-zenith and reference spectra, while the blue curve is the 5th order polynomial derived by the DOAS fitting. The difference between the total optical density and the polynomial is shown as the red curve in Panel (c), and the black curve in Panel (c) is the sum of all the absorptions. The difference between the two curves in Panel (c) is the fitting residual, shown as the gray curve in Panel (d). The RMS of the fitting residual is indicated at the bottom of Panel (d). The absorptions of all the fitting species derived by the DOAS fitting are shown in Panels (e_1) and (e_2). Panel (e_2) is the magnification of Panel (e_1), in which the absorptions of minor species can be seen clearly.

Figure 5.7 shows the O_4 DSCDs at the UV and VIS bands measured during the daytime of 07 December 2015. The SZAs and RAAs are also shown in Panels (a) and (b), respectively. The sky was clear without clouds during the entire day. The results indicate that at both bands, the O_4 DSCDs are lowest at noon and decrease with increasing viewing elevation angle.

Table 5.1: The DOAS fit settings for UV (338–370 nm) and VIS (440–490 nm) bands.

Species	Temperature	Fitting window UV	VIS	Reference
CHOCHO	296 K		✓	Volkamer et al. (2005b)
HCHO	273 K	✓		Chance and Orphal (2011)
H_2O	296 K	✓	✓	HITEMP 2010, Rothman et al. (2010)
NO_2[a]	273 K	✓	✓	Bogumil et al. (2003)
NO_2[a]	220 K	✓	✓	Bogumil et al. (2003)
O_3[b]	273 K	✓	✓	Serdyuchenko et al. (2014)
O_3[b]	223 K	✓	✓	Serdyuchenko et al. (2014)
O_4	293 K	✓	✓	Thalman and Volkamer (2013)
Ring		✓	✓	Calculated by QDOAS
Polynomial		5th order	5th order	
Intensity offset		linear	linear	

[a] I_0 correction is applied with SCD of 1×10^{17} molec/cm² (Aliwell et al., 2002).
[b] I_0 correction is applied with SCD of 1×10^{20} molec/cm² (Aliwell et al., 2002).
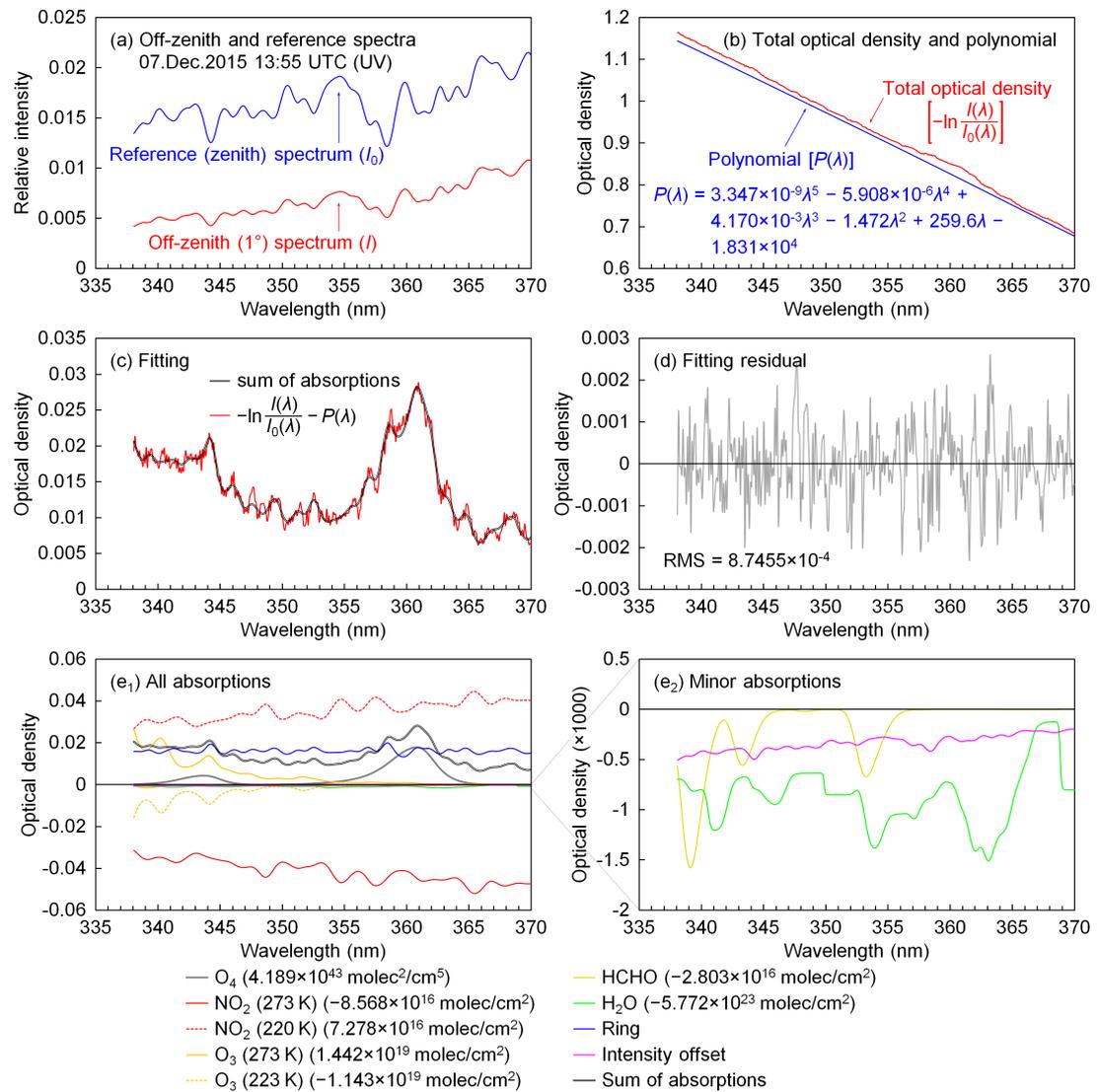
Figure 5.5: An example of the DOAS fitting in the UV band. The off-zenith spectrum was measured on 07 Dec 2015 at 13:55 UTC, at the elevation of 1°. (a) Off-zenith spectrum (I, red curve) and zenith reference spectrum (I_0, blue curve). (b) Total optical depth (D, red curve) and the fitted polynomial (P, blue curve). (c) Sum of all absorptions (black curve) and the difference between the total optical depth and fitted polynomial (red curve). (d) Fitting residual. (e_1) Absorptions of all the fitting spicies derived by the DOAS fitting. (e_2) Magnification of Panel (e_1), absorptions of minor species.
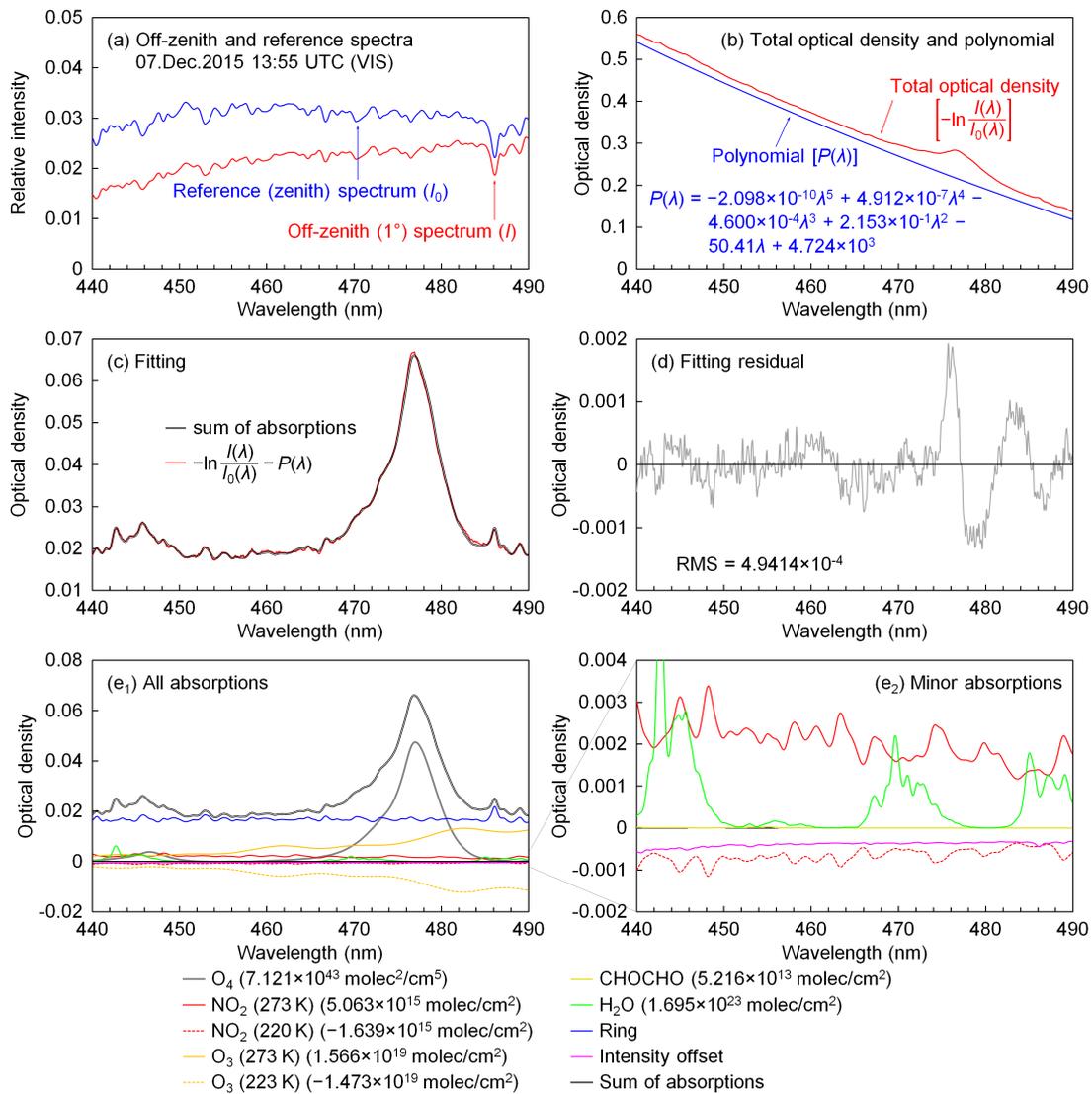
Figure 5.6: Same as Figure 5.5, but for the VIS band.

5.5 Topography effect and the simplification in RTM

[1]

The topography around the UFS is quite complex, which complicates the radiative transfer simulations. As shown in Figure 3.5, the surface altitude varies between 600 and 2,800 m a.s.l. along the viewing direction of the MAX-DOAS

---

[1]Due to the complexity of TRACY-2, the radiative transfer simulations presented in this section were performed by Prof. Dr. Thomas Wagner (MPIC-Mainz).
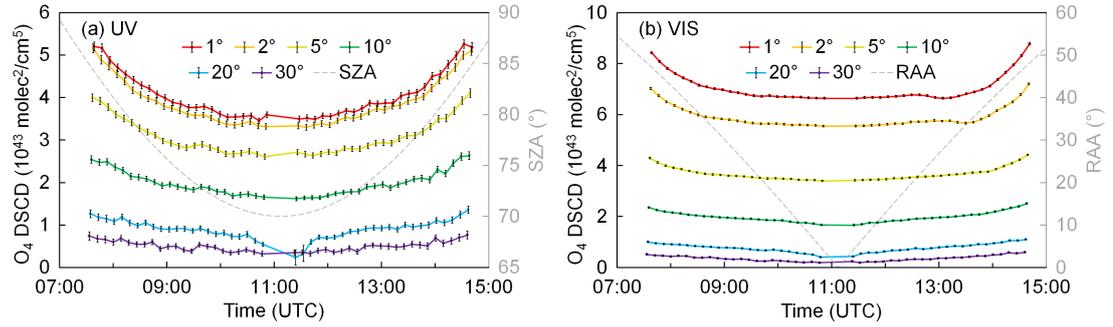
Figure 5.7: O_4 DSCDs at (a) UV and (b) VIS bands measured during the daytime of 07 Dec 2015, as well as the SZAs and RAAs. The error bars represent the uncertainty calculated from the RMS of fitting residual.

instrument. Figure 3.5 (b) also shows the type of surface in different colors which includes forests, meadows, rocks, etc. Some parts of the surface are seasonally or permanently covered by snow, while some steep slopes cannot be covered by snow even in winter.

Three-dimensional RTMs can consider such a complex terrain, but they are computational expensive and unaffordable for retrieval. Due to the limitation of the two-dimensional RTM LIDORT used in the study, we simplified the ground topography to a flat surface at an altitude of 2,650 m a.s.l in the radiative transfer simulations. In order to estimate the error caused by this simplification, we investigated the error using the three-dimensional RTM TRACY-2.

TRACY-2 is a full spherical Monte-Carlo atmospheric RTM (Deutschmann, 2008; Wagner et al., 2007), which allows to simulate three-dimensional radiative transport as well as two-dimensional variation of the surface height. The model was compared to other RTMs and very good agreement was found (Wagner et al., 2007). We also did an inter-comparison with LIDORT. The result shows that with the same definition of topography and atmosphere, the difference between the O_4 DSCDs simulated by the two RTMs is less than 3%.

For the three-dimensional simulations carried out in this study, a pseudo-reality topography was defined with the exact ground altitude (obtained from Google Earth) in the azimuth direction of the MAX-DOAS measurements taken into account, whereas in the dimension orthogonal to this direction, the surface altitude was set constant. This simplification was chosen to reduce the computational effort. Since the atmospheric light paths in the viewing direction of the instruments can be very long (up to several tens of kilometers), whereas the in-

fluence of the orography perpendicular to this direction is expected to be small, the influence from only the topography along the viewing direction is quantified in a first step.

Simulations were performed with all combinations of three different SZAs (30°, 50° and 70°), three different RAAs (30°, 60° and 90°) and two different aerosol extinction profiles (an aerosol-free profile and a box-shape profile with AOD = 0.12 and box height = 3 km), i.e., altogether 18 cases. For each case, O_4 DSCDs at 360 and 477 nm were simulated with both the flat surface at 2,650 m and the pseudo-reality topography using TRACY-2. The relative differences of O_4 DSCDs simulated with the flat surface comparing to those simulated with the pseudo-reality topography were then calculated. A fixed surface albedo of 0.07 was used in the simulations. For both wavelengths, the single scattering albedo was set to 0.93 and the phase function was defined as a Henyey-Greenstein phase function with the asymmetry parameter set to 0.68. The atmospheric profile was defined as the US standard mid-latitude atmosphere (Anderson et al., 1986). Figure 5.8 shows the results of some of the cases: (a) and (b) show the results of six cases with SZA = 50° and different RAAs and both aerosol extinction profiles; (c) and (d) show the results of six cases with RAA = 60° and different SZAs and also both aerosol extinction profiles.

Table 5.2: Systematic and random errors caused by the topography simplification. Results were calculated from the relative differences of O_4 DSCDs simulated with a flat surface at 2,650 m comparing to those simulated with the pseudo-reality surface in 18 cases (see text). The mean of the relative difference of each elevation and each wavelength was considered as the systematic error. The standard deviation of the relative difference was considered as the random error.

Elevation angle	UV (360 nm)		VIS (477 nm)	
	Systematic error (%)	Random error (%)	Systematic error (%)	Random error (%)
1°	-3.19	1.99	-2.30	2.24
2°	-3.69	1.64	-1.90	2.21
5°	-3.42	1.60	-2.48	1.57
10°	-4.12	2.32	-3.51	2.24
20°	-4.74	3.09	-3.93	4.63
30°	-5.08	5.44	-3.91	5.84

As shown in all the panels of Figure 5.8 as well as in all the other cases which are not shown, O_4 DSCDs simulated with the flat surface are in general
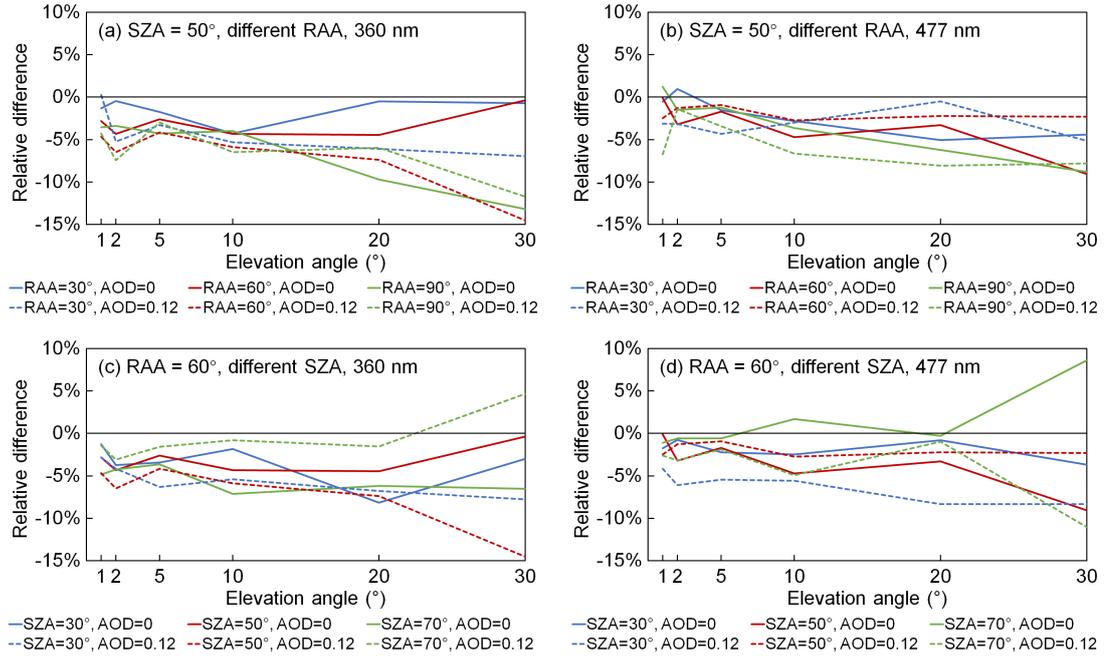
Figure 5.8: Relative differences of O_4 DSCDs at (a, c) 360 nm and (b, d) 477 nm simulated with a flat surface at 2,650 m comparing to the O_4 DSCDs simulated with the pseudo-reality topography. (a) and (b) show the results simulated with the same SZA of 50° and different RAAs of 30°, 60° and 90°; (c) and (d) show the results simulated with the same RAA of 60° and different SZAs of 30°, 50° and 70°. Solid lines are the results simulated under aerosol-free condition, and dashed lines are the results simulated with a box-shape profile with AOD = 0.12 and box height = 3 km.

slightly underestimated comparing to the pseudo-reality topography. The difference could be explained by the scattering in the valleys where the concentration of O_4 is higher. For the flat surface at 2,650 m, the light paths below 2,650 m would not be taken into account, and hence the O_4 DSCDs would be underestimated. Moreover, the relative error has no obvious correlation with the elevation angle, SZA, RAA or aerosol load. This is because the light path below 2,650 m is influenced by the topography, and the influence differs with the observation geometry. In addition, the light path is also influenced by the aerosols both below and above 2,650 m. Concerning the fact that only a pseudo-reality surface and a constant surface albedo was used in the study, the actual error caused by the topography simplification is expected to be much more complicated.

In order to make the compensation feasible, we considered the error as the combination of a systematic error and a random error. Based on the results of all

the 18 cases in this study, the mean bias of each elevation and each wavelength was considered as the systematic error, while the standard deviation of the relative difference was considered as the random error, see Table 5.2. In the aerosol profile retrieval, systematic errors were first corrected from the measured O_4 DSCDs, while random errors were included in the error budget in the calculation of cost functions (see Section 5.8.2). In the following text of this chapter, measured O_4 DSCDs refer to the values corrected by the systematic error unless otherwise mentioned.

5.6   Sensitivity analysis

In order to make full use of the measurement sensitivity and reduce unnecessary computational efforts, our retrieval algorithm was designed according to the sensitivity of O_4 absorption. We performed several sensitivity tests to determine the optimal vertical grid, step size of the aerosol extinction for each layer and the maximum aerosol extinction. In addition, these sensitivity tests also help to estimate the measurement and model errors which are very important for the retrieval. The sensitivity tests are based on the forward simulations of O_4 DSCDs using LIDORT.

We investigated the sensitivity of O_4 absorption to surface albedo, single scattering albedo (SSA), scattering phase function, aerosol layer thickness, aerosol extinction above retrieval height, and surface aerosol extinction. In the test of each parameter, O_4 DSCDs at 360 and 477 nm and at the six off-zenith elevations were simulated with the parameter being tested set as different values, while all the other parameters were fixed. In this section, we only present the results of the sensitivity tests under the common settings listed in Table 5.3 (except for Section 5.6.1, in which the results of an additional test with an aerosol-free profile are also shown). In the following subsections, all the unmentioned simulation parameters followed the common settings. The extreme and median values of each parameter are also discussed in the following subsections.

5.6.1   Sensitivity to surface albedo

It is difficult to determine the exact surface albedo around the measurement site. In other studies, the surface albedo at low-altitude sites was usually estimated to be 0.05–0.1 (e.g., Irie et al., 2008; Ma et al., 2013; Wagner et al., 2011; Chan et al.,

Table 5.3: The common settings for sensitivity studies.

Parameter	Value or definition
Topography	A flat surface at an altitude of 2,650 m a.s.l.
Solar zenith angle (SZA)	60°
Relative solar azimuth angle (RAA)	60°
Surface albedo	0.1
Single scattering albedo (SSA)	0.93 (360 nm) / 0.92 (477 nm)
Phase function	The 'median' phase function defined in Section 5.6.3
Aerosol extinction profile	Box-shape profile with AOD = 0.12 and box-height = 3 km (i.e., $\sigma = 0.04\,\mathrm{km^{-1}}$ for 2,650–5,650 m a.s.l. and $\sigma = 0$ for altitude > 5,650 m)
Climatology	US standard profiles for profile, temperature and trace gas profiles

2017; Li et al., 2010b; Clémer et al., 2010; Li et al., 2013; Wang et al., 2016), while at a high-altitude site, it was estimated to be 0.2 (Franco et al., 2015). As for the UFS, on the one hand, the snow covers and naked rocks are more reflective than the typical urban and rural surfaces; on the other hand, the deep valleys close to the site can significantly decrease the surface albedo. In addition, the measurements at different elevations might be sensitive to different parts of the surface. The effective surface albedo also depends on the observation geometry. The forming and melting of the snow cover can affect the surface albedo as well. However, the RTM can only assume a constant surface albedo. Therefore, we have to estimate a variation range of the surface albedo and consider the possible uncertainty in the retrieval. In this study, we empirically estimated that the surface albedo varies between 0.025 and 0.2 with a median value of 0.1 for both 360 and 477 nm.
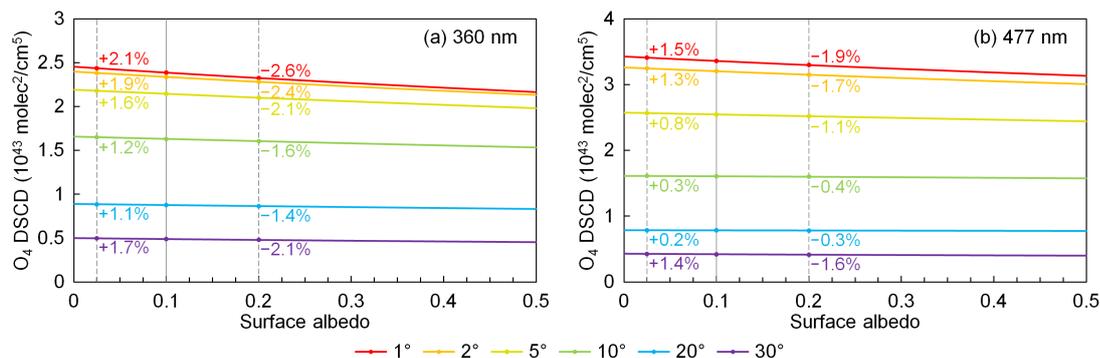
Figure 5.9: O_4 DSCDs at (a) 360 nm and (b) 477 nm simulated with different surface albedo values between 0 and 0.5. The other simulation parameters followed the settings listed in Table 5.3. The gray solid line refers to the empirically estimated median surface albedo value of 0.1, and the gray dashed lines refer to the extreme values of 0.025 and 0.2 defined in the study. The relative differences between the O_4 DSCDs simulated with extreme surface albedo values (0.025 and 0.2) and the ones simulated with the median value (0.1) are noted in the charts.

Figure 5.9 shows the O_4 DSCDs simulated with the surface albedo varying between 0 and 0.5 (with a step size of 0.025), while the other parameters were fixed as the settings listed in Table 5.3. The empirically estimated median surface albedo value of 0.1 is marked as the gray solid line, and the extreme values of 0.025 and 0.2 are marked as the gray dashed lines. For each elevation, the relative percentage differences of the O_4 DSCDs simulated with the extreme surface albedo values comparing to the one simulated with the median value are marked

beside the data points. The results show that at all the elevations and at both 360 and 477 nm, O_4 DSCD slowly decreases with increasing surface albedo.
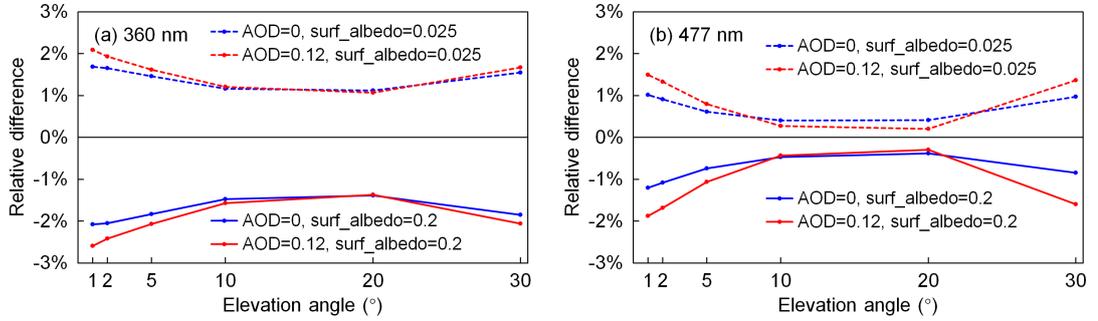
Figure 5.10: Relative differences of O_4 DSCDs at (a) 360 nm and (b) 477 nm simulated with extreme surface albedo values (solid lines for 0.2 and dashed lines for 0.025) comparing to O_4 DSCDs simulated with the median value (0.1). The blue lines refer to the results under aerosol-free condition, while the red lines refer to the results with a box-shape profile with AOD = 0.12 and box height = 3 km. The other simulation parameters followed the settings listed in Table 5.3.

Besides the box-shape aerosol profile with AOD = 0.12 defined in the common settings, we also did a similar test with an aerosol-free profile. The percentage differences of the O_4 DSCDs corresponding to extreme surface albedo values from both of the tests are summarized in Figure 5.10.

The results show that at both wavelengths and under both aerosol profiles, O_4 DSCDs at all the six elevations slightly decrease with increasing surface albedo, and the variation rate differs with different elevation angles and different aerosol loads. Based on our estimation of the median value and variation range of surface albedo, the uncertainty caused by surface albedo would be less than 3%, and the positive and negative errors are nearly equal. Further simulations show that the uncertainty caused by surface albedo also depends on the observation geometry.

5.6.2 Sensitivity to single scattering albedo

As the aerosol optical property data at the UFS were not available, we estimated the aerosol optical properties from the AERONET data at Hohenpeißenberg (see Section 3.3.2). As shown in Figure 5.11, according to the long-term single scattering albedo (SSA) data, 90% of the SSA at 360 nm vary between 0.87 and 0.997, and the median value is 0.93; for the SSA at 477 nm, 90% of the data vary between 0.85 and 0.997, and the median value is 0.92.
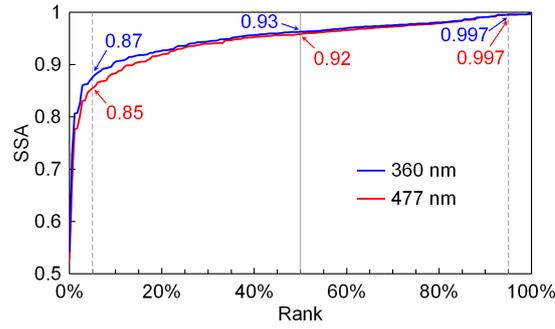
Figure 5.11: Cumulative distribution of the single scattering albedo (SSA) at 360 and 477 nm, derived from the AERONET data at Hohenpeißenberg from 2013 to 2014.
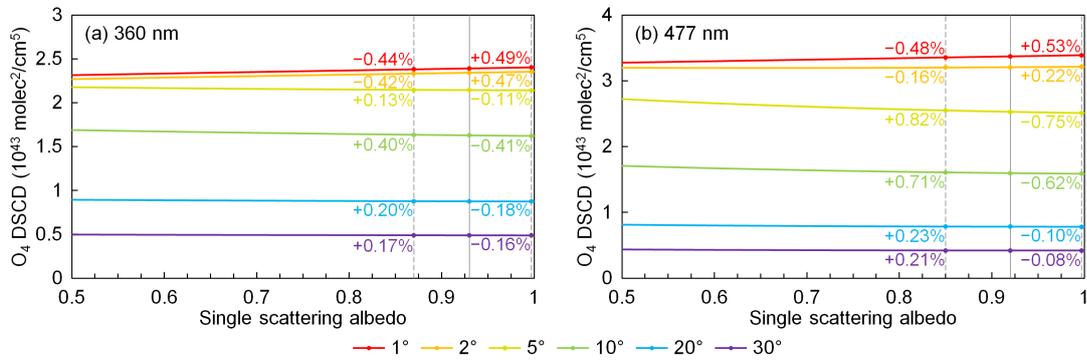
Figure 5.12: O_4 DSCDs at (a) 360 nm and (b) 477 nm simulated with different single scattering albedo values between 0.5 and 1 (step size 0.025, the extreme and median values were also included). The other simulation parameters followed the settings listed in Table 5.3. The gray solid line indicates the empirically estimated median single scattering albedo value (0.93 for 360 nm and 0.92 for 477 nm), and the gray dashed lines indicate the extreme values (0.87 and 0.997 for 360 nm, 0.85 and 0.997 for 477 nm). The relative differences between the O_4 DSCDs simulated with extreme single scattering albedo values and the one simulated with the median value are noted in the charts.

In order to estimate the uncertainty of simulated O_4 DSCD due to the SSA, we simulated O_4 DSCDs with the SSA varies from 0.5 to 1 (with a step size of 0.025, and the above-mentioned extreme and median values were also included), while the other parameters were fixed as the settings listed in Table 5.3. The results are shown in Figure 5.12. In each chart, the gray solid line indicates the median SSA value, while the gray dashed lines indicate the extreme values. For each elevation, the relative percentage differences of the O_4 DSCDs simulated

with the extreme SSA values comparing to the one simulated with the median value are marked beside the data points.

The results show that at different elevations, O_4 DSCD either slowly decreases or slowly increases with increasing SSA. The results also indicate that using the median SSA value in the forward simulation would result in less than 1% error in O_4 DSCDs in 90% of the cases. In addition, the positive and negative errors are mostly equal. Since the simulation error attributed to SSA is rather small, using the SSA data from Hohenpeißenberg should not have a big influence on the retrieval, although that site is located at a much lower altitude comparing to the UFS.

5.6.3 Sensitivity to scattering phase function
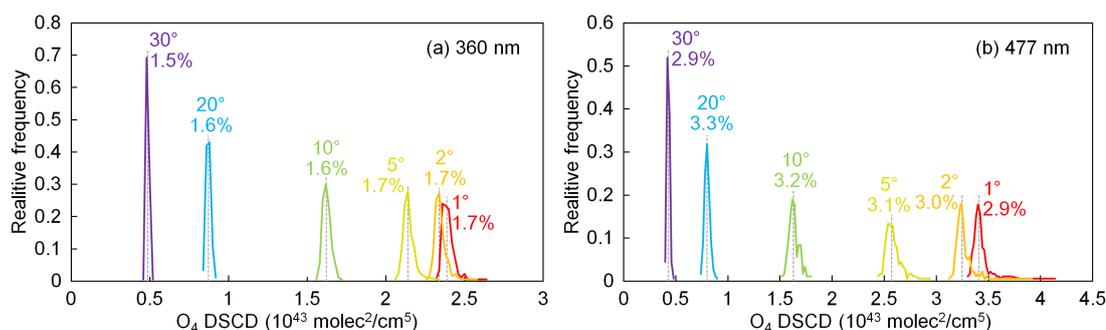
Figure 5.13: Frequency distributions of O_4 DSCDs at (a) 360 nm and (b) 477 nm simulated with all the phase functions during 2013–2014. The other simulation parameters followed the settings listed in Table 5.3. The percentage standard deviation of the simulated O_4 DSCDs at each elevation is labeled in the plots. The gray dashed lines represent the median values of simulated O_4 DSCDs at each elevation.

The estimation of the uncertainty of simulated O_4 DSCD due to scattering phase function is also based on the AERONET data at Hohenpeißenberg. Unlike most of the other simulation parameters which can be defined by a single number, the parameter of scattering phase function is defined by function values at different scattering angles. In order to estimate the uncertainty, we simulated O_4 DSCDs with all the phase function data from 2013 to 2014 (altogether 179 available data), while the other parameters were fixed as the settings listed in Table 5.3. The frequency distributions of simulated O_4 DSCDs are shown in Figure 5.13. For each elevation, the percentage standard deviation is marked beside the curve,

and the gray dashed line indicates the median value. The results indicate that the distributions of the simulated O_4 DSCDs follow the normal distribution, and the standard deviations at 477 nm are larger comparing to 360 nm. In addition, the simulation uncertainty caused by phase function is 3–5 times larger than that caused by SSA and comparable to the uncertainty caused by the surface albedo.

Based on the simulation results, the phase function with which the simulated O_4 DSCDs at all the elevations are closest to the median values was chosen as the so-called 'median' phase function for each wavelength.

5.6.4   Sensitivity to aerosol layer thickness
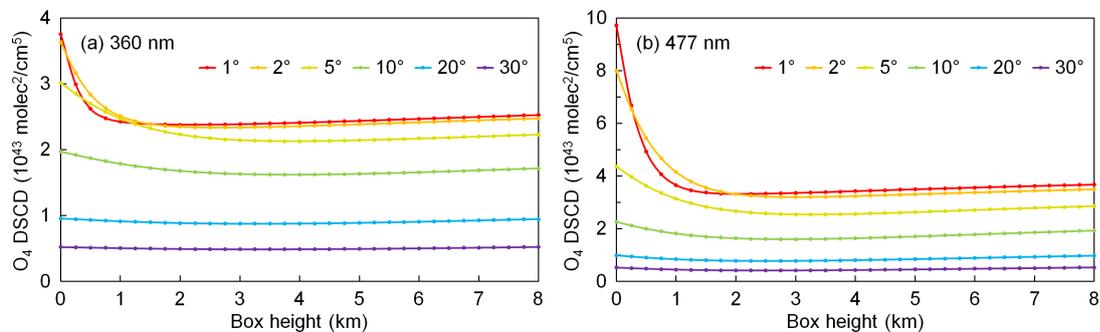
Figure 5.14: Simulated O_4 DSCDs at (a) 360 nm and (b) 477 nm for box-shape profiles with the same surface aerosol extinction coefficient of $0.04\,\mathrm{km^{-1}}$ and different box heights from 0 to 8 km. The other simulation parameters followed the settings listed in Table 5.3.

The sensitivity of O_4 DSCD to aerosol layer thickness was estimated by simulating O_4 DSCDs with box-shape aerosol profiles with the same aerosol extinction coefficient of $0.04\,\mathrm{km^{-1}}$ and different box heights varying from 0 to 8 km. The other parameters were fixed as the settings listed in Table 5.3. The simulated O_4 DSCDs are shown in Figure 5.14.

The results indicate that the sensitivity of O_4 DSCD at all the elevations decreases rapidly with increasing aerosol layer thickness (and also increasing AOD). Furthermore, O_4 DSCDs at all the elevations are almost constant when the thickness varies between 2 and 8 km, which indicates that O_4 absorption is insensitive to the aerosols above 2 km. Taking the O_4 DSCD at 360 nm and at the elevation of 2° as an example, the sensitivity to aerosols at 2 km is lower than that at the surface level by a factor of ∼40. In addition, measurements at lower elevations are more sensitive to aerosols close to the ground comparing to higher elevations.

This result coincides with the results reported in the MAX-DOAS studies based on the OEM (e.g., Frieß et al., 2006; Clémer et al., 2010; Frieß et al., 2016; Bösch et al., 2018). In these studies, the averaging kernels — which indicate the measurement sensitivities to aerosols at different altitudes — are all close to zero at the altitudes above 2 km.

5.6.5 Sensitivity to aerosol extinction above retrieval height
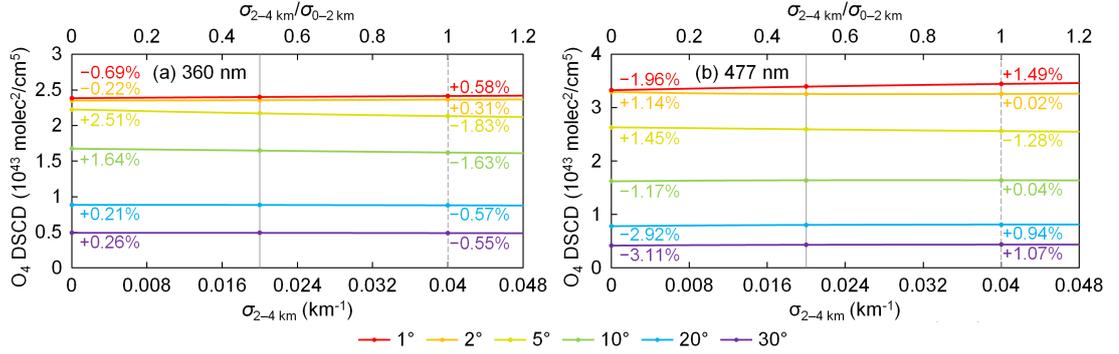
Figure 5.15: Simulated O_4 DSCDs at (a) 360 nm and (b) 477 nm for profiles with the same aerosol extinction coefficient of $0.04 \, \text{km}^{-1}$ between 0 and 2 km above instrument and different aerosol extinction coefficients varying from 0 to $0.048 \, \text{km}^{-1}$ between 2 and 4 km. The other simulation parameters followed the settings listed in Table 5.3. The gray solid line refers to the empirically estimated median $\sigma_{2-4 \, \text{km}}$ value of $0.02 \, \text{km}^{-1}$ (i.e., 50% of $\sigma_{0-2 \, \text{km}}$), and the gray dashed lines refer to the extreme values of 0 and $0.04 \, \text{km}^{-1}$ (i.e., 0% and 100% of $\sigma_{0-2 \, \text{km}}$). The relative differences between the O_4 DSCDs simulated with extreme $\sigma_{2-4 \, \text{km}}$ values and the ones simulated with the median $\sigma_{2-4 \, \text{km}}$ are noted in the charts.

According to the conclusion of Section 5.6.4, our retrieval of aerosol profiles would mainly focus on aerosols below 2 km above instrument. However, as the aerosol load on Zugspitze is usually very low and the aerosol extinction coefficient above 2 km is usually in the same order of magnitude with the one below 2 km. We estimate that the aerosol extinction coefficient between 2 and 4 km (denoted as $\sigma_{2-4 \, \text{km}}$) varies from 0 to 100% of the aerosol extinction coefficient below 2 km (denoted as $\sigma_{0-2 \, \text{km}}$), and the median value is 50% of $\sigma_{0-2 \, \text{km}}$. In order to estimate the sensitivity of O_4 absorption to $\sigma_{2-4 \, \text{km}}$, we simulated O_4 DSCDs with profiles with the same $\sigma_{0-2 \, \text{km}}$ of $0.04 \, \text{km}^{-1}$ and different $\sigma_{2-4 \, \text{km}}$ varying from 0 to $0.048 \, \text{km}^{-1}$ (i.e., 1.2 times of $\sigma_{0-2 \, \text{km}}$), and the other parameters were fixed as the settings listed in Table 5.3. The results are shown in Figure 5.15

The results indicate that the aerosols above $2\,km$ can affect the O_4 DSCDs by up to $\sim 3\%$, which is similar to the surface albedo. Therefore, we considered the influence from the aerosols above $2\,km$ as a kind of measurement uncertainty, and treated it in the same way as the errors caused by surface albedo, single scattering albedo and phase function uncertainties.

5.6.6   Sensitivity to surface aerosol extinction
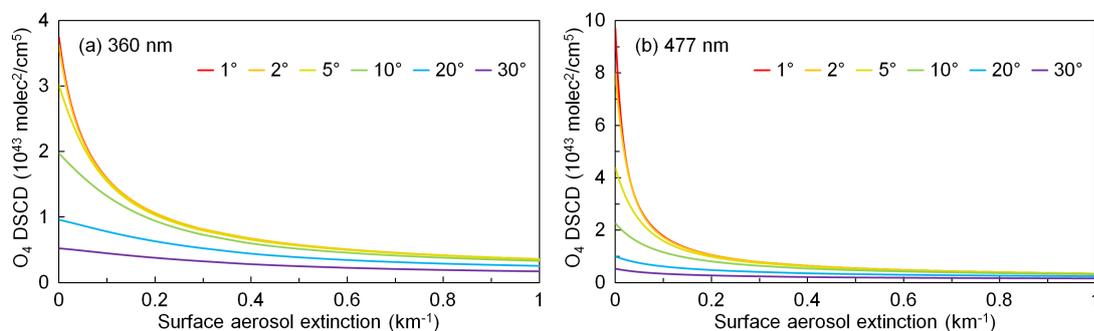
Figure 5.16: Simulated O_4 DSCDs at (a) $360\,nm$ and (b) $477\,nm$ for box-shape profiles with the same box height of $2\,km$ and different surface aerosol extinction coefficients varying from 0 to $1\,km^{-1}$. The other simulation parameters followed the settings listed in Table 5.3. Note that the curves of $1°$ and $2°$ are quite close to each other.

In order to estimate the sensitivity of O_4 DSCD to surface aerosol extinction, we simulated O_4 DSCDs with box-shape profiles with a constant box height of $2\,km$ and different aerosol extinction coefficients vary from 0 to $1\,km^{-1}$. The other parameters were fixed as the settings listed in Table 5.3. The simulated O_4 DSCDs are shown in Figure 5.16.

The results indicate that the O_4 DSCDs at all elevations and both wavelengths decrease monotonically with increasing aerosol extinction, and the sensitivity of O_4 DSCD to surface aerosol extinction also decreases with increasing aerosol extinction. The sensitivity is very low when the surface aerosol extinction coefficient exceeds $0.3\,km^{-1}$. In addition, measurements at lower elevations are much more sensitive.

5.7   Design of the look-up table

In this study, we retrieved aerosol profiles from MAX-DOAS measurements using the LUT method. The basic idea of the LUT method is to replace repetitive time-consuming computation by a pre-calculated database. In this study, we replaced the forward simulation of O_4 DSCDs by a LUT, so that numerous aerosol profiles could be considered in each retrieval with an affordable computational effort.

We considered five input parameters for the look-up function which replaces the forward simulation,

$$\Delta S_{\mathrm{s}} \;=\; f(\boldsymbol{x}, \lambda, \alpha, \theta, \phi), \tag{5.6}$$

where ΔS_{s} represents the simulated O_4 DSCD, $\boldsymbol{x}$ is the aerosol extinction profile, λ is the wavelength, α is the elevation angle, θ is the SZA, and ϕ is the RAA. All the input parameters are well-known in the retrieval.

In order to formulate the pre-calculated database, the five input parameters need to be parametrized as a grid with finite nodes.

5.7.1   Parametrization of the aerosol extinction profile
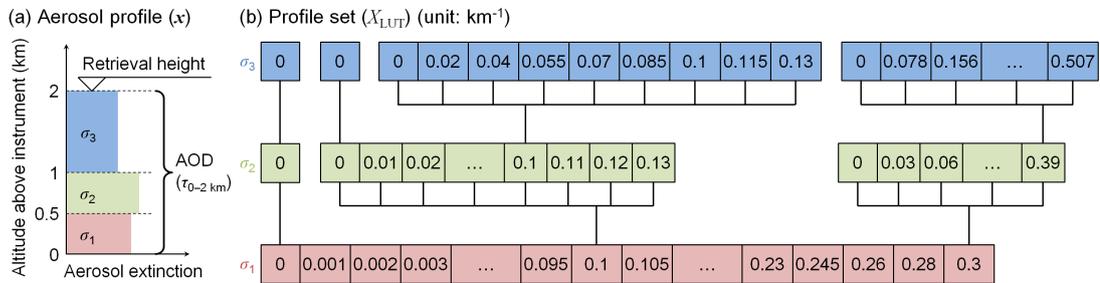
Figure 5.17: Definitions of (a) the parametrized aerosol profile ($\boldsymbol{x}$) and (b) the profile set (X_{LUT}). Note that only some representative nodes are shown in Panel (b).

As discussed in Section 5.6.4, O_4 absorption is insensitive to aerosols above 2 km. Therefore, our retrieval would mainly focus on the aerosols between 0 and 2 km above the MAX-DOAS instrument (i.e., 2,650–4,650 m a.s.l.). In order to limit the complexity of the retrieval, avoid unreasonable results, and make full use of the measurement sensitivity, we parametrized the aerosol extinction profile as aerosol extinction coefficients in three layers. The thicknesses of the lower two

layers were defined as $0.5\,\mathrm{km}$. Due to the lower sensitivity at high altitudes, the thickness of the third layer was set to $1\,\mathrm{km}$. The aerosol profile is denoted as a three-dimensional state vector $\boldsymbol{x}$,

$$\boldsymbol{x} = \begin{pmatrix} \sigma_1 \\ \sigma_2 \\ \sigma_3 \end{pmatrix}, \tag{5.7}$$

where σ_1 is the aerosol extinction coefficient between 0 and $0.5\,\mathrm{km}$ ($2{,}650$–$3{,}150\,\mathrm{m}$ a.s.l.), σ_2 is the aerosol extinction coefficient between 0.5 and $1\,\mathrm{km}$ ($3{,}150$–$3{,}650\,\mathrm{m}$ a.s.l.), and σ_3 is the aerosol extinction coefficient between 1 and $2\,\mathrm{km}$ ($3{,}650$–$4{,}650\,\mathrm{m}$ a.s.l.). The definition of $\boldsymbol{x}$ is illustrated in Figure 5.17 (a).

5.7.2   Definition of the profile set

In order to formulate the LUT, we defined a profile set (denoted as X_{LUT}) which is assumed to include all possible aerosol extinction profiles under cloud-free condition. X_{LUT} is a finite set of $\boldsymbol{x}$, and the variation steps of σ_1, σ_2 and σ_3 were determined according to the sensitivity and accuracy of measurements. X_{LUT} includes only the profiles with reasonable shapes, and the variation range of σ_1, σ_2 and σ_3 covers the actual aerosol load at the UFS. In this way, unreasonable and unrealistic retrieval results can be avoided.

As discussed in Section 5.6.6, the measurement sensitivity decreases with increasing surface aerosol extinction, and the sensitivity is very low when the surface aerosol extinction coefficient exceeds $0.3\,\mathrm{km}^{-1}$. Therefore, σ_1 was defined to vary between 0 and $0.3\,\mathrm{km}^{-1}$. The variation step increases from $0.001\,\mathrm{km}^{-1}$ per step to $0.02\ \mathrm{km}^{-1}$ per step with increasing aerosol extinction, so that the difference of O_4 DSCD per step is similar to the average spectral fitting error ($\sim 2\%$). In total, we defined 65 values for σ_1, see Table 5.4.

As illustrated in Figure 5.17 (b), the values of σ_2 and σ_3 were defined like a tree, which means we defined different values of σ_2 for different σ_1, and the values of σ_3 were also defined depending on σ_2. According to the ceilometer observations at the UFS, strong elevated aerosol layers are unlikely to exist under cloud-free conditions, therefore we allowed only weak elevated layers in designing the profile set. We assume that for reasonable profiles, σ_2 should not exceed σ_1 by more than 30%, and σ_3 should not exceed σ_2 by more than 30%, either. According to the sensitivity, for each value of σ_1 ($\sigma_1 > 0$), we defined 14 possible values

for σ_2 which varies from 0 to $1.3\sigma_1$ with a step size of $0.1\sigma_1$. In case $\sigma_1 = 0$, elevated layers are not considered, then σ_2 and σ_3 can only be 0. Similarly, σ_3 varies between 0 and $1.3\sigma_2$. Due to the lower measurement sensitivity at higher altitude, we defined 9 possible ratios between σ_3 and σ_2 (see Table 5.4). In case $\sigma_2 = 0$, σ_3 can only be 0.

X_{LUT} includes the profiles with all the combinations of σ_1, σ_2/σ_1 and σ_3/σ_2. For each of the 64 nonzero values of σ_1, there are $1 + (13 \times 9) = 118$ corresponding profiles. For $\sigma_1 = 0$, there is only one profile with $\sigma_1 = \sigma_2 = \sigma_3 = 0$. Therefore, the profile set consists of $1 + 64 \times 118 = 7{,}553$ aerosol extinction profiles in total.

5.7.3 Definitions of other dimensions of the look-up table

As already presented above, the five input parameters of the look-up function need to be parametrized as a grid with finite nodes. As discussed in Section 5.7.2, the aerosol extinction profile ($\boldsymbol{x}$) has been parametrized as a profile set which consists of 7,553 possible profiles. For the other four input parameters, we also need to define finite representative nodes.
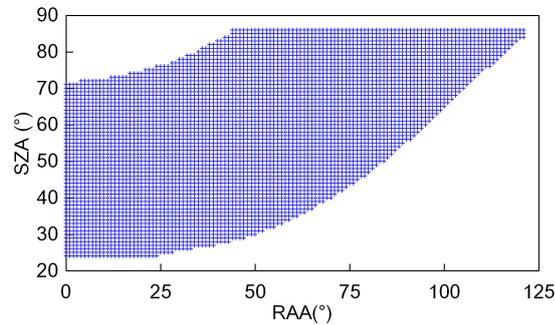
Figure 5.18: The SZA-RAA grid of the LUT.

Since the simulated O_4 DSCDs were to be fitted to the measured ones, only the data at 360 and 477 nm and at the six off-zenith elevation angles of the measurement cycles ($1°$, $2°$, $5°$, $10°$, $20°$, $30°$) were needed and hence included in the LUT. For SZA (θ) and RAA (ϕ), we defined a grid with $1° \times 1°$ resolution. The grid includes 5,005 combinations of SZA and RAA, which can cover all possible solar positions for the daytime measurements at the UFS, see Figure 5.18. When we obtained data from the LUT, as the input SZA and RAA are not integers, the output ΔS_{s} was interpolated from the data of the four adjacent nodes of the SZA-RAA grid. In total, the five input parameters were parametrized as a grid with

Table 5.4: Definition of input parameters of the O_4 DSCD LUT.

Parameter	Symbol	Number of grid points	Grid values
Aerosol extinction coefficient of 0–0.5 km above instrument (km^{-1})	σ_1	65	0, 0.001, 0.002, ..., 0.009, (0.001/step, 10 values) 0.01, 0.0115, 0.013, ..., 0.0265, (0.0015/step, 12 values) 0.028, 0.03, 0.032, ..., 0.038, (0.002/step, 6 values) 0.04, 0.0425, 0.045, 0.0475, (0.0025/step, 4 values) 0.05, 0.053, 0.056, ..., 0.077, (0.003/step, 10 values) 0.08, 0.085, 0.09, ..., 0.115, (0.005/step, 8 values) 0.12, 0.13, 0.14, ..., 0.19, (0.01/step, 8 values) 0.2, 0.215, 0.23, 0.245, (0.015/step, 4 values) 0.26, 0.28, 0.3 (0.02/step, 3 values)
Aerosol extinction coefficient of 0.5–1 km above instrument (km^{-1})	σ_2	14 ($\sigma_1 > 0$) 1 ($\sigma_1 = 0$)	0, 0.1σ_1, 0.2σ_1, ..., 1.3σ_1 (0.1σ_1/step)
Aerosol extinction coefficient of 1–2 km above instrument (km^{-1})	σ_3	9 ($\sigma_2 > 0$) 1 ($\sigma_2 = 0$)	0, 0.2σ_2, 0.4σ_2, 0.55σ_2, 0.7σ_2, 0.85σ_2, σ_2, 1.15σ_2, 1.3σ_2
Wavelength (nm)	λ	2	360, 477
Elevation angle (°)	α	6	1, 2, 5, 10, 20, 30
Solar zenith angle (SZA) (°)	θ	63	24, 25, 26, ..., 86 (1/step)
Relative solar azimuth angle (RAA) (°)	ϕ	122	0, 1, 2, ..., 121 (1/step)

$7,553 \times 2 \times 6 \times 5,005 = 453,633,180$ nodes. Details of the parametrization of the input parameters are summarized in Table 5.4.

As discussed in Section 5.6, besides the input parameters we defined, O$_4$ DSCDs can also be affected by other parameters such as the ground albedo, aerosol optical properties, and others. Since accurate measurements of these parameters are not available and their influence is relatively small, they are considered as uncertainties. In creating the LUT, these parameters were fixed to the median values discussed in Section 5.6. Details of the simulation settings are listed in Table 5.5. O$_4$ DSCDs corresponding to all nodes of the LUT were simulated using LIDORT.

As discussed in Section 5.6.5, the influence from the aerosols above $2\,\mathrm{km}$ was also considered as a kind of uncertainty and treated in a similar way as the other unknown parameters. In the simulations for creating the LUT, the aerosol extinction coefficient between 2 and $4\,\mathrm{km}$ was defined as $0.5\sigma_3$, so that this so-called parameter was fixed to the 'median' value. Note that the aerosol extinction coefficient in this layer is not considered as a part of the retrieved profile and does not play a part in calculating the retrieved AOD.

5.8   O$_4$ DSCD uncertainty estimation

The uncertainties of O$_4$ DSCDs are required in the aerosol profile retrieval. Most of the other MAX-DOAS studies only considered the spectral fitting error in their retrieval. However, the fitting error only contributes to a small part of the total uncertainty. In addition, the total uncertainty is not directly proportional to the spectral fitting error. As the measurement and simulation uncertainties play an important part in our inversion method, we performed a comprehensive error analysis for the MAX-DOAS measurements and radiative transfer simulation of O$_4$ DSCDs. In this study, error from seven major sources were taken into account in estimating the total uncertainty.

5.8.1   Error in measured O$_4$ DSCDs

Two error sources related to measured O$_4$ DSCDs were taken into account in the total uncertainty estimation, which are the DOAS fitting error (ϵ_fit) and the error caused by temperature variation (ϵ_temp).

Table 5.5: Settings of fixed parameters in calculating the O_4 DSCD LUT.

Parameter	Value or definition
Topography	A flat surface at an altitude of 2,650 m a.s.l.
Surface albedo	0.1
Single scattering albedo (SSA)	0.93 (360 nm) / 0.92 (477 nm)
Phase function	The 'median' phase function defined in Section 5.6.3
Climatology	US standard profiles for profile, temperature and trace gas profiles
Aerosol extinction coefficient of 2–4 km above instrument	50% of the aerosol extinction coefficient of 1–2 km above instrument (i.e., $0.5\sigma_3$)
Aerosol extinction coefficient above 4 km from instrument	0

5.8.1.1 DOAS fitting error

ϵ_{fit} is the byproduct of the DSCD calculation, derived from the fitting residual and the absorption cross section of O_4. It is proportional to the RMS of the fitting residual. For low elevations (1°, 2°, 5°), the percentage of ϵ_{fit} comparing to the DSCD typically varies between 1% and 3% at the UV band and between 0.3% and 0.7% at the VIS band, which is rather small compared to other sources of error. However, for the elevation of 30°, as the absolute DSCD values are much smaller, the percentage of ϵ_{fit} can be up to $\sim$25% and $\sim$10% at the UV and VIS bands, respectively.

5.8.1.2 Error caused by temperature variation

As discussed in Section 5.4, O_4 absorption cross section measured at 273 K was used in the DOAS fitting. However, the effective temperature of the MAX-DOAS measurements could be significantly different from 273 K. Previous studies have shown that O_4 absorption has a strong and systematic dependence on temperature (Thalman and Volkamer, 2013; Wagner et al., 2019).
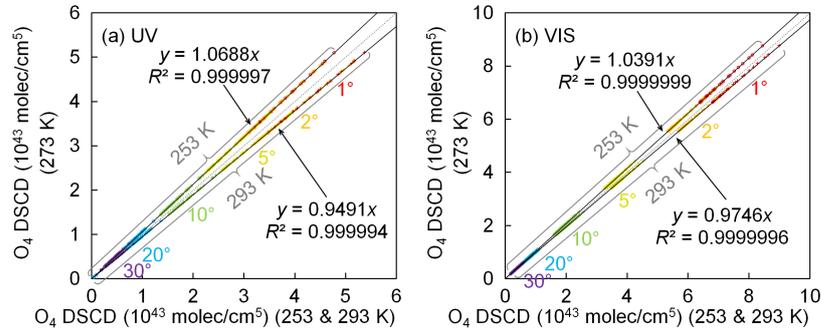
Figure 5.19: Comparison of O_4 DSCDs calculated using cross sections measured at 273 K and the ones calculated using cross sections measured at 253 and 293 K, calculated from all the spectra measured on 07 Dec 2015. Panels (a) and (b) show the data of UV and VIS bands, respectively. The data of 253 K are shown as X markers, while the data of 293 K are shown as circle markers. Data points are plotted in different colors according to their elevation angles.

In order to estimate the error in O_4 DSCDs caused by the variation of temperature, we compared the O_4 DSCDs calculated using the cross sections measured at 273 K to the ones calculated using the cross sections measured at 253 K and 293 K. Figure 5.19 shows the comparison based on the data of an entire day. The

results indicate that O_4 DSCDs calculated using different cross sections are linearly correlated, regardless of the measurement geometry. The linear regression results indicate that when the effective temperature is $293\,K$, O_4 DSCDs calculated using the cross sections measured at $273\,K$ are underestimated by 5.09% and 2.54% for UV and VIS bands, respectively; when the effective temperature is $253\,K$, O_4 DSCDs are overestimated by 6.88% and 3.91% for UV and VIS bands, respectively. Between 253 and $293\,K$, the average variation rate of O_4 DSCD at UV band is $0.3\%/K$. This result is in general agreement with Wagner et al. (2019). They found that with the fitting window of 352–$387\,nm$, O_4 DSCDs retrieved using the cross section at $203\,K$ are 30% smaller than those retrieved using the cross section at $293\,K$, i.e., $0.33\%/K$ on average.

As we assume the error is linear to the temperature difference, based on the fact that the temperature at the measurement site varies between ~258 and $288\,K$ during daytime in most cases, we estimated the ϵ_{temp} of all measurements to be 4.5% and 2.4% of the O_4 DSCDs at UV and VIS band, respectively.

5.8.2   Error in simulated O_4 DSCDs

Five error sources related to simulated O_4 DSCDs were taken into account in estimating the total uncertainty. They are the random error caused by the simplification of the topography definition (ϵ_{topo}), the error caused by surface albedo (ϵ_{SA}), the error caused by single scattering albedo (ϵ_{SSA}), the error caused by phase function (ϵ_{PF}) and the error caused by aerosols above retrieval height ($\epsilon_{2-4\,\text{km}}$).

As discussed in Section 5.5, the random error caused by the simplification of the topography definition (ϵ_{topo}) of each elevation and each wavelength was derived from the standard deviation of the relative errors of the 18 cases simulated using the three-dimensional RTM TRACY-2. Values of ϵ_{topo} are listed in Table 5.2.

For the uncertainties from the other four sources (ϵ_{SA}, ϵ_{SSA}, ϵ_{PF} and $\epsilon_{2-4\,\text{km}}$), as discussed in Section 5.6, they can be estimated by radiative transfer simulations. Since they differ under different observation geometries and different aerosol loads, we determined them using simple LUTs in the retrieval. In order to simplify the error estimation process, we assume that the uncertainties from the four sources are only influenced by the AOD, while the influence from different vertical distribution of aerosols is neglected. In addition, from the O_4 DSCD LUT, we found that O_4 DSCD at $5°$ is almost negatively correlated with AOD, while it is
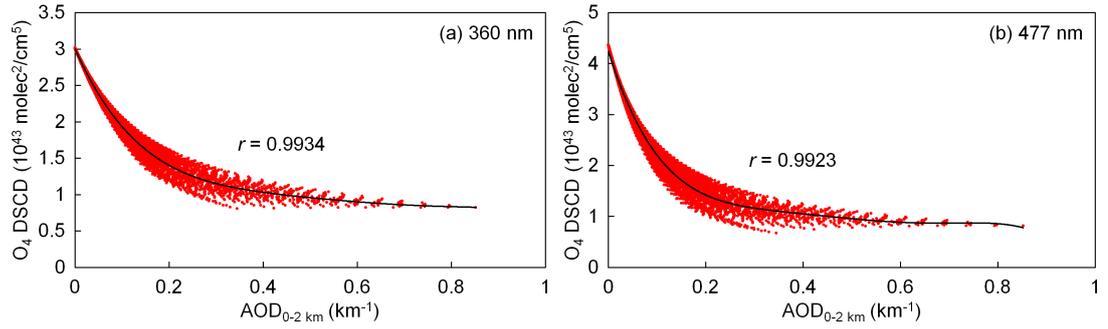
Figure 5.20: Correlation between O$_4$ DSCD at 5° and AOD between 0 and 2 km for all the profiles in X_{LUT} (SZA = RAA = 60°). The r value shown in each chart is the Pearson correlation coefficient of the trend line.

insensitive to the shape of profile (an example is shown in Figure 5.20). Therefore, we used the O$_4$ DSCD measured at 5° as the indicator for estimating the AOD in deriving uncertainty values from the error LUTs.

The error LUTs consist of the values of ϵ_{SA}, ϵ_{SSA}, ϵ_{PF} and $\epsilon_{2-4\,\text{km}}$ for all combinations of SZA and RAA (with 1° × 1° resolution) and 65 profiles of the X_{LUT} with $\sigma_1 = \sigma_2 = \sigma_3$. The calculation of the error LUTs was similar to the sensitivity study. In order to estimate the uncertainty caused by each parameter, O$_4$ DSCDs were simulated under both median and extreme values, while all the other parameters were fixed as the median settings listed in Table 5.5. For each scenario, the relative difference between the two simulations was treated as the uncertainty and stored in the LUT.

As discussed in Section 5.6.1, the uncertainty caused by surface albedo (ϵ_{SA}) was derived from the relative difference of the O$_4$ DSCDs simulated with the surface albedo set to 0.2 (extreme value) and 0.1 (median value).

As discussed in Section 5.6.2, in the estimation of the uncertainty caused by single scattering albedo (ϵ_{SSA}), the extreme value was chosen as 0.997 for both the UV and VIS bands, while the median value was chosen as 0.92 and 0.93 for UV and VIS bands, respectively.

As discussed in Section 5.6.3, from all the phase functions measured by the AERONET station in Hohenpeißenberg during the period of 2013–2014, the phase function with which the simulated O$_4$ DSCDs at all elevations are closest to the median values was chosen as the so-called 'median' phase function. The phase function with which the simulated O$_4$ DSCDs are closest to the rank of 95% (i.e., 2σ) was chosen as the 'extreme' phase function. ϵ_{PF} was derived from the

relative difference between O_4 DSCDs simulated with 'extreme' and 'median' phase functions.

As discussed in Section 5.6.5, the error caused by aerosols above $2\,\mathrm{km}$ ($\epsilon_{2-4\,\mathrm{km}}$) was treated like ϵ_{SA}, ϵ_{SSA} and ϵ_{PF} in the study. The so-called 'median' O_4 DSCDs were simulated with profiles with $\sigma_{2-4\,\mathrm{km}}$ (the aerosol extinction coefficient between 2 and $4\,\mathrm{km}$) equals to $0.5\sigma_3$ (50% of the aerosol extinction coefficient between 1 and $2\,\mathrm{km}$), while the 'extreme' values were simulated with profiles with $\sigma_{2-4\,\mathrm{km}} = \sigma_3$. $\epsilon_{2-4\,\mathrm{km}}$ was derived from the relative difference between the 'extreme' and 'median' results.

5.8.3 Total uncertainty

As the seven kinds of errors mentioned in Sections 5.8.1 and 5.8.2 are independent to each other and we assume they follow the normal distribution, the total uncertainty of each band and each elevation can be determined by the RMS of the seven errors as

$$\epsilon = \sqrt{\epsilon_{\mathrm{fit}}^2 + \epsilon_{\mathrm{temp}}^2 + \epsilon_{\mathrm{topo}}^2 + \epsilon_{\mathrm{SA}}^2 + \epsilon_{\mathrm{SSA}}^2 + \epsilon_{\mathrm{PF}}^2 + \epsilon_{2-4\,\mathrm{km}}^2}. \qquad (5.8)$$
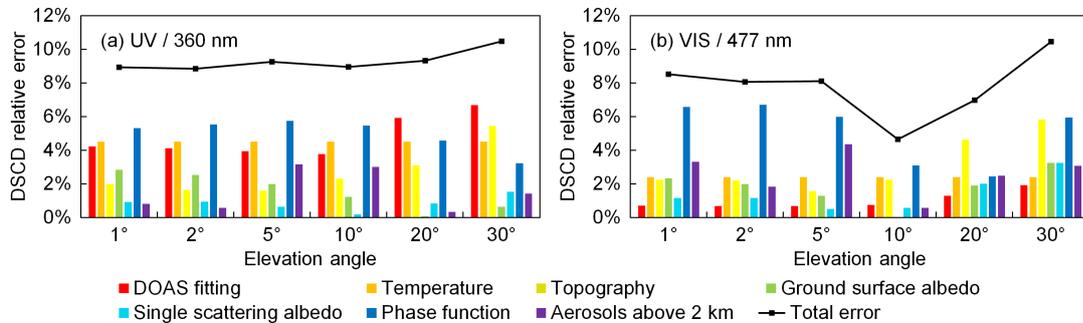
Figure 5.21: Error budgets of (a) UV and (b) VIS bands of the scanning cycle on 05 Jul 2015 at $\sim$16:26 UTC (SZA $\sim$64°, RAA $\sim$97°). Y-axes refer to the relative error of O_4 DSCDs.

Examples of the error budgets of two measurement cycles at both wavelength bands are shown in Figure 5.21 and Figure 5.22. The cycle shown in Figure 5.21 was measured in summer under relatively high aerosol load (AOD at $440\,\mathrm{nm}$ measured by the sun photometer around the noon of that day was $\sim$0.2), while the cycle shown in Figure 5.22 was measured in winter under relatively low aerosol load (AOD at $440\,\mathrm{nm}$ measured by the sun photometer around the noon of that
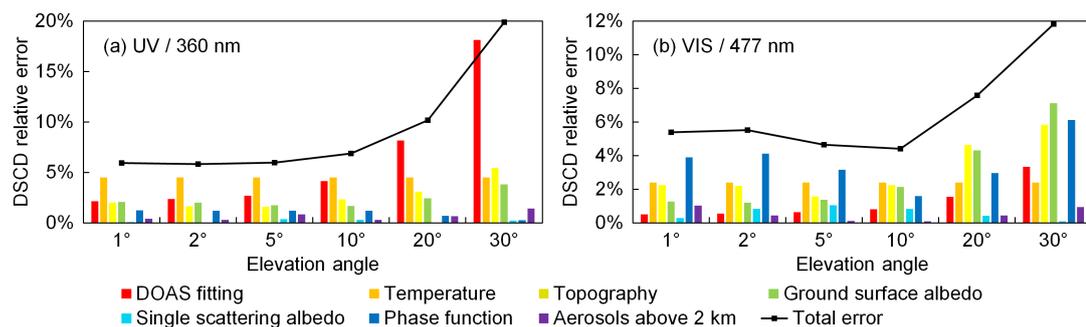
Figure 5.22: Same as Figure 5.21, but for the scanning cycle on 07 Dec 2015 at ~13:55 UTC (SZA ~79°, RAA ~39°).

day was ~0.015). In addition, The former cycle was measured under a smaller SZA comparing to the latter (64° and 79°, respectively), while the RAA was much larger than the latter (97° and 39°, respectively). The results show that contributions from different error sources are quite different in different measurement cycles, at different wavelengths and at different elevation angles.

5.8.4 Other possible error sources

Besides the seven error sources mentioned above, there are still some other sources of error which are difficult to be estimated and hence not included in the error estimation. For example:

a. Error in O$_4$ DSCD scaling factors: in this study, we found that elevation-dependent O$_4$ DSCD scaling factors are needed to bring measurements and modeled results into agreement. We determined the factors based on the statistical analysis of the long-term measurement, see Section 5.10. However, as it is still difficult to estimate the uncertainties of the scaling factors, they are currently not taken into account in calculating the total uncertainties.

b. Error caused by horizontal gradients of the aerosol extinction: besides its direct effect on the measurements, the complex topography might also cause systematic horizontal gradients of the aerosol extinction. For example, polluted air masses from the valleys might be transported to higher altitudes according to the vertical mixing and the prevailing wind direction. Such effects can be especially important for the measurements discussed here because of the rather low AOD. Further quantification of the effects of possible horizontal gradients is beyond the scope of this study, but might be one reason for the observed elevation

dependence of the O_4 DSCD scaling factor.

c. Error caused by the variation of atmospheric profile: the O_4 DSCD LUT was calculated using the US standard climatology data, but the change of atmospheric temperature and pressure can slightly affect the O_4 absorption. However, since it is difficult to estimate the accurate uncertainty and real-time measurements of temperature and pressure profiles were not available, the error caused by the variation of the atmospheric profile was not taken into account in calculating the total uncertainties.

d. Systematic effect of the surface albedo on the measurements at the high-altitude station: due to the dependence of the snow coverage on altitude, the surface albedo close to the instrument is typically higher than at locations far away. Since the measurements at high elevations are usually more sensitive to air masses closer to the instrument, they are probably more strongly affected by snow and ice comparing to the measurements at low elevations. In this study, this effect could not be further quantified, but it might be one reason for the need of different O_4 DSCD scaling factors for different elevations, see Section 5.10.

In order to avoid the underestimation of the measurement uncertainty, we set a relatively relaxed threshold of cost functions for choosing valid profiles, see Section 5.9.

5.9   Aerosol profile inversion method

Aerosol extinction profiles were retrieved from the measured O_4 DSCDs of each scanning cycle. The measurements of the UV and VIS bands were retrieved separately. The measured O_4 DSCDs at the UV and VIS bands were fitted to the O_4 DSCDs simulated at 360 and 477 nm, respectively. In the retrieval, we assume the state of atmosphere is stable during a scanning cycle, and the distribution of aerosols is homogeneous in horizontal direction. For a single scanning cycle, the measured O_4 DSCDs at the wavelength λ are denoted as a measurement vector

$$\boldsymbol{y}_{\mathrm{m}} = \begin{pmatrix} \Delta S_{\lambda,1} \\ \Delta S_{\lambda,2} \\ \vdots \\ \Delta S_{\lambda,M} \end{pmatrix}, \tag{5.9}$$

where M is the number of off-zenith measurements in each scanning cycle, which

is 6 in this study. $\Delta S_{\lambda,1}$, $\Delta S_{\lambda,2}$, ..., $\Delta S_{\lambda,6}$ are the O_4 DSCDs measured at the wavelength band λ and at the viewing elevation angles of $1°$, $2°$, $5°$, $10°$, $20°$, and $30°$, respectively.

The simulated O_4 DSCDs corresponding to each possible aerosol extinction profile in X_{LUT} can be obtained from the LUT. Similar to $\boldsymbol{y}_{\text{m}}$, the simulation vector $\boldsymbol{y}_{\text{s}}$ for each possible profile $\boldsymbol{x}$ is be denoted as

$$\boldsymbol{y}_{\text{s}}(\boldsymbol{x}) = \begin{pmatrix} f(\boldsymbol{x}, \lambda, \alpha_1, \theta_1, \phi_1) \\ f(\boldsymbol{x}, \lambda, \alpha_2, \theta_2, \phi_2) \\ \vdots \\ f(\boldsymbol{x}, \lambda, \alpha_M, \theta_M, \phi_M) \end{pmatrix}, \text{for } \boldsymbol{x} \in X_{\text{LUT}}. \tag{5.10}$$

Aerosol extinction profiles can be derived by fitting the forward simulation to the measured O_4 DSCDs. Typically, the optimal solution can be determined by minimizing the cost function, which was defined as

$$\chi^2(\boldsymbol{x}) = [\boldsymbol{y}_{\text{m}} - \boldsymbol{y}_{\text{s}}(\boldsymbol{x})]^{\text{T}} \cdot \mathbf{S}_\epsilon^{-1} \cdot [\boldsymbol{y}_{\text{m}} - \boldsymbol{y}_{\text{s}}(\boldsymbol{x})], \tag{5.11}$$

where $\mathbf{S}_\epsilon$ is the data error covariance matrix. Assuming the measurement of each viewing elevation is independent, $\mathbf{S}_\epsilon$ is a diagonal matrix and its diagonal elements equal to the square of the total uncertainties of each elevation defined in Eq. (5.8),

$$\mathbf{S}_\epsilon = \begin{bmatrix} \epsilon_1^2 & 0 & \ldots & 0 \\ 0 & \epsilon_2^2 & \ldots & 0 \\ \vdots & \vdots & \ddots & \vdots \\ 0 & 0 & \ldots & \epsilon_M^2 \end{bmatrix}. \tag{5.12}$$

Our cost function definition is similar to the cost functions used in many of the MAX-DOAS studies based on the OEM (e.g., Clémer et al., 2010; Frieß et al., 2016; Wang et al., 2016; Chan et al., 2017), but only includes the item related to measurement error, while the item related to the a priori profile is omitted. This is because the a priori profile is not needed in our retrieval algorithm.

χ^2 indicates the difference between $\boldsymbol{y}_{\text{s}}$ and $\boldsymbol{y}_{\text{m}}$, however, as the retrieval is ill-posed and the SNR of the measurement at the UFS is low, the single profile with the lowest χ^2 is not necessarily the one closest to the true profile. In order to overcome this limitation, we consider all the profiles in X_{LUT} with $\chi^2(\boldsymbol{x}) \leq 1.5M$ (9 in this study) as valid profiles and calculate the weighted mean profile as the

optimal result. A profile with $\chi^2 \leq M$ indicates that the measured and simulated O_4 DSCDs agree within the measurement uncertainties, but in order to avoid underestimation of the measurement uncertainties, we defined the threshold as $1.5M$. The weight of each valid profile in the calculation of the optimal solution is defined based on its cost function:

$$w(\boldsymbol{x}) \,=\, \frac{1/\chi^2(\boldsymbol{x})}{\sum[1/\chi^2(\boldsymbol{x})]}, \text{for } \boldsymbol{x} \,\in\, X_{\text{LUT}} \text{ and } \chi^2(\boldsymbol{x}) \,\leq\, 1.5M. \quad\quad (5.13)$$

The optimal solution is then defined as the weighted mean of all the valid profiles, which can be calculated as

$$\hat{\boldsymbol{x}} \,=\, \sum w(\boldsymbol{x}) \cdot \boldsymbol{x}, \text{for } \boldsymbol{x} \,\in\, X_{\text{LUT}} \text{ and } \chi^2(\boldsymbol{x}) \,\leq\, 1.5M. \quad\quad (5.14)$$
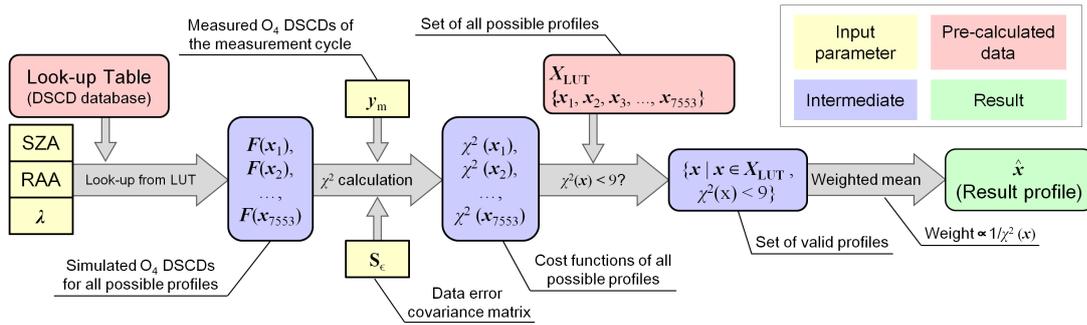
Figure 5.23: Procedure of the aerosol profile inversion method.

The procedure of the aerosol profile inversion method is summarized in Figure 5.23.

5.10 O_4 DSCD correction

Discrepancies between measured and simulated O_4 DSCDs have been found in many other MAX-DOAS studies (Wagner et al., 2009; Clémer et al., 2010; Chan et al., 2015; Wang et al., 2016; Chan et al., 2017; Wagner et al., 2019). The discrepancies were often explained by the systematic errors of the absorption cross section of O_4 as well as the radiative transfer simulation, and a correction is therefore necessary. Some previous studies suggested to multiply a constant scaling factor to the measured O_4 DSCD for all elevations to correct for the
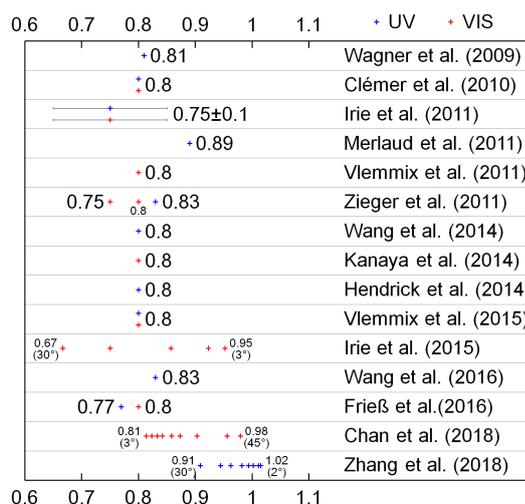
Figure 5.24: O$_4$ DSCD scaling factors suggested by some previous studies.

systematic error. The scaling factor typically varies between 0.75 and 0.9, and the most common value is 0.8 (e.g., Wagner et al., 2009; Clémer et al., 2010; Irie et al., 2011; Merlaud et al., 2011; Vlemmix et al., 2011; Zieger et al., 2011; Wang et al., 2014a; Kanaya et al., 2014; Hendrick et al., 2014; Vlemmix et al., 2015; Wang et al., 2016; Frieß et al., 2016). Some recent studies suggested elevation-dependent scaling factors: Irie et al. (2015) suggested a set of scaling factors for 477 nm which gradually decreases with increasing elevation angle, varying from 0.952 for 3° to 0.667 for 30°; Zhang et al. (2018) suggested a set of scaling factors for 360 nm which also decreases with increasing elevation angle, varying from from 1.02 for 1° to 0.909 for 30°; Chan et al. (2017) derived a set of elevation-dependent scaling factors for 477 nm by comparing modeled and measured (relative) intensities, varying from 0.792 for 1° to 0.957 for 30°. The scaling factors suggested by some previous studies are summarized in Figure 5.24. On the other hand, some other MAX-DOAS studies did not find it necessary to apply any corrections to O$_4$ DSCDs. For example, Frieß et al. (2011) reported that for the MAX-DOAS measurements in an Arctic area, the measured and simulated O$_4$ DSCDs are in good agreement without any correction. Note that the scaling factor mentioned here refers to the ratio between simulated and measured O$_4$ DSCDs, which is opposite to some other studies.

In order to assess whether an O$_4$ DSCD correction is necessary for the MAX-DOAS measurements at the UFS, we compared the measured O$_4$ DSCDs to the simulated ones in the LUT. Assuming our profile set (X_{LUT}) covers all possi-

ble aerosol profiles under cloud-free conditions, we derived the O_4 scaling factor
for each elevation angle and each wavelength based on statistical analysis. The
AODs measured by the sun photometer were used to restrict the range of possible
profiles.
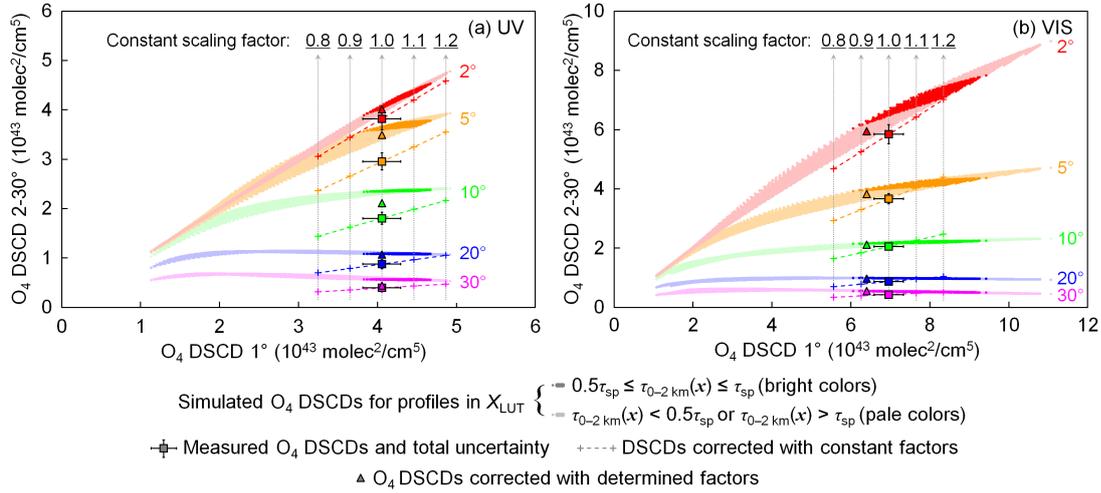
Figure 5.25: Distribution of simulated, measured and corrected O_4 DSCDs of
(a) UV and (b) VIS bands of the scanning cycle on 07 Dec 2015 at ~13:55 UTC
(SZA ~79°, RAA ~39°). The x-axes indicate the O_4 DSCDs measured (or simu-
lated) at the elevation of 1°, while the y-axes represent the O_4 DSCDs measured
(or simulated) at the other five elevations. Different colors indicate measure-
ments at different elevations. The colored dots show the simulated O_4 DSCDs of
all possible profiles in the profile set (X_{LUT}). The data points of the profiles with
AOD between 0 and 2 km ($\tau_{0-2\,\mathrm{km}}(\boldsymbol{x})$) varies between 50% and 100% of the total
AOD measured by the sun photometer (τ_{sp}) are shown in bright colors, while the
dots of the other profiles are shown in pale colors. The square markers represent
measured O_4 DSCDs, and the error bars show the total uncertainties. System-
atic errors caused by the topography simplification are already corrected from the
measured O_4 DSCDs. The plus signs along the dashed lines show the measured
O_4 DSCDs corrected with constant factors of 0.8, 0.9, 1.1 and 1.2. The trian-
gle markers show the measured O_4 DSCDs corrected with the finally determined
scaling factors listed in Table 5.6.

Figure 5.25 shows the scattered plots of measured and simulated O_4 DSCDs
of the scanning cycle measured on 07 December 2015 at ~13:55 UTC. The mea-
surements of both (a) UV and (b) VIS bands are shown. According to the cloud
screening as well as the skycam images, this day was absolutely cloud free. The
total AOD measured by the sun photometer at that time was 0.02 and 0.017 at 360
and 477 nm bands, respectively. In each plot, the x axis indicates the O_4 DSCDs
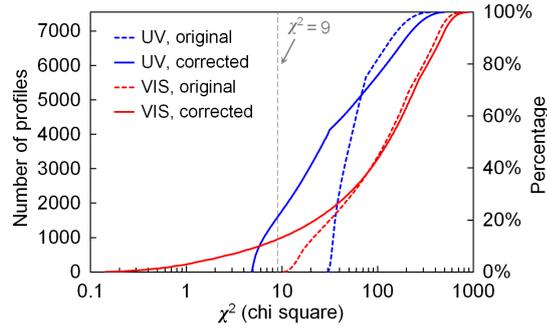
Figure 5.26: Cumulative distribution of the χ^2 of all profiles in X_{LUT} for the scanning cycle at 07 Dec 2015 $\sim$13:55 UTC (SZA $\sim$79°, RAA $\sim$39°). Dashed and solid curves refer to the results before and after the O$_4$ DSCD correction, respectively. Blue and red curves refer to the results of the UV and VIS bands, respectively. Note that the x axis is logarithmically scaled.

measured (or simulated) at the elevation of 1°, while the y axis represents the O$_4$ DSCDs at the other five off-zenith elevations. Different colors indicate measurements at different elevations. The simulated O$_4$ DSCDs ($\boldsymbol{y}_{\mathrm{s}}(\boldsymbol{x})$) of all the possible profiles in X_{LUT} are shown as colored dots. We assume the MAX-DOAS measurement of AOD between 0 and 2 km above instrument (denoted as $\tau_{0-2\,\mathrm{km}}$, $\tau_{0-2\,\mathrm{km}}(\boldsymbol{x}) = 0.5\sigma_1(\boldsymbol{x}) + 0.5\sigma_2(\boldsymbol{x}) + \sigma_3(\boldsymbol{x})$) varies between 50% and 100% of the total AOD measured by the sun photometer (denoted as τ_{sp}) in most cases, and the data points of the profiles fulfilling this assumption are highlighted in the plots. The measured O$_4$ DSCDs (already corrected for the systematic errors caused by the topography simplification) are plotted as square markers with error bars showing the total uncertainties. It is obvious that at most of the elevations, the measured O$_4$ DSCD does not agree with the simulations within the total error. As a result, at both UV and VIS bands, no profiles in X_{LUT} satisfy the selection requirement ($\chi^2 \leq 9$, see dashed curves in Figure 5.26). No profiles matching the measurement is unlikely to happen under such clear sky condition, hence, implies a systematic error and correction of the error is necessary.

In order to determine whether the O$_4$ scaling factor is constant for all the elevations or dependent on the viewing elevation angles, we first assume it is constant and plot the corrected O$_4$ DSCD measurements in Figure 5.25. The plus signs indicate the measured O$_4$ DSCDs corrected with constant scaling factors of 0.8, 0.9, 1.1 and 1.2. Furthermore, the corrected O$_4$ DSCDs should vary along the colored dashed lines simultaneously if any other constant scaling factor is applied

to the measurements. However, the forward simulation of O_4 DSCDs does not overlap with the dashed lines in most of the cases (especially for 5° and 10° of the UV band), indicating that a constant O_4 scaling factor for all viewing elevations could not resolve the systematic error. Therefore, different scaling factors should be applied to different elevations.

In this study, the O_4 DSCD scaling factors for each viewing elevation and each wavelength were determined through the statistical analysis of the long-term observations. We assume the scaling factors mainly depend on the viewing elevation angle, while being less sensitive to other factors such as solar geometry, aerosol load, temperature etc.

5.10.1   Determination of scaling factors of high elevations

Figure 5.25 shows that the simulated O_4 DSCDs at high elevations (e.g. 20° and 30°) vary in very narrow ranges. Based on the assumption that X_{LUT} covers all possible aerosol profiles, the measured O_4 DSCDs should lie within the ranges. Therefore, the scaling factors can be derived by taking the ratio of the simulated and measured values. As the simulated values vary in narrow ranges, the uncertainties of the derived scaling factors should also be low. In order to determine more convincing scaling factors, we derived optimal results from the big data of the long-term measurements. In addition, only the measurements taken under cloud-free and low aerosol load ($\tau_{\mathrm{sp}} \leq 0.03$) conditions were used, so as to avoid accounting data contaminated by clouds in the analysis. Here it should be noted that the measurements with AOD ≤ 0.03 are almost entirely found during winters due to the strong seasonal variation of aerosol load at the UFS.

Subsequently, for the wavelength λ and the ith elevation of each scanning cycle, we found out the simulated O_4 DSCDs corresponding to all the profiles in X_{LUT} fulfilling $0.5\tau_{\mathrm{sp},\lambda} \leq \tau_{0-2\,\mathrm{km}}(\boldsymbol{x}) \leq \tau_{\mathrm{sp},\lambda}$ from the LUT. The simulated O_4 DSCDs can be described as a set,

$$Y_{\lambda,i}^* = \{f(\boldsymbol{x}, \lambda, \alpha_i, \theta_i, \phi_i) \mid \boldsymbol{x} \in X_{\mathrm{LUT}}, 0.5\tau_{\mathrm{sp},\lambda} \leq \tau_{0-2\,\mathrm{km}}(\boldsymbol{x}) \leq \tau_{\mathrm{sp},\lambda}\}. \quad (5.15)$$

Only if $\max(Y_{\lambda,i}^*) \leq 1.1\min(Y_{\lambda,i}^*)$, then the scanning cycle was taken into account. In most cases, measured O_4 DSCDs at high elevations are lower than simulated ones, therefore we calculated the scaling factor from the minimum in

$Y^*_{\lambda,i}$ to avoid over-estimation of the scaling factor. Hence for each of such scanning cycles, the suggested scaling factor is the ratio between the minimum simulated O$_4$ DSCD and the measured O$_4$ DSCD, which can be described as

$$\gamma^*_{\lambda,i} \;=\; \frac{\min(Y^*_{\lambda,i})}{\Delta S_{\lambda,i}}, \tag{5.16}$$

where $\Delta S_{\lambda,i}$ is the measured O$_4$ DSCD (already corrected for the systematic errors caused by the topography). For the elevations of 5°, 10°, 20°, and 30° at UV band and 10°, 20°, and 30° at VIS band, numerous scanning cycles from the long-term measurement fulfill the selection criterion, so there are sufficient samples of $\gamma^*_{\lambda,i}$ for statistical analysis. In order to derive the optimal scaling factors, we analyzed the frequency distribution of $\gamma^*_{\lambda,i}$ for each elevation and each band. We found that for all of the high elevations and both bands, the distribution of $\gamma^*_{\lambda,i}$ follows the normal distribution function with a single sharp peak. Subsequently, the optimal scaling factor of each elevation and each wavelength ($\hat{\gamma}_{\lambda,i}$) was defined as the expected value of $\gamma^*_{\lambda,i}$, which is the mode of $\gamma^*_{\lambda,i}$ derived by Gaussian fit,

$$\hat{\gamma}_{\lambda,i} \;=\; E[\gamma^*_{\lambda,i}]. \tag{5.17}$$
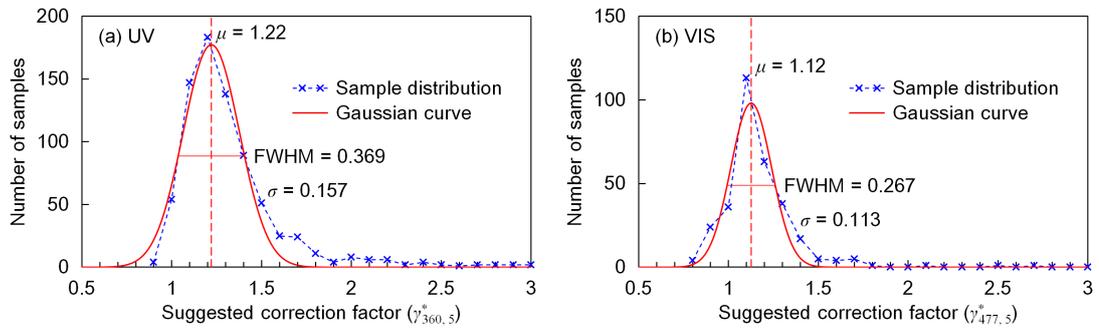
Figure 5.27: Gaussian fits for deriving the O$_4$ DSCD scaling factors of 20° for (a) UV and (b) VIS bands. The frequency distributions are counted for bins of 0.1. In each plot, the vertical dashed line indicates the mode (μ) of suggested scaling factors derived by the Gaussian fit.

Figure 5.27 shows the Gaussian fits for deriving the scaling factors of 20° for UV and VIS bands.
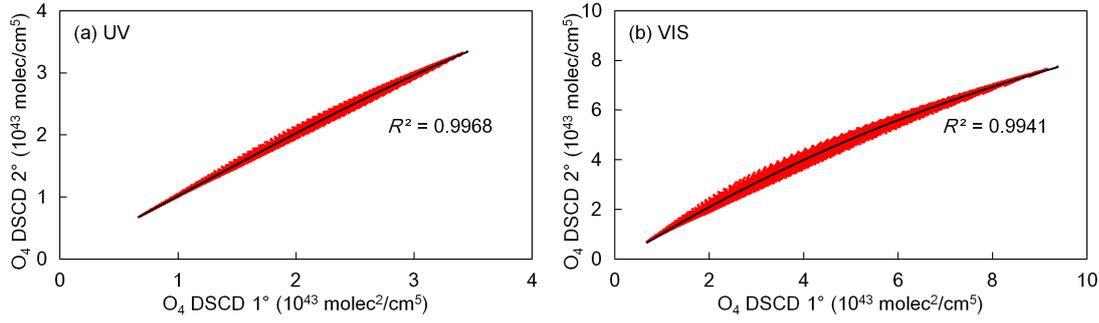
Figure 5.28: Correlation between simulated O_4 DSCDs at $2°$ and $1°$ for all the profiles in X_{LUT} with $0 \leq \tau_{0-2\,\mathrm{km}}(\boldsymbol{x}) \leq 2\tau_{\mathrm{sp}}$, for (a) UV and (b) VIS bands of the measurement cycle on 30 Aug 2015 at $\sim$11:00 UTC.

5.10.2   Determination of scaling factors of low elevations

For the low elevations ($1°$ and $2°$ for UV band and $1°$, $2°$ and $5°$ for VIS band), as O_4 DSCDs vary in wide ranges, it is impossible to determine the scaling factor using the method mentioned above. However, it is found that in many scanning cycles, within the possible profiles in X_{LUT}, the simulated O_4 DSCDs at low elevations are well correlated to those at the neighboring elevation. An example is shown in Figure 5.28. Therefore, once the scaling factor of the higher elevation has been determined, we can derive an expected value of the O_4 DSCD at the lower elevation from the corrected O_4 DSCD at the higher elevation, and the suggested scaling factor can be derived by taking the ratio of the expected and the measured values.

For the wavelength λ and for each scanning cycle, a subset of X_{LUT} is defined as

$$X^{\dagger} = \{\boldsymbol{x} \mid \boldsymbol{x} \in X_{\mathrm{LUT}}, 0 \leq \tau_{0-2\,\mathrm{km}}(\boldsymbol{x}) \leq 2\tau_{\mathrm{sp},\lambda}\}, \qquad (5.18)$$

and the elements of $X^{\dagger}$ are denoted as $\boldsymbol{x}_j^{\dagger}$. The corresponding simulated O_4 DSCDs at the ith elevation are denoted as

$$\Delta S_{i,j}^{\dagger} = f(\boldsymbol{x}_j^{\dagger}, \lambda, \alpha_i, \theta_i, \phi_i), \text{for } \boldsymbol{x}_j^{\dagger} \in X^{\dagger}. \qquad (5.19)$$

For all the profiles in $X^{\dagger}$, a 3rd order polynomial regression was applied between $\Delta S_{i,j}^{\dagger}$ and $\Delta S_{i+1,j}^{\dagger}$. The regression function is denoted as g. Only if the correlation coefficient $R^2 \geq 0.98$, this scanning cycle was taken into account. As the scaling factor of the $(i+1)^{\mathrm{th}}$ elevation ($\hat{\gamma}_{\lambda,i+1}$) has already been determined, the expected

value of the O$_4$ DSCD at the ith elevation can be derived from the corrected measured value at the $(i+1)^{\text{th}}$ elevation by the regression function:

$$E[\Delta S_{\lambda,i}] \ = \ g(\Delta S_{\lambda,i+1} \cdot \hat{\gamma}_{\lambda,i+1}), \qquad (5.20)$$

and the scaling factor suggested by this scanning cycle is

$$\gamma^{\dagger}_{\lambda,i} \ = \ \frac{E[\Delta S_{\lambda,i}]}{\Delta S_{\lambda,i}}. \qquad (5.21)$$

Like the high elevations, we found that for all the low elevations and the both bands, the frequency distribution of $\gamma^{\dagger}_{\lambda,i}$ derived from the long-term measurements also follows the normal distribution, therefore the optimal scaling factor of each elevation and each wavelength was defined as the expected value of $\gamma^{\dagger}_{\lambda,i}$ derived by fitting the frequency distribution to a Gaussian function,

$$\hat{\gamma}_{\lambda,i} \ = \ E[\gamma^{\dagger}_{\lambda,i}]. \qquad (5.22)$$

Once $\hat{\gamma}_{\lambda,i}$ has been determined, the scaling factor of the $(i-1)^{\text{th}}$ (lower) elevation can be derived in the same way. The scaling factors of 1° and 2° at UV band and 1°, 2°, 5° at VIS band were determined using this method.

5.10.3 Summary

Table 5.6: The finally determined O$_4$ DSCD scaling factors.

Elevation angle	Factors for corrected DSCDs[a]		Factors for original DSCDs	
	UV (360 nm)	VIS (477 nm)	UV (360 nm)	VIS (477 nm)
1°	1.00	0.92	0.97	0.90
2°	1.05	1.02	1.01	1.00
5°	1.18	1.04	1.14	1.02
10°	1.17	1.03	1.12	0.99
20°	1.22	1.12	1.16	1.08
30°	1.12	1.27	1.06	1.22

[a] Means the O$_4$ DSCDs which are already corrected for the systematic errors caused by the topography simplification.

The O$_4$ DSCD scaling factors determined by us are listed in Table 5.6. In Figure 5.25, the corrected O$_4$ DSCDs are indicated as triangles. The scaling factors show that except for the elevation of 1°, the simulated O$_4$ DSCDs are overestimated comparing to the measured ones. It should be noted that the de-

termination of the scaling factors is based on the measured O_4 DSCDs which are already corrected for the systematic errors caused by the topography simplification (discussed in 5.5). Comparing to the original measurements, the results still indicate that the simulated O_4 DSCDs at high elevations are overestimated. This result is opposite to the results of most of the other studies. At the moment we have no clear explanation for this finding, it might be related to the specific properties of the high-altitude station, e.g. the highly structured topography, horizontal gradients of the aerosol extinction, and the systematic dependence of the surface albedo on altitude.

Figure 5.26 shows the cumulative distribution of χ^2 of all the profiles in X_{LUT} for the scanning cycle shown in Figure 5.25. The distributions of χ^2 before and after the DSCD correction are shown as dashed and solid curves, respectively. The results indicate that for both UV (blue curves) and VIS (red curves) bands, the χ^2 of most profiles in X_{LUT} are significantly lower after the correction. As a result, a number of profiles can fulfill the selection criterion ($\chi^2 \leq 9$) after the correction. Note that the AODs measured by MAX-DOAS are still expected to be lower than the sun photometer results due to the fact that the MAX-DOAS only reports the AOD below $2\,\text{km}$ while the sun photometer covers the entire atmosphere.

5.11 Results and discussions

Our retrieval algorithm was applied to the long-term measurement data of the UFS MAX-DOAS from February 2012 to February 2013 and from July 2013 to February 2016. The results were also compared to sun photometer measurements. This section presents the results as well as their discussions.

5.11.1 Dependency of retrieval result on the threshold of cost function

As presented in Section 5.9, we consider all the profiles with $\chi^2 \leq 9$ as valid profiles, and the retrieved profile is defined as the weighted mean of all the valid profiles. In this section, we investigate the dependency of the retrieval result on the threshold of χ^2 by comparing the results calculated with different χ^2 thresholds. Taking the two measurement cycles mentioned in Figure 5.21 and Figure 5.22 for example, Figure 5.29 (05 July 2015 at ~16:26 UTC) and Figure 5.30 (07 Decem-
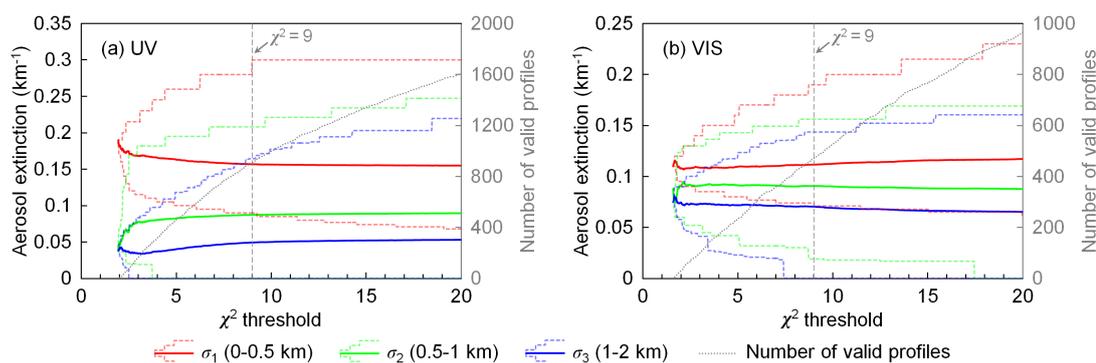
Figure 5.29: Weighted mean profiles, variation ranges of valid profiles and number of valid profiles corresponding to different χ^2 thresholds, results of (a) UV and (b) VIS bands of the scanning cycle on 05 Jul 2015 at $\sim$16:26 UTC (SZA $\sim$64°, RAA $\sim$97°). The weighted mean profiles are shown as solid curves which indicate the aerosol extinction coefficients in the three layers (σ_1, σ_2, and σ_3). The variation ranges of valid profiles are shown as dashed curves which indicate the variation ranges of σ_1, σ_2, and σ_3. The gray dotted curves indicate the number of valid profiles corresponding to different thresholds of χ^2.
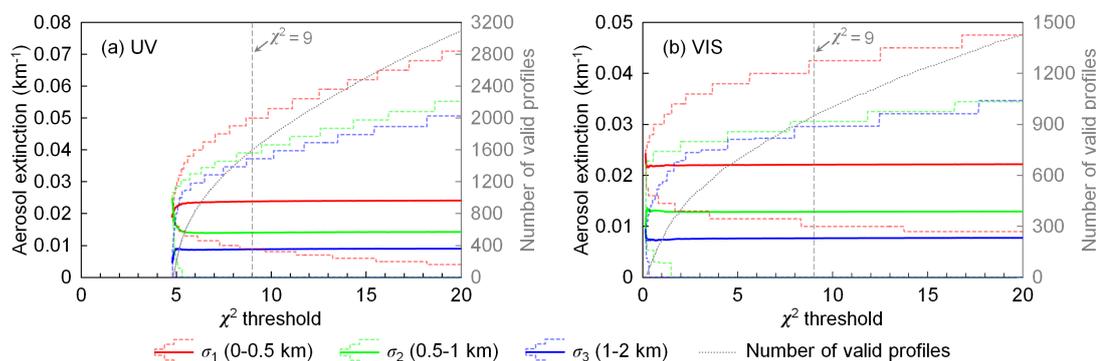
Figure 5.30: Same as Figure 5.29, but for the scanning cycle on 07 Dec 2015 at $\sim$13:55 UTC (SZA $\sim$79°, RAA $\sim$39°).

ber 2015 at $\sim$13:55 UTC) show the weighted mean profiles, the variation range of valid profiles, and the number of valid profiles corresponding to different χ^2 thresholds. The profiles are shown as colored curves which indicate the aerosol extinction coefficients in the three layers (i.e., σ_1, σ_2, and σ_3).

The results of both scanning cycles show that the retrieved profiles are insensitive to the threshold of χ^2 when there are a sufficient number of valid profiles (number of profiles exceeds $\sim$800 and $\sim$400 for UV and VIS bands, respectively; see the gray curves in Figure 5.29 and Figure 5.30). This is because the profiles

with larger χ^2 have lower weight (w). In addition, when the threshold value is increased, more profiles with both higher and lower aerosol extinction coefficients are taken into account. As a result, the variation range of valid profiles becomes larger but the weighted mean remains similar. The results show that the retrieval with a χ^2 threshold of 9 is stable; therefore, it is used in the study.

5.11.2   Estimation of the uncertainties of retrieved profiles
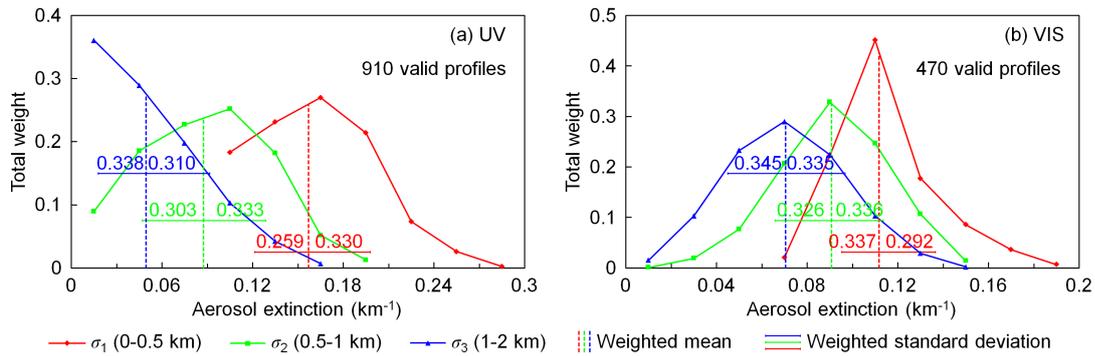
Figure 5.31: Weight distributions of valid profiles of (a) UV and (b) VIS bands, results of the scanning cycle on 05 Jul 2015 at ~16:26 UTC (SZA ~64°, RAA ~97°). The weight distributions of the aerosol extinction coefficients of the three layers (σ_1, σ_2 and σ_3) are shown as solid curves with different colors. The vertical dashed lines indicate the weighted mean aerosol extinction coefficient of the three layers ($\sigma_1(\hat{\boldsymbol{x}})$, $\sigma_2(\hat{\boldsymbol{x}})$ and $\sigma_3(\hat{\boldsymbol{x}})$). The error bars indicate the weighted standard deviation calculated with Eq. (5.23) and (5.24). The numbers on the error bars refer to the total weight (w) of the profiles covered by each error bar.
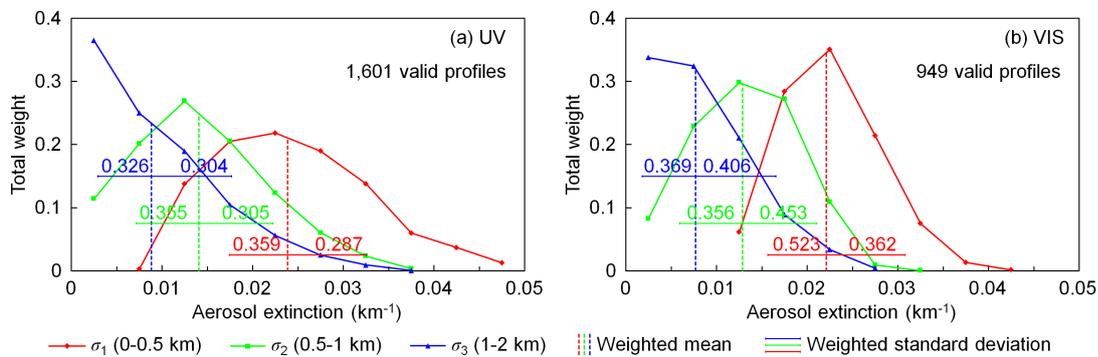
Figure 5.32: Same as Figure 5.31, but for the scanning cycle on 07 Dec 2015 at ~13:55 UTC (SZA ~79°, RAA ~39°).

Still taking the two measurement cycles mentioned in Section 5.11.1 as examples, we analyze the weight distribution of valid profiles, see Figure 5.31 and Figure 5.32. The distributions of aerosol extinction coefficients in the three altitude layers (σ_1, σ_2, and σ_3) are shown as solid curves. For each layer, aerosol extinction coefficients of all valid profiles were grouped, and the y axis refers to the total weight of each group. In each chart, the three vertical dashed lines indicate the weighted mean aerosol extinction coefficient of each layer (i.e., σ_1, σ_2, and σ_3 of $\hat{\boldsymbol{x}}$). The results show that the distributions of σ_1, σ_2 and σ_3 are all asymmetric for both the UV and VIS bands. In particular for the layer of 1–2 km (σ_3) at UV band, the weight decreases monotonically with increasing aerosol extinction in both of the two cycles. Taking the cycle shown in Figure 5.32 (07 December 2015 at ~13:55 UTC) as an example, there are altogether 205 (12.8%) and 120 (12.6%) valid profiles with $\sigma_3 = 0$ at UV and VIS bands, respectively. These profiles contribute total weights of 0.122 and 0.101 for the UV and VIS retrievals, respectively.

In order to estimate the uncertainty of $\hat{\boldsymbol{x}}$, we calculated the weighted standard deviations of σ_1, σ_2 and σ_3 of all valid profiles. Due to the asymmetric distribution, the weighted standard deviations were calculated separately for the left (negative) and right (positive) sides. For the lth ($l = 1$, 2, or 3) layer, denote the aerosol extinction coefficient of each valid profile as $\sigma_l(\boldsymbol{x})$, then the weighted standard deviation of the left side was calculated from all the valid profiles with $\sigma_l(\boldsymbol{x}) < \sigma_l(\hat{\boldsymbol{x}})$,

$$SD_l^- = \sqrt{\frac{\sum w(\boldsymbol{x}) \cdot [\sigma_l(\hat{\boldsymbol{x}}) - \sigma_l(\boldsymbol{x})]^2}{\sum w(\boldsymbol{x})}}, \qquad (5.23)$$

for $\boldsymbol{x} \in X_{\text{LUT}}$ and $\chi^2(\boldsymbol{x}) \le 1.5M$ and $\sigma_l(\boldsymbol{x}) < \sigma_l(\hat{\boldsymbol{x}})$,

and the weighted standard deviation of the right side was calculated from all the valid profiles with $\sigma_l(\boldsymbol{x}) > \sigma_l(\hat{\boldsymbol{x}})$,

$$SD_l^+ = \sqrt{\frac{\sum w(\boldsymbol{x}) \cdot [\sigma_l(\boldsymbol{x}) - \sigma_l(\hat{\boldsymbol{x}})]^2}{\sum w(\boldsymbol{x})}}, \qquad (5.24)$$

for $\boldsymbol{x} \in X_{\text{LUT}}$ and $\chi^2(\boldsymbol{x}) \le 1.5M$ and $\sigma_l(\boldsymbol{x}) > \sigma_l(\hat{\boldsymbol{x}})$.

The uncertainties of $\hat{\boldsymbol{x}}$ are indicated as error bars in Figure 5.31 and Figure 5.32. For each layer, the total weight of the profiles covered by the error bar is labeled in the charts. At the UV band, the total weight of the valid profiles

covered by the uncertainties is 59–66%, which is close to the standard normal distribution. However, the percentage can be up to 90% at the VIS band. This is because the SNR of the measurement at the VIS band is higher. Therefore the retrieval of VIS band has higher selectivity, and the weight is more concentrated to the mean value.

5.11.3   Retrieval of synthetic measurement data
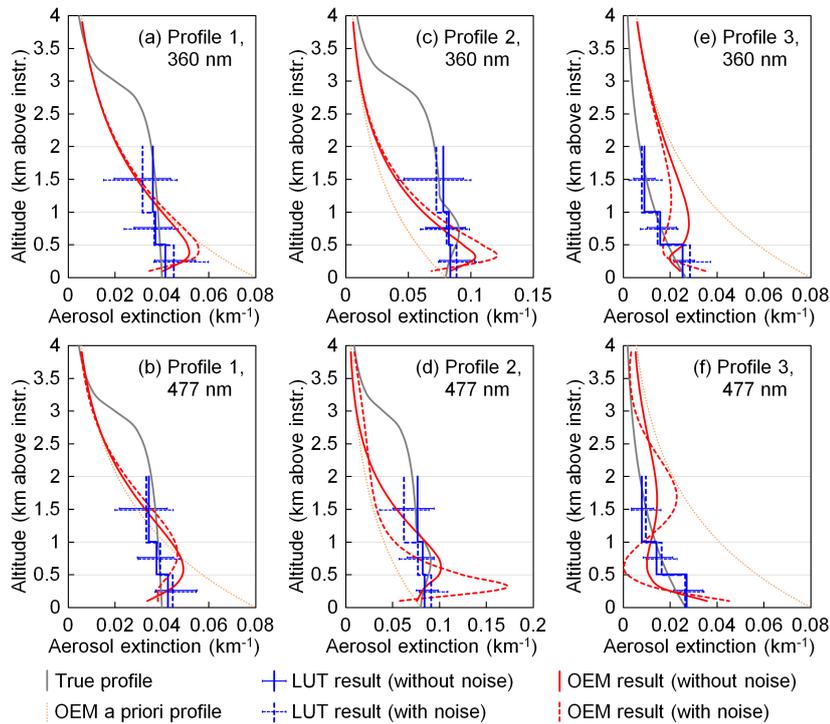
Figure 5.33: Retrieval results of three sets of synthetic data at (a, c, and e) 360 nm and (b, d, and f) 477 nm. The gray curves show the true profiles, with which the synthetic O_4 DSCDs were simulated. The blue and red curves represent the profiles retrieved using our algorithm and BePRO, respectively. The solid blue and red curves represent the profiles retrieved from the original synthetic data, and the dashed curves represent the profiles retrieved from the synthetic data with random noised added. The error bars of the blue curves indicate the uncertainties calculated by Eq. (5.23) and (5.24). The dotted orange curve in each chart is the a priori profile used in the retrievals using BePRO.

In order to test the effectiveness of our retrieval algorithm, we generated some synthetic measurement data and then retrieved using our algorithm. Figure 5.33 shows the results of three representative synthetic profiles at 360 and 477 nm. In

each chart, the true profile is shown as the gray curve. Profile 1 is a tangent curve
with aerosols distributed between 0 and 6 km above instrument. The aerosol ex-
tinction decreases with increasing altitude, which is $0.04 \, \mathrm{km}^{-1}$ at surface level,
$\sim 89\%$ at 2 km, and 50% at 3 km. The total AOD is 0.12, of which $\sim 92\%$ is
contributed from the altitude below 3 km. Profile 2 has a similar shape as Profile
1, but the aerosol extinction between 0.5 and 1 km above instrument has been
enhanced. The aerosol extinction peaks at 0.75 km, and the average aerosol ex-
tinction coefficient between 0.5 and 1 km is larger than the bottom layer by $\sim 10\%$.
In addition, the aerosol extinction coefficients at other altitudes are increased by
a factor of 2 comparing to Profile 1. Profile 3 is an exponential profile. The total
AOD is 0.04, the SH is 1.5 km, and the surface aerosol extinction coefficient is
$0.0267 \, \mathrm{km}^{-1}$.

We first simulated O_4 DSCDs at 360 and 477 nm and at the elevations of 1°,
2°, 5°, 10°, 20° and 30° with each profile. The solar position was set as $\mathrm{SZA} = 60°$
and $\mathrm{RAA} = 60°$, and the other parameters followed the settings used in calculating
the LUT listed in Table 5.5 (excluding the aerosol extinction coefficients above
2 km). In order to test the stability of the retrieval, we also generated a set of
noisy data for each profile and each wavelength by adding random noise to the
simulated O_4 DSCDs. We assume the measurement noise at all the elevations is
at the same level and follows the normal distribution with a standard deviation
of 2% of the DSCD at the lowest elevation. This noise level is realistic for the
measurements at the UFS.

Aerosol profiles were then retrieved from both the original and noisy synthetic
data using our algorithm. In the error estimation, the DOAS fitting error (ϵ_{fit})
was defined as the average values of the UFS measurements, while the other six
kinds of errors followed the common settings presented in Section 5.8. O_4 DSCD
correction was not applied. The solid and dashed blue curves in Figure 5.33 show
the profiles retrieved from the original and noisy data, respectively, and the error
bars indicate the uncertainties calculated by Eq. (5.23) and (5.24). The results
show that for Profile 1 and Profile 3, our retrieval algorithm can well reproduce
the true profiles from not only the original data but also the noisy data. For
Profile 2, the retrieved profile cannot reproduce the elevated layer, but the error
bar covers the aerosol extinction of the true profile. This is because the retrieval is
ill-posed, which means the limited input information does not only correspond to
one or more profiles with elevated layers; instead, many other profiles without the
elevated layer can also fit the input information. Adding noise to the synthetic

data can affect the retrieved aerosol extinction coefficients, however the influence is small in most cases. In addition, the noise can amplify the uncertainty of retrieved profile. The results indicate that our LUT-based retrieval is robust.

As in Section 5.2.3, we also tried to retrieve aerosol profiles from the synthetic data using the bePRO profiling tool. In the retrieval of all the 12 cases (three profiles, with and without noise, 360 and 477 nm), the a priori profile was defined as an exponential profile with AOD = 0.12 and SH = 1.5 km, shown as the dotted orange curve in each panel of Figure 5.33. The vertical grid was defined as 20 layers of 200 m thickness each. The definition of the uncertainty covariance matrix of a priori (S_a) is similar to Section 5.2.3. For Profiles 1 and 2, the scaling factor β was defined as 0.2 and the correlation length γ was defined as 0.05 km. For Profile 3, as the difference between the true and a priori profiles is quite large, we set $\beta = 0.4$ and $\gamma = 0.1$ km, so that the constrain from the a priori profile is weaker. The measurement uncertainty covariance matrix (S_ϵ) was also defined as in most of the other MAX-DOAS studies that S_ϵ is a diagonal matrix with variances equal to the square of the DOAS fitting error (ϵ_{fit}^2). We defined ϵ_{fit} the same as in the LUT-based retrieval, but the other six error sources were not included. The retrieval parameters related to the radiative transfer simulation followed the settings of our LUT-based retrieval.

The results retrieved from the data with and without noise are shown in Figure 5.33 as solid and dashed red curves, respectively. In all of the 12 retrieval cases, the O_4 DSCDs simulated with the retrieved profiles are well correlated to the input values (the relative RMS error varies between 0.7% and 4.7%). However, as the retrieval is ill-posed, the retrieved profiles cannot reproduce the true profile well. Especially at high altitudes (above 1 km), the retrieved profiles are mostly dominated by the a priori profile. In addition, the OEM-based retrieval is sensitive to measurement noise, which can be seen from the large variations in the profile shape and aerosol extinction. The results indicate that our LUT-based algorithm is much more suitable for the measurements at the UFS.

5.11.4   Comparison to sun photometer measurements

Figure 5.34 shows the comparison of the AODs measured by MAX-DOAS and sun photometer during the entire study period. The seasonally averaged AODs measured by both instruments are listed in Table 5.7. As the AODs measured by the MAX-DOAS refer to the AODs between 0 and 2 km while the AODs measured
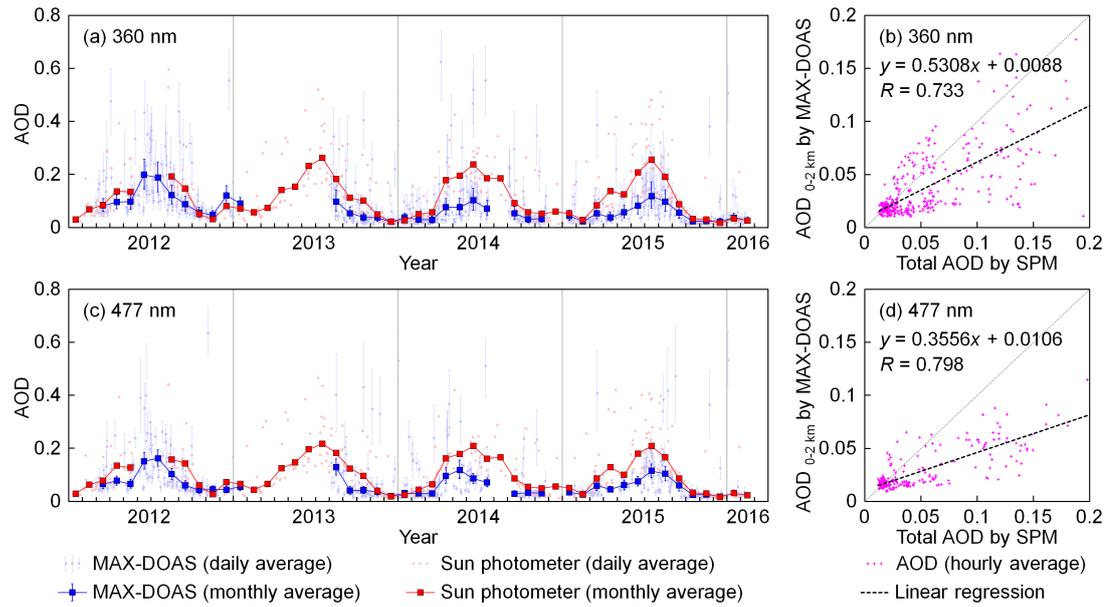
Figure 5.34: Comparison of AODs at (a and b) 360 nm and (c and d) 477 nm measured by the MAX-DOAS and sun photometer at the UFS. The charts on the left side (a and c) show the daily and monthly averaged time series, whereas the scatter plots on the right side (b and d) show the hourly averaged results. The AODs measured by MAX-DOAS refer to the vertical range between 0 and 2 km above the instrument (i.e., $\tau_{0-2\,\text{km}}(\hat{\boldsymbol{x}}) = 0.5\sigma_1(\hat{\boldsymbol{x}}) + 0.5\sigma_2(\hat{\boldsymbol{x}}) + \sigma_3(\hat{\boldsymbol{x}})$). The measurements were available during daytime with $\text{SZA} < 85°$ and cloud-free conditions. The AODs measured by the sun photometer refer to the total AODs, and only the measurements during 10:00–14:00 UTC were used due to their accuracy. The daily and monthly averaged results were calculated from all available hourly averaged AODs. The error bars of the MAX-DOAS data refer to the averages of the uncertainties calculated by Eq. (5.23) and (5.24). A few data points are outside the scatter plots.

by the sun photometer refer to the total AODs, the sun photometer results are expected to be larger. Despite the difference, the time series (Panels (a) and (c) of Figure 5.34) show that the AODs measured by both instruments have a similar seasonal variation with the highest AOD in summer and the lowest in winter. The monthly averaged data show that the difference between the AODs measured by MAX-DOAS and sun photometer is much larger in summer, this coincides with the ceilometer profiles shown in Figure 3.15 which indicate much higher aerosol extinction coefficients above 2 km (4,650 m a.s.l.) in summer.

The correlation between hourly averaged AODs measured by MAX-DOAS and sun photometer is shown in Figure 5.34 (b, d). AODs show a general agree-

Table 5.7: Seasonal average AODs measured by the MAX-DOAS and sun photometer at the UFS. The AODs measured by MAX-DOAS refer to the AODs between 0 and 2 km above instrument (i.e., 2,650–4,650 m a.s.l.), and the meausrements were available during the daytime with SZA $< 85°$ and no cloud; the AODs meausred by sun photometer refer to the total AOD, and the measurements were only available during 10:00–14:00 UTC. The results listed in the table were calculated from all available hourly averaged AODs.

Season	AOD (0–2 km) measured by MAX-DOAS		Total AOD measured by sun photometer	
	360 nm	477 nm	360 nm	477 nm
Spring (MAM)	0.064	0.065	0.106	0.101
Summer (JJA)	0.121	0.114	0.214	0.184
Autumn (SON)	0.048	0.040	0.070	0.068
Winter (DJF)	0.028	0.024	0.037	0.033

ment at the UV and the VIS bands with correlation coefficients of $R = 0.733$ and 0.798, respectively. However, AODs from MAX-DOAS are lower, consequently the slopes of the regression lines are 0.5308 and 0.3556 for UV and VIS bands, respectively. This is within expectation due to the different definitions of AODs. It is in particular true in cases of large AODs due to very strong convection of polluted air masses from the valley and/or the presence of Saharan dust layers. Then, particles are often transported beyond the range of the MAX-DOAS measurements and the disagreement is largest. This feature might be strengthened by the decreased sensitivity of the MAX-DOAS measurements at higher altitudes, so that the upper part of an aerosol layer is missed. In addition, a few data points lie above the 1:1 reference lines. This might be explained by the inhomogeneous distribution of aerosols in horizontal direction, and the light paths of the MAX-DOAS and the sun photometer are different. MAX-DOAS measures scattered sunlight while sun photometer derives the AOD from direct sun measurements. Therefore, when the aerosol load along the light path of MAX-DOAS is higher than that of the direct sun measurement, the AOD measured by the MAX-DOAS may exceed the one measured by the sun photometer. For most of these points, the difference between the results of the two instruments is within their uncertainty range, and the disagreement is probably due to the measurement and retrieval errors.
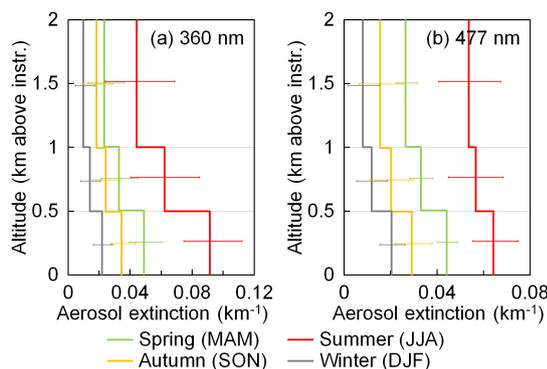
Figure 5.35: Seasonal average aerosol extinction profiles at (a) 360 and (b) 477 nm derived from the long-term measurement results of the MAX-DOAS at the UFS. The error bars represent the average uncertainties calculated by Eq. (5.23) and (5.24).

5.11.5 Temporal variation of aerosol characteristics

The seasonally averaged aerosol extinction profiles derived from the long-term measurements of the MAX-DOAS at the UFS are shown in Figure 5.35. The results indicate that the aerosol load at the UFS is highest in summer and lowest in winter, which coincides with the ceilometer results shown in Figure 3.15. The seasonal pattern can be explained by the higher biogenic emissions from vegetation in summer. Moreover, the mixing layer is higher in summer, thus anthropogenic aerosols are more likely dispersed to upper altitudes. The shape of the profiles also agree with the ceilometer results that the averaged aerosol extinction decreases with increasing altitude in all seasons — taking into account the coarse vertical resolution of the MAX-DOAS. In addition, Figure 5.35 shows a larger vertical gradient at 360 nm in summer. This might be explained by the lower sensitivity of the UV measurement for high altitudes due to the more decreased visibility at shorter wavelengths.

We compared the seasonally averaged aerosol extinction coefficients at 360 and 477 nm in the bottom layer (0–0.5 km above the instrument, σ_1), see Figure 5.36. The averaged aerosol extinction coefficients are shown as bar charts. The ratios between the aerosol extinction coefficients at 360 and 477 nm are indicated by the gray curve. The results show that the aerosol extinction coefficient ratio between 360 and 477 nm is significantly higher in summer than in the other seasons.

The Ångström exponents (AEs) can be calculated from the ratios. The results are listed in Table 5.8. The seasonally averaged AEs of 380–500 nm from
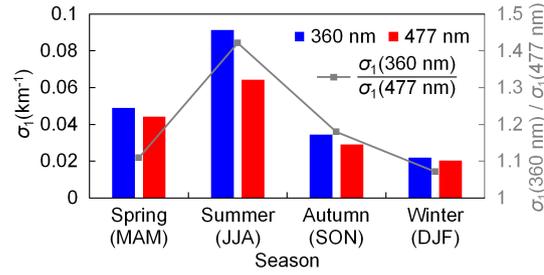
Figure 5.36: Comparison of seasonal average aerosol extinction coefficients at 360 and 477 nm in the bottom layer (0–0.5 km above instrument, σ_1). The colored bars show the average aerosol extinction coefficients of the four seasons (equal to the bottom values shown in Figure 5.35). The gray square markers indicate the ratios between the aerosol extinction coefficients at 360 and 477 nm.

Table 5.8: Seasonal average Ångström exponents (AEs) obtained from MAX-DOAS near-surface measurements (0–0.5 km above instrument) and from AERONET measurements at Hohenpeißenberg. The results of MAX-DOAS were calculated from the ratios between the seasonal average aerosol extinction coefficients at 360 and 477 nm (i.e., the ratios shown in Figure 5.36). The results of AERONET are the seasonally averaged values of AEs (380–500 nm) at Hohenpeißenberg from Apr 2013 to Feb 2016.

Season	AE from UFS MAX-DOAS	AE from AERONET at Hohenpeißenberg
Spring (MAM)	0.37	1.26
Summer (JJA)	1.25	1.38
Autumn (SON)	0.59	1.05
Winter (DJF)	0.24	0.47

the AERONET measurements at Hohenpeißenberg from April 2013 to February 2016 are also listed for comparison. The result shows that both the UFS and Hohenpeißenberg measured the highest AE in summer and the lowest in winter. The AE at the UFS is in general lower than that measured at Hohenpeißenberg with a smaller difference in summer. This can be explained by the different altitude of the two sites. As the AERONET station at Hohenpeißenberg is located at ∼950 m a.s.l., larger contribution of anthropogenic aerosols is expected. The extremely low AE at the UFS in spring, autumn and winter agrees with the result measured at a plateau site (Lhasa, China, 3,688 m a.s.l.) reported in Xin et al. (2007). The annual mean AE at that site is reported to be 0.06 ± 0.31, which is significantly lower than those measured at low-altitude sites, in particular urban and forest sites. In general, a smaller AE implies larger aerosol particle

sizes (Dubovik et al., 2002). The increased AE at the UFS in summer indicates a
larger contribution of fine particles. The result is consistent with the fact that the
particle size of biogenic secondary aerosols transported from the lower altitudes
to upper altitudes in summer is in general smaller than ice particles.

Chapter 6

Retrieval of total VCDs of O$_3$ and NO$_2$

In this chapter, we present the retrieval of the total VCDs of O$_3$ and NO$_2$ from MAX-DOAS zenith measurements. Since off-zenith spectra were not used in such retrieval, the MAX-DOAS was virtually used as a ZSL-DOAS.

6.1   Basic principle
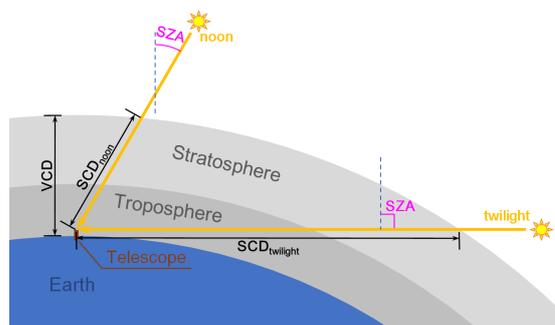
Figure 6.1: Light paths of scattered sunlight at noon and during twilight periods.

The vertical column density (VCD, V) of a certain kind of atmospheric gas refers to the vertically integrated number density:

$$V = \int n(z) \mathrm{d}z, \qquad (6.1)$$

where z is the altitude, and $n(z)$ is the number density at altitude z. In this study,

114

the total VCDs (the VCDs integrated from the ground surface to the top of the atmosphere) of O_3 and NO_2 were retrieved from the zenith spectra measured during twilight periods, i.e. the sunrise and sunset periods, when the SZA is close to 90°. In the retrieval, a fixed zenith spectrum measured at noon was used as the reference spectrum for the DSCD calculation. As illustrated in Figure 6.1, the light path at noon (especially in summer) is much shorter than the one during twilight periods. The air mass factor (AMF, A), which means the ratio between the SCD and the VCD of trace gas, can be calculated by RTM.

For the measurements during a single twilight period (usually about 0.5 h, when 86° < SZA < 90°), based on the the definitions of AMF, SCD, DSCD, and VCD, as well as the assumption that the total VCDs of O_3 and NO_2 are stable within such a short time span, we can derive that

$$\Delta S_i = S_i - S_{\text{ref}} = V \cdot A_i - S_{\text{ref}}, \tag{6.2}$$

where ΔS_i is the ith DSCD measurement during the twilight period, which is the difference between the total SCDs of the ith twilight measurement (S_i) and the reference measurement (S_{ref}). A_i is the AMF corresponding to the ith measurement. As the reference spectrum is fixed and the total VCD (V) is assumed to be constant, the DSCD (ΔS) would be a linear function of the AMF (A). Since we have a number of DSCD measurements during each twilight period and their corresponding AMFs are also available, V and S_{ref} can be derived by applying a linear regression between ΔS_i and A_i. The mean total VCD during the period is then given by the slope of the fitted trend line, and S_{ref} can be derived from the intercept of the linear fit (multiplied by -1). This method is called Langley plot.

Once S_{ref} is known, the VCD of each measurement (V_i) can be calculated:

$$V_i = \frac{\Delta S_i + S_{\text{ref}}}{A_i}, \tag{6.3}$$

and the mean total VCD during the twilight period ($\bar{V}$) can be calculated in a simpler way:

$$\bar{V} = \frac{\sum_{i=1}^{n} V_i}{n}, \tag{6.4}$$

where n is the number of measurements in the period.

The Langley plot method has some limitations. First, the assumption that the total VCD is stable over the twilight period must be fulfilled, however, even if the

plot shows a straight line, this assumptions is not necessarily correct (Marenco, 2007). Second, the AMFs must be accurately calculated, however, the actual AMFs can be influenced by clouds and aerosols, as well as the actual profile of the trace gas. In addition, errors exist in the measured DSCDs, especially due to the varying temperature. Therefore, in most other studies (e.g., Vaughan et al., 1997; Chen, 2008), the Langley plot method was only used to derive S_{ref}, while the total VCDs were calculated using Eq. (6.3) and (6.4), as this method is more robust than the Langley plot method (Bassford et al., 2001).

6.2   DSCD calculation

For the retrieval of the total VCDs of O$_3$ and NO$_2$, the DSCDs were both calculated from VIS spectra using DOAS method. The fit settings are summarized in Table 6.1. We followed the settings recommended by the NDACC (Network for the Detection of Atmospheric Composition Change), except for a slight change of the fitting window of NO$_2$ due to the spectral range of our VIS spectrometer (fitting window starts from 428 nm instead of 425 nm). The DSCDs of O$_3$ were calculated using the 450–550 nm spectral interval, which is called the Chappuis band (Chappuis, 1880; Grebenshchikov et al., 2007). The DSCDs of NO$_2$ were calculated using the fitting window of 428–490 nm. A fixed spectrum measured on the noon of 28 Jun 2012 was used as the reference spectrum, because this spectrum has the lowest O$_3$ absorption over the measurement period. As in the DOAS evaluation in Chapter 5, DSCDs with the RMS of fitting residual larger than 1×10^{-3} were filtered out.

6.3   AMF look-up tables

The AMFs of O$_3$ and NO$_2$ were obtained from the corresponding LUTs developed at BIRA-IASB in support of the NDACC UV-visible WG (Hendrick et al., 2011).

The O$_3$ and NO$_2$ AMF LUTs were both calculated using the UVSPEC/DISORT RTM (Mayer and Kylling, 2005) which is based on the Discrete Ordinate Method and includes a treatment of the multiple scattering in a pseudo-spherical geometry. The AMFs were computed at a single wavelength (500 and 465 nm for O$_3$ and NO$_2$, respectively). An aerosol extinction profile corresponding to background conditions was used for the AMF calculation. It was constructed from

Table 6.1: The DOAS fit settings for O_3 and NO_2 for the retrieval of total VCDs.

| Species | Evaluation species | | Reference |
	O_3	NO_2	
Fitting window	450–500 nm	428–490 nm	
O_3[a] (223 K)	✓	✓	Bogumil et al. (2003)
NO_2[b] (220 K)	✓	✓	Vandaele et al. (1998)
H_2O	✓	✓	Hitran 2004
O_4	✓	✓	Hermans et al. (2003)
Ring	✓	✓	Chance and Spurr (1997)
Polynomial	5th order	5th order	
Intensity offset	linear	linear	

[a] I_0 correction is applied with SCD of 10^{19} molec/cm^2 (Aliwell et al., 2002).
[b] I_0 correction is applied with SCD of 2×10^{16} molec/cm^2 (Aliwell et al., 2002).

the aerosol model of Shettle (1989) included in UVSPEC/DISORT. The temperature profile was from the TOMS (Total Ozone Mapping Spectrometer) version 8 (TV8) climatology (McPeters et al., 2007). A global monthly climatology of the surface albedo was coupled to the interpolation routines so that realistic albedo values could be obtained in a transparent way. This albedo climatology was extracted from the GOME surface albedo database developed by Koelemeijer et al. (2003).

The database of O_3 AMFs is based on the TV8 ozone and temperature profile climatology (Bhartia et al., 2004). The TV8 is a monthly-zonal climatology sorted according to the ozone column. It has been widely used for the retrieval of global total ozone fields from recent US and European UV-VIS nadir sounders (e.g., Bhartia et al., 2004; Coldewey-Egbers et al., 2005; Van Roozendael et al., 2006; Eskes et al., 2005). The parameters considered in building the LUT are wavelength, ground albedo, altitude and SZA.

The database of NO_2 AMFs is based on the harmonic climatology of stratospheric NO_2 profile developed by Lambert et al. (1999, 2000). This climatology consists of a Fourier harmonic decomposition of UARS HALOE v19 and SPOT-4 POAM-III v2 NO_2 profile data records. It has been used for the retrieval of global total ozone fields from recent European UV-VIS nadir sounders (GOME and SCIAMACHY). For the NO_2 AMF calculation, the NO_2 concentration between 20 and 60 km altitude was taken from the climatology of Lambert et al. (1999, 2000). Between 12 and 17 km, the NO_2 profiles were complemented by a climatology derived from SAOZ balloon observations. The NO_2 concentration

was set to zero below 12 km altitude.

6.4   Results and discussions

6.4.1   Langley plots of O_3
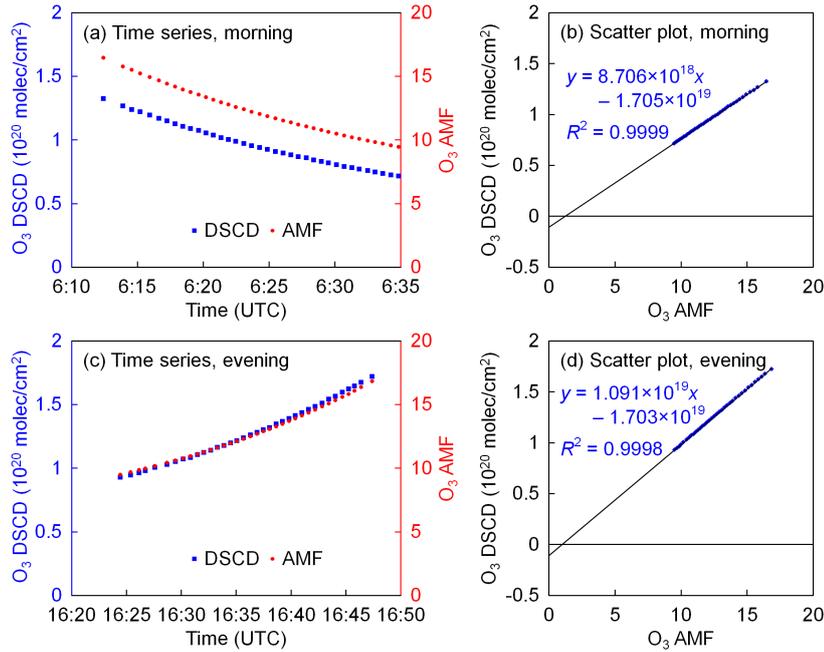
Figure 6.2: Time series of O_3 DSCDs and AMFs (a and c) during the twilight periods of 24 Feb 2014 and the corresponding Langley plots (b and d). The reference spectrum was taken on 28 Jun 2012 at 11:37 UTC.

Figure 6.2 shows the Langley plots of O_3 for the morning and evening twilight periods of 24 February 2014. It can be seen that the AMFs obtained from the LUT are highly correlated with the DSCDs of O_3 during both of the two periods.

Figure 6.3 shows the Langley plot results from February 2012 to February 2016, including O_3 VCDs, correlation coefficients (R^2) and O_3 SCDs of the reference spectrum (S_{ref}) derived from Langley plot. (Note that the results of the twilight periods with less than 10 data were filtered out; for Panels (a) and (c), the results with the correlation coefficient $R^2 < 0.99$ were also filtered out.) The results show that for most of the measurements, the AMFs are highly correlated with the O_3 DSCDs, as the correlation coefficient (R^2) typically varies between 0.99 and 0.9999.
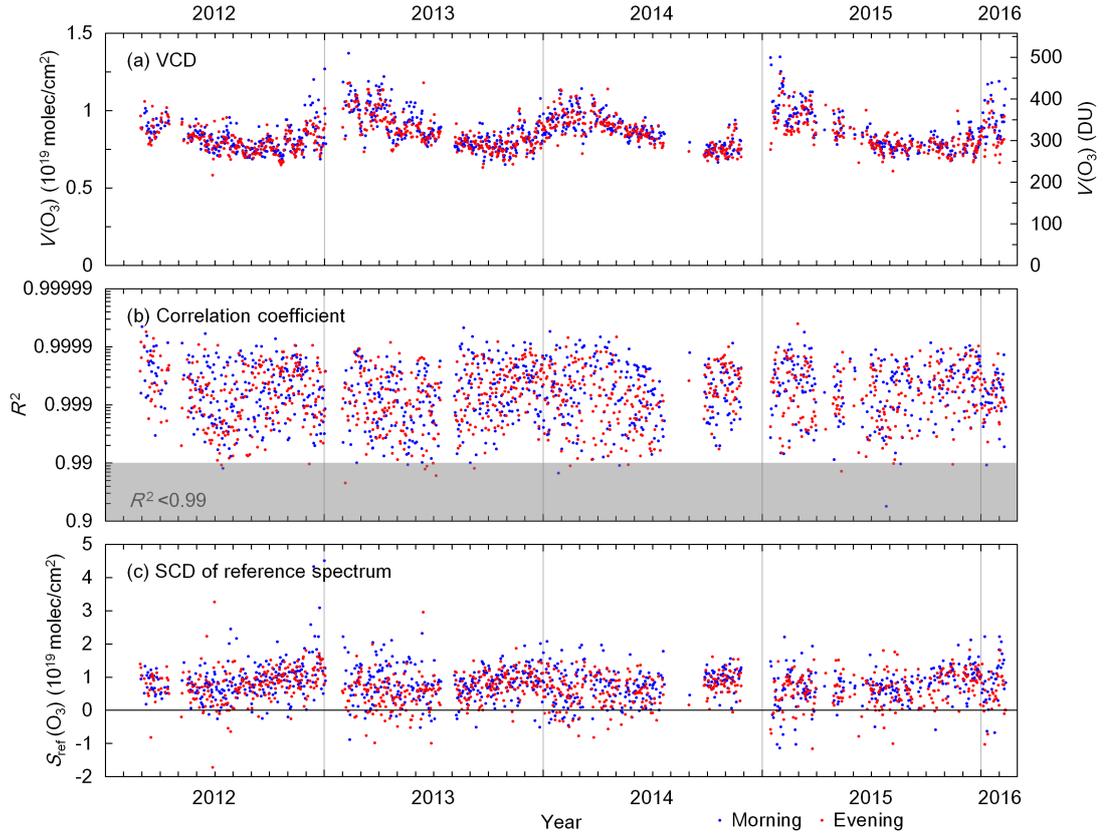
Figure 6.3: Time series of the results of O_3 Langley plots from Feb 2012 to Feb 2016. (a) O_3 VCDs. (b) Correlation coefficients. Note that the y-axis is not linear. (c) O_3 SCDs of the reference spectrum. Note that the twilight periods with less than 10 data were filtered out. In Panels (a) and (c), the data with $R^2 < 0.99$ (shadowed area in Panel (b)) were also filtered out.

However, the O_3 SCDs of the reference spectrum (S_{ref}) derived from the Langley plots vary in a large range, for most measurements they vary from -1×10^{19} to 2×10^{19} molec/cm^2. This can be explained by the existence of clouds or fog. Clouds or fog can affect the effective light path of the photons received by the telescope due to the multiple scattering process, but the AMF LUT cannot predict such changes, and the data are not cloud screened. Therefore, it is difficult to derive the accurate value of S_{ref} from the measurements of a single twilight period. Yet, we can estimate S_{ref} according to the statistical analysis of the long-term results. Figure 6.4 shows the frequency distribution of S_{ref} derived from the long-term Langley plot results. It can be seen that the derived S_{ref} values mostly follow the normal distribution. By fitting the frequency distribution to a Gaussian function, we estimate that $\langle S_{ref}(O_3) \rangle \approx 7.73 \times 10^{18}$ molec/cm^2 (or
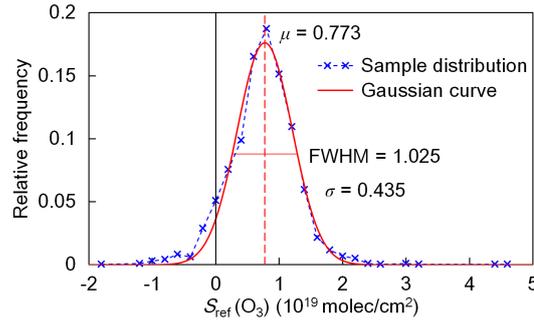
Figure 6.4: Frequency distribution of O_3 SCDs of the reference spectrum (S_{ref}) derived from Langley plots of data from Feb 2012 to Feb 2016 (for bins of 2×10^{18} molec/cm^2) and the Gaussian fit. The results of the twilight periods with less than 10 data and the results with the correlation coefficient $R^2 < 0.99$ were filtered out. The morning and evening results were counted together.

288 DU).

As the reference spectrum has the lowermost O_3 absorption over the years, its AMF should be close to the lower limit of AMF, which equals to $1/\cos(\text{SZA})$. The reference spectrum was measured under an SZA of $24.03°$, therefore its AMF should be only slightly larger than $1/\cos(24.03°) = 1.095$. Then we can estimate that the VCD of the reference measurement is about 7.06×10^{18} molec/cm^2 (or 263 DU). This value is reasonable for the O_3 measurement at the UFS.

In addition, as S_{ref} is much smaller than the DSCDs measured during twilight periods (typically varies between 6×10^{19} and 1.6×10^{20} molec/cm^2) and it is to be divided by the AMF (varies between 9 and 18), the error in S_{ref} does not play an important role in calculating the VCDs using Eq (6.3) and (6.4).

6.4.2   Langley plots of NO_2

Figure 6.5 shows the Langley plots of NO_2 for the morning and evening twilight periods of 24 February 2014. Figure 6.6 shows the Langley plot results from February 2012 to February 2016, including NO_2 VCDs, correlation coefficients (R^2) and NO_2 SCDs of the reference spectrum (S_{ref}) derived from Langley plots. (Note that the results of the twilight periods with less than 10 data were filtered out; For Panels (a) and (c), the data with $R^2 < 0.99$ were also filtered out.) The results show that the correlation between the DSCDs and AMFs of NO_2 is not as good as that of O_3. In most cases, the correlation coefficient (R^2) varies between 0.9 and 0.999; occasionally, the correlation is poor. In addition,
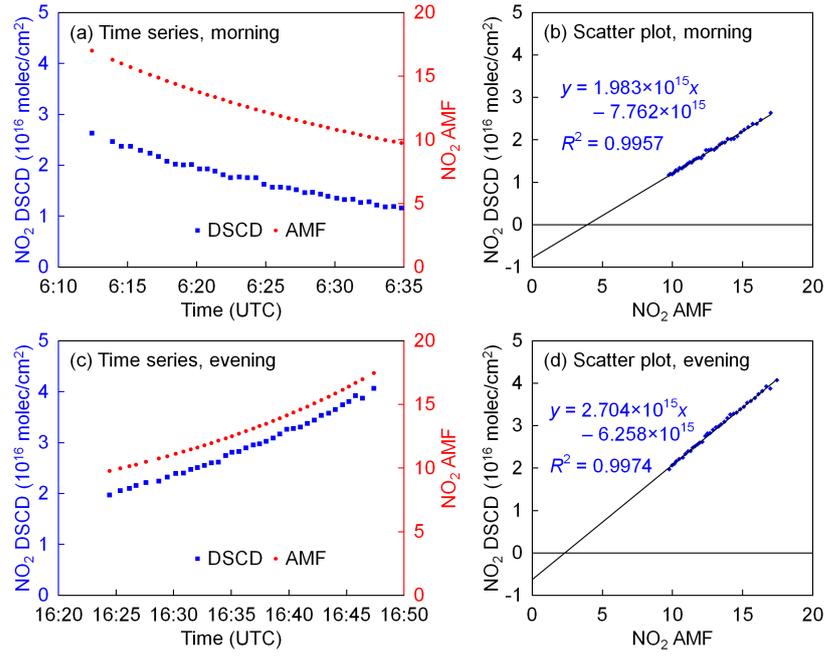
Figure 6.5: Time series of NO_2 DSCDs and AMFs (a and c) measured during the twilight periods of 24 Feb 2014 and the corresponding Langley plots (b and d). The reference spectrum was taken on 28 Jun 2012 at 11:37 UTC.

the correlation in the evening is better than in the morning on average. This is because the tropspheric NO_2 plays an important role in the total column, and the concentration of tropspheric NO_2 is unstable. The variation is especially strong in the morning due to the increasing sunshine. Moreover, such variation cannot be predicted by the AMF LUT.

The frequency distribution of the NO_2 SCDs of the reference spectrum (S_{ref}) derived from the long-term Langley plot results is shown in Figure 6.7. The derived S_{ref} values typically vary from 0 to 1.5×10^{16} molec/cm^2, and the values follow the normal distribution as well. Therefore, we estimate the $\langle S_{ref} \rangle$ of NO_2 in the same way as the $\langle S_{ref} \rangle$ of O_3. By fitting the frequency distribution to a Gaussian function, we estimate that $\langle S_{ref}(NO_2) \rangle \approx 7.72 \times 10^{15}$ molec/cm^2. Consequently, the VCD of the reference measurement is about 7.05×10^{15} molec/cm^2. This value is normal for a summer noon.
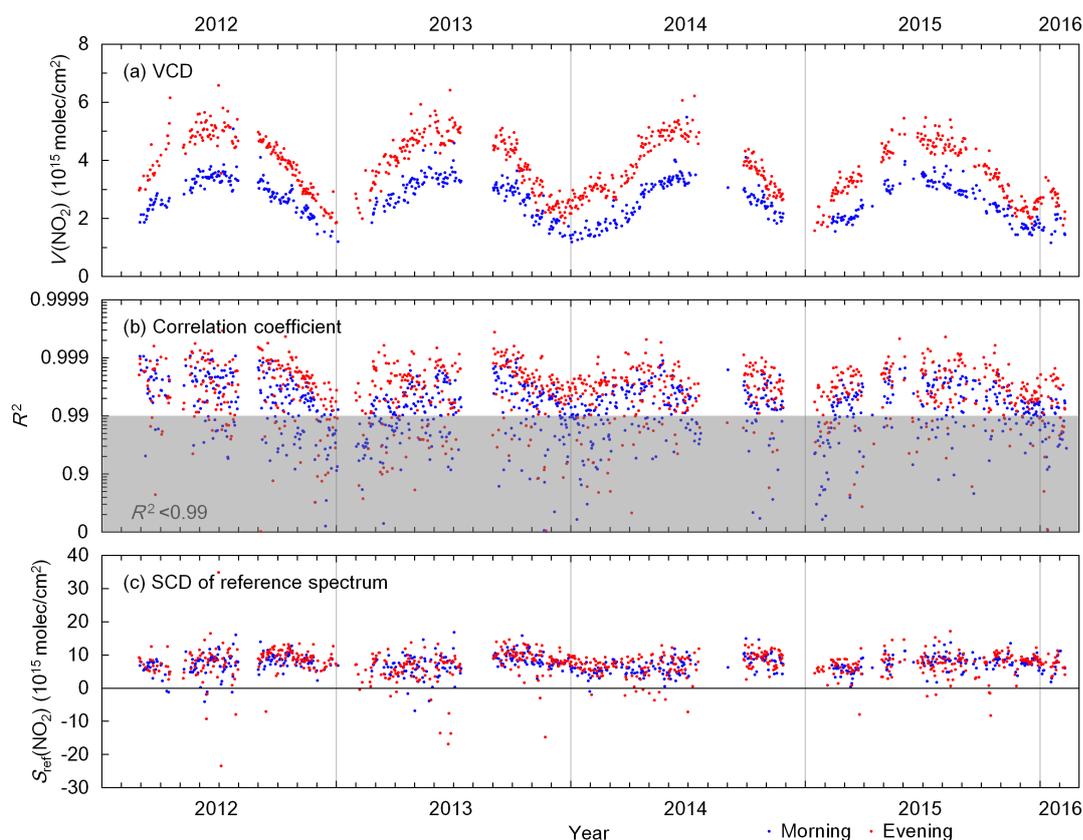
Figure 6.6: Time series of the results of NO_2 Langley plots from Feb 2012 to Feb 2016. (a) NO_2 VCDs. (b) Correlation coefficients. Note that the y-axis is not linear. (c) NO_2 SCDs of the reference spectrum. Note that the twilight periods with less than 10 data were filtered out. In Panels (a) and (c), the data with $R^2 < 0.99$ (shadowed area in Panel (b)) were also filtered out.

6.4.3 Satellite validation

Figure 6.8 shows the time series of the VCDs of O_3 and NO_2 measured by the UFS MAX-DOAS and calculated using Eq. (6.3) and (6.4) (blue and red dots), as well as the O_3 and NO_2 VCDs measured by the GOME-2 instrument on the MetOp-A satellite (green triangles). The satellite data are available from February 2012 to December 2014. The satellite data are the averages of all the original VCD data within $150\,\mathrm{km}$ from the UFS. The MetOp-A satellite was in a sun-synchronous orbit, and all of its data points were measured at 9:30 local time. Figure 6.9 shows the comparison between the MAX-DOAS and satellite results. The MAX-DOAS results derived by Langley plots and by Eq. (6.3) and (6.4) are both compared.

The results show that the VCDs of O_3 measured by MAX-DOAS in both
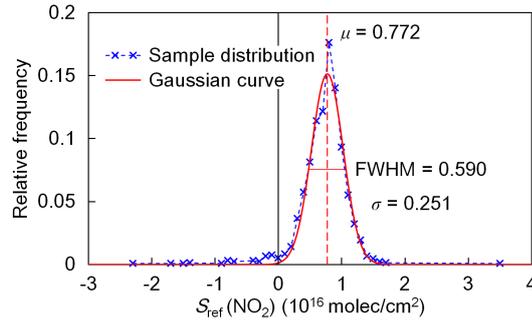
Figure 6.7: Frequency distribution of NO_2 SCDs of the reference spectrum (S_{ref}) derived from Langley plots of data from Feb 2012 to Feb 2016 (for bins of 1×10^{15} molec/cm^2) and the Gaussian fit. The results of the twilight periods with less than 10 data and the results with the correlation coefficient $R^2 < 0.99$ were filtered out. The morning and evening results were counted together.
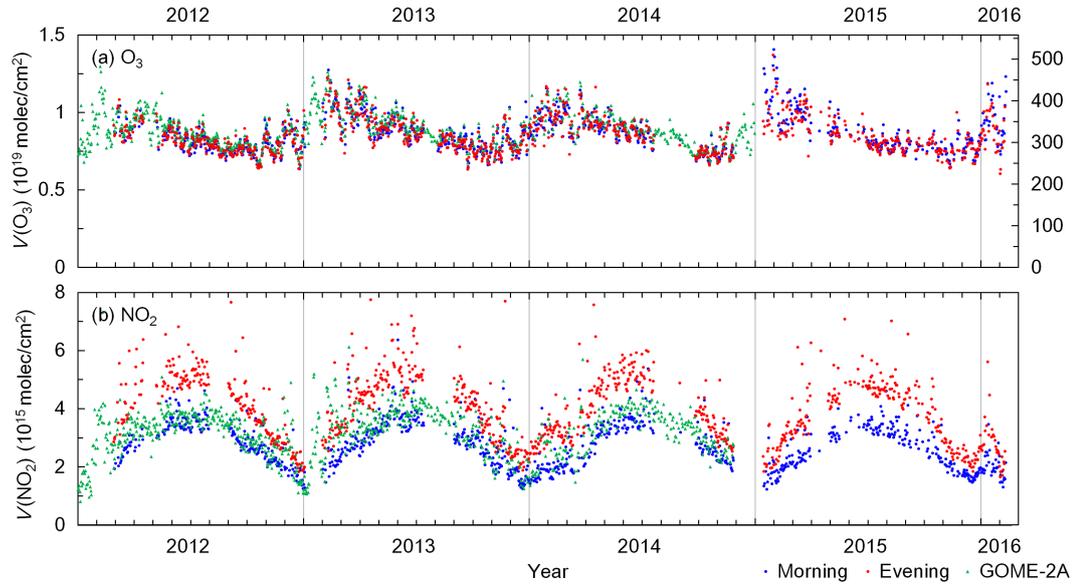
Figure 6.8: Time series of the VCDs of (a) O_3 and (b) NO_2 measured by MAX-DOAS and calculated using Eq. (6.3) and (6.4) (blue and red dots represent morning and evening data, respectively), as well as the O_3 and NO_2 VCDs measured by the GOME-2 instrument on the MetOp-A satellite (green triangles).

mornings and evenings agree well with the satellite results. In addition, the results calculated using Eq. (6.3) and (6.4) agree with the satellite data better than the results derived by Langley plots. This implies that the former method is more robust than the latter. This conclusion coincides with other studies. The O_3 VCDs measured by the MAX-DOAS at the UFS are on average slightly smaller
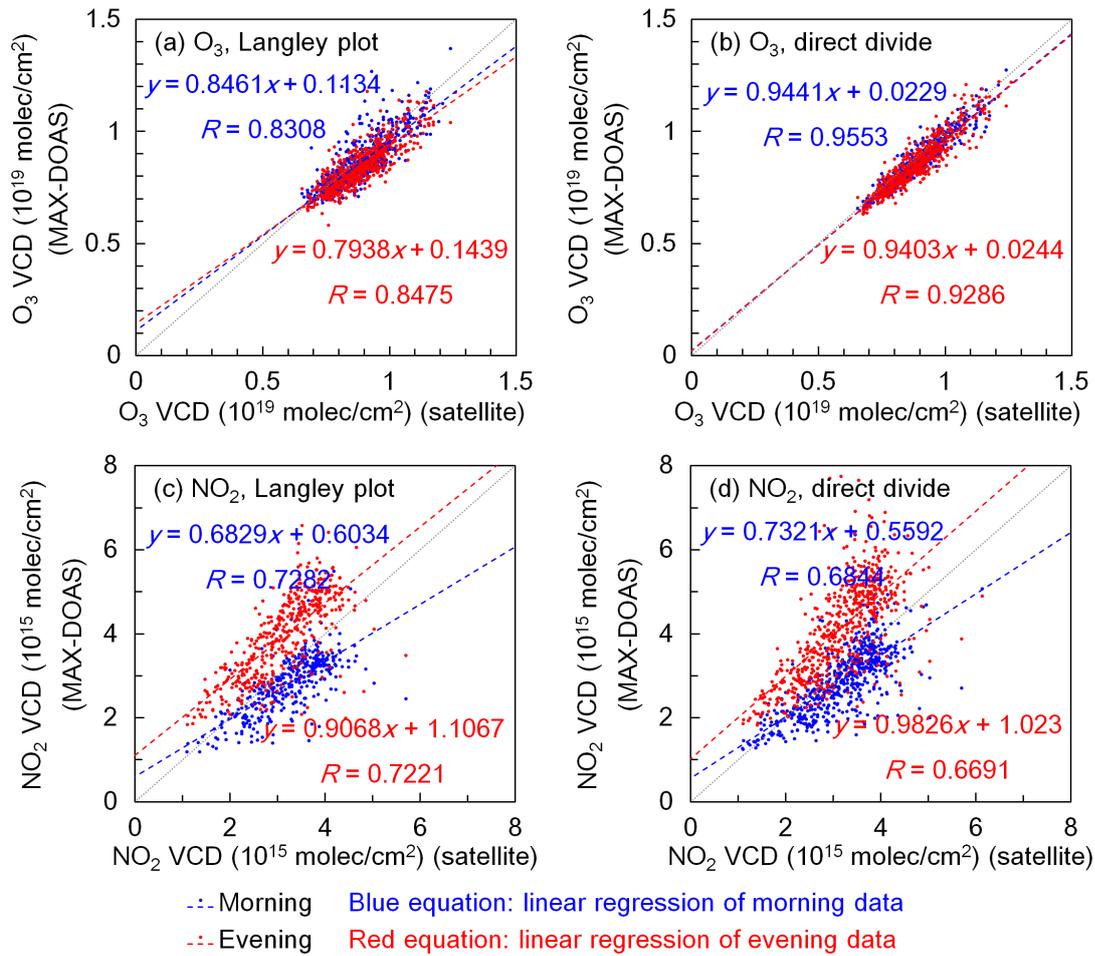
Figure 6.9: Comparison of the total VCDs of O_3 (a and b) and NO_2 (c and d) measured by the UFS MAX-DOAS and the GOME-2 instrument on the MetOp-A satellite. In Panels (a) and (c), the MAX-DOAS data were derived by Langley plots; in Panels (b) and (d), the MAX-DOAS data were calculated using Eq. (6.3) and (6.4).

than the satellite results, this is because the UFS is located at a high altitude, while the satellite measurements include many low-altitude measurements which have stronger O_3 absorption due to the longer light path in the troposphere.

For the VCDs of NO_2, the agreement between the MAX-DOAS and satellite results is weaker comparing to O_3, regardless of the calculation method. This can be explained from two aspects. First, unlike O_3, the concentration of NO_2 has a strong diurnal cycle (it can be seen that the morning and evening MAX-DOAS results differ a lot), and the MAX-DOAS and satellite results were not measured at the same time. Second, the satellite results cover some polluted

areas like Munich and Innsbruck, while the MAX-DOAS only measures at the UFS. For both mornings and evenings, the Langley plot results agree with the satellite results slightly better than the results calculated using Eq. (6.3) and (6.4). However, it should be noted that they are not fully comparable, because for Langley plot results, 37% of the morning data and 22% of the evening data were filtered out due to their low correlation coefficients ($R^2 < 0.99$).

6.4.4   Temporal variation of the VCDs of O_3 and NO_2
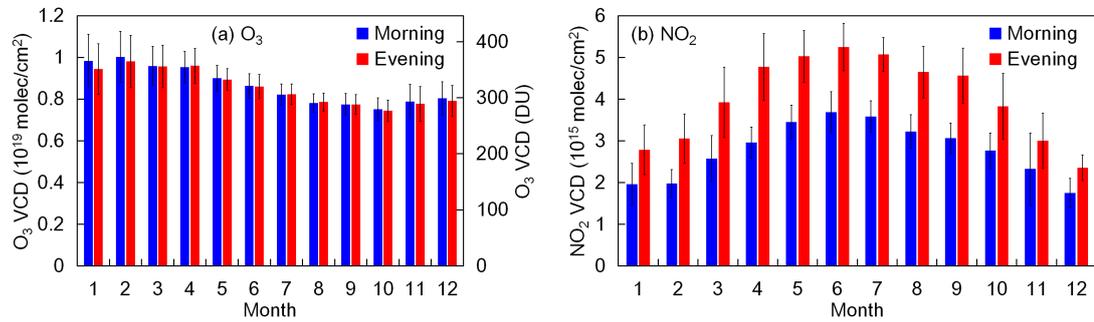
Figure 6.10: Annual variation patterns of the VCDs of (a) O_3 and (b) NO_2, averaged from the data from Feb 2012 to Feb 2016. The original data were calculated using Eq. (6.3) and (6.4). The error bars indicate the standard deviations.

Table 6.2: Seasonal average VCDs of O_3 and NO_2 measured by the MAX-DOAS and calculated using Eq. (6.3) and (6.4), averaged from the data from Feb 2012 to Feb 2016.

Season	O_3 (molec/cm^2)		NO_2 (molec/cm^2)	
	Morning	Evening	Morning	Evening
Spring (MAM)	9.37×10^{18} (349 DU)	9.37×10^{18} (349 DU)	2.97×10^{15}	4.52×10^{15}
Summer (JJA)	8.24×10^{18} (307 DU)	8.25×10^{18} (307 DU)	3.59×10^{15}	5.10×10^{15}
Autumn (SON)	7.70×10^{18} (287 DU)	7.64×10^{18} (284 DU)	2.69×10^{15}	3.73×10^{15}
Winter (DJF)	9.26×10^{18} (345 DU)	9.03×10^{18} (336 DU)	1.89×10^{15}	2.72×10^{15}

Figure 6.10 shows the annual variation patterns of the VCDs of O_3 and NO_2, and Table 6.2 summarizes the seasonally averaged VCDs of O_3 and NO_2. The

data were averaged from the MAX-DOAS results (calculated using Eq. (6.3) and (6.4)) from February 2012 to February 2016.

The results show that among the four seasons, the VCD of O_3 is highest in spring and lowest in autumn. The spring average is larger than the autumn average by 22% and 23% for morning and evening data, respectively. Although the formation of O_3 requires UV radiation and the solar radiation is strongest in summer, the VCD of O_3 does not peak in summer. This might be caused by the strong exchange of air between the stratosphere and the troposphere in summer, so that more tropospheric air with low O_3 concentration is transported to the ozone layer.

The VCD of NO_2 is highest in summer and lowest in winter. In addition, it has a much larger yearly amplitude comparing to the VCD of O_3. For both the morning and evening data, the summer average is larger than the winter average by nearly 90%. This can also be explained by the strong vertical exchange of air in summer, so that the pollutants in the PBL are more likely dispersed to the free troposphere and the stratosphere. This result coincides with the annual variation pattern of aerosol load measured at the UFS.

Chapter 7

Conclusions and outlook

In this chapter, we summarize the results and findings of this work and provide directions for future research.

7.1 Summary and conclusions

In this work, we analyzed the long-term spectra measured by the MAX-DOAS instrument at the high-altitude station UFS. In Chapter 4, we presented the cloud-screening method. In Chapter 5, we presented the retrieval of aerosol extinction profiles. In Chapter 6, we presented the retrieval of the total VCDs of O_3 and NO_2 from the zenith measurements during twilight periods.

7.1.1 Cloud screening method

In Chapter 4, we presented the cloud-screening method for the UFS, which is based on the color index (CI) of the zenith spectra.

The CIs were calculated from the UV spectra, defined as the ratio between the radiative intensities at 330 and 390 nm. In order to make the CIs measured during different periods as well as the simulated CIs comparable, CIs were first calibrated following the method suggested in (Wagner et al., 2016), with which measured CIs under overcast skies were fitted to the simulated minimum CIs.

However, we found the further cloud screening method suggested in (Wagner et al., 2016) infeasible for the measurements at the UFS. Instead, we defined SZA-dependent CI thresholds for cloud screening according to the long-term frequency distribution of calibrated CIs. For each SZA, calibrated CIs show a bimodal frequency distribution, and the two peaks correspond to the measurements under

overcast and clear skies. Therefore, the threshold for each SZA was defined as the calibrated CI with the minimum probability between the two distribution peaks, and a 4th order polynomial fitting was applied to smooth the function.

The cloud screening method has been applied to the entire measurement period from February 2012 to February 2016. The percentage of cloudy measurements is highest in summer and lowest in winter. In total, about 60% of the zenith measurements have been identified as cloudy scenes and filtered out for aerosol profile retrieval.

7.1.2   Retrieval of aerosol profiles

Chapter 5 is the major part of this work. In this chapter, we first presented the basic principle of MAX-DOAS aerosol profile retrieval. We found that the commonly used OEM-based retrieval algorithms are not suitable for the high-altitude site, hence we developed a new aerosol profile retrieval algorithm based on a parametrized O_4 DSCD LUT.

We investigated the sensitivity of O_4 absorption to several parameters. According to the measurement sensitivity, aerosol profiles were parametrized as the aerosol extinction coefficients of three layers (0–0.5 km, 0.5–1 km, and 1–2 km). We defined a profiles set which is assumed to include all possible aerosol extinction profiles under cloud-free conditions at the UFS. The profile set consists of 7,553 profiles. O_4 DSCDs at 360 and 477 nm were simulated with all the profiles in the profile set and all possible viewing geometries (with a $1° \times 1°$ SZA-RAA grid). The simulated data were stored in a LUT, and the LUT was used as the forward model in the aerosol profile retrieval. UV and VIS measurements were retrieved separately. In the retrieval of each measurement cycle, the simulated O_4 DSCDs corresponding to all of the profiles in the profile set were obtained from the LUT. The cost function (χ^2) of each profile was then calculated according to the simulated and measured O_4 DSCDs as well as the measurement uncertainties. A comprehensive error analysis was performed to estimate the total uncertainty. Valid profiles were selected from the profile set according to the cost functions. The optimal solution was defined as the weighted mean of all the valid profiles.

A key finding of this study is that elevation-dependent O_4 DSCD scaling factors are needed to bring the measured and simulated O_4 DSCDs into agreement. Based on the assumption that the LUT covers all possible aerosol profiles under clear-sky conditions, we determined the scaling factors according to the statistical

analysis of the long-term measurements. The agreement between measured and simulated O_4 DSCDs has been greatly improved by this correction.

In order to test the effectiveness of the algorithm, we retrieved profiles from synthetic data. The results indicate that our algorithm can reproduce the true profile well, and the retrieval is stable to measurement noise.

The AODs retrieved from the long-term MAX-DOAS measurements were compared to the sun photometer observations at the UFS. The results show reasonable agreement with each other. However, especially in summer, the sun photometer results are systematically larger (by about a factor of 2) than the MAX-DOAS results. This discrepancy is mainly due to the different definitions of AOD measured by the MAX-DOAS and sun photometer. The larger difference in summer also coincides with the ceilometer measurements at the UFS which indicate larger aerosol extinctions at high altitudes in summer. The long-term results show that the aerosol load at the UFS is highest in summer and lowest in winter. High AOD in summer is mainly related to a higher frequency of extended mixing layers which allow particles to disperse from lower to upper altitudes. According to the MAX-DOAS measurements, the mean aerosol extinction decreases with increasing altitude in all seasons, which agrees with the ceilometer measurements. The Ångström exponents derived from MAX-DOAS surface measurements are highest in summer and extremely low in winter, which implies a smaller particle size in summer. This might be due to a significant contribution from biogenic sources in summer.

The study demonstrated that our aerosol profile retrieval algorithm is effective for the MAX-DOAS measurements at the UFS. Since the profile set only includes reasonable profiles and the final solution is calculated from the weighted mean of all valid profiles, and because the retrieval does not rely on a priori profiles, many of the limitations of OEM-based retrieval algorithms have been overcome. In addition, as the O_4 DSCDs of all possible profiles were pre-calculated, our method significantly reduces the computational time, so that real-time retrievals should be possible. However, the pre-calculation of the LUT database requires massive computational efforts. Therefore, this method is more suitable for long-term measurements.

7.1.3   Retrieval of total VCDs of O_3 and NO_2

In Chapter 6, we presented the retrieval of the total VCDs of O_3 and NO_2 from the zenith spectra measured during twilight periods.

We first introduced the principle of the retrieval method, including the Langley plot method. Then we introduced the O_3 and NO_2 AMF LUTs developed at BIRA-IASB in support of the NDACC UV-visible WG.

Langley plots of O_3 and NO_2 were applied to the long-term measurements at the UFS. The Langley plots of O_3 show that for most measurements, the AMFs obtained from the LUT are highly correlated with the DSCDs, as the correlation coefficient (R^2) typically varies between 0.99 and 0.9999. For the Langley plots of NO_2, the correlation between DSCDs and AMFs is weaker than O_3. The correlation coefficient typically varies from 0.9 to 0.999, and occasionally below 0.5. For both O_3 and NO_2, the SCDs of the reference spectrum (S_{ref}) derived from Langley plots vary in large ranges. However, their long-term distributions both follow the normal distribution. We determined the values of $\langle S_{ref} \rangle$ from the long-term distributions using Gaussian fits. Then we calculated the VCDs of O_3 and NO_2 by directly dividing the SCDs (derived by adding $\langle S_{ref} \rangle$ to the twilight DSCDs) by the AMFs (Eq. (6.3) and (6.4)).

The long-term VCDs of O_3 and NO_2 derived by both Langley plots and Eq. (6.3) and (6.4) were compared to satellite measurements. The comparisons show that the VCDs of O_3 measured by MAX-DOAS in both mornings and evenings agree well with the satellite results, and the results calculated using Eq. (6.3) and (6.4) agree with the satellite data better than the results derived by Langley plots. For the comparison of NO_2, the agreement is weaker than that of O_3, regardless of the calculation method.

The long-term measurements show that the VCD of O_3 is highest in spring and lowest in autumn, while the VCD of NO_2 is highest in summer and lowest in winter. The VCD of NO_2 has a much larger yearly amplitude comparing to the VCD of O_3. For the VCD of NO_2, the summer average is larger than the winter average by nearly 90%; while for O_3, the spring average is larger than the autumn average by $\sim$22%.

7.2 Outlook

The long-term MAX-DOAS measurement at the UFS is a valuable database. Much more information could be retrieved from the spectra. Based on our aerosol profile results, the profiles of trace gases such as NO_2, HCHO, HONO, etc. could be further retrieved. In addition, the amount of certain important stratosphere trace gas species other than O_3 and NO_2 (e.g., BrO and OClO) could also be derived from the spectra. As the UFS is a background station with usually clean air, such measurements would provide valuable information on the stratosphere processes in the northern mid-latitudes. Pollution episodes with enhancement of free tropospheric trace gases can be used to investigate the transport of pollutants.

Our cloud screening method and aerosol profile retrieval algorithm (including the O_4 correction method) can also be adapted to other sites, including low-altitude sites and urban sites (our cloud screening method may only be suitable for unpolluted sites). We hope they can be used in more studies, so that the methods can be further optimized. Further studies may also focus on the combination of the LUT method and machine learning approach.

List of abbreviations

AAC	Aerodynamic Aerosol Classifier
ABL	Atmospheric Boundary Layer
AE	Ångström Exponent
AERONET	AErosol RObotic NETwork
AMF	Air Mass Factor
AMS	Aerosol Mass Spectrometer
AOD	Aerosol Optical Depth
APS	Aerodynamic Particle Sizer
a.s.l.	Above Sea Level
BIRA-IASB	Belgisch Instituut voor Ruimte-Aeronomie - Institut d'Aéronomie Spatiale de Belgique (Belgian Institute for Space Aeronomy)
CCD	Charge Coupled Device
CE-DOAS	Cavity Enhanced Differential Optical Absorption Spectroscopy
CI	Color Index
CL	ChemiLuminescence
CPC	Condensation Particle Counter
DAMF	Differential Air Mass Factor
DC	Dark Current
DMA	Differential Mobility Analyzer
DOAS	Differential Optical Absorption Spectroscopy
DSCD	Differential Slant Column Density
DWD	Deutscher WetterDienst (German Weather Service)
EAS	Electrical Aerosol Spectrometer
FOV	Field Of View
FTIR	Fourier Transform InfraRed
FWHM	Full Width at Half Maximum

GOME	Global Ozone Monitoring Experiment
ILAS	Improved Limb Atmospheric Spectrometer
IPCC	Intergovernmental Panel on Climate Change
LIDORT	LInearized Discrete Ordinate Radiative Transfer
LMU	Ludwig-Maximilians-Universität München (Ludwig Maximilian University of Munich)
LP-DOAS	Long Path Differential Optical Absorption Spectroscopy
LUT	Look-Up Table
MAX-DOAS	Multi-AXis Differential Optical Absorption Spectroscopy
MPIC	Max-Planck-Institut für Chemie (Max Planck Institute for Chemistry)
NDACC	Network for the Detection of Atmospheric Composition Change
OEM	Optimal Estimation Method
OMI	Ozone Monitoring Instrument
OSIRIS	Optical Spectrograph and InfraRed Imager System
PBL	Planetary Boundary Layer
PC	Personal Computer
PM	Particulate Matters
ppbv	Part(s) Per Billion by Volume
ppmv	Part(s) Per Million by Volume
pptv	Part(s) Per Trillion by Volume
RAA	Relative solar Azimuth Angle
RRS	Rotational Raman Scattering
RTE	Radiative Transfer Equation
RTM	Radiative Transfer Model
RVRS	Rotiational Vibrational Raman Scattering
SAA	Solar Azimuth Angle
SCD	Slant Column Density
SCIAMACHY	SCanning Imaging Absorption spectroMeter for Atmospheric CHartographY
SH	Scaling Height
SNR	Signal-to-Noise Ratio
SSA	Single Scattering Albedo
TDLAS	Tunable Diode Laser Absorption Spectroscopy
TOMS	Total Ozone Mapping Spectrometer
TROPOMI	TROPOspheric Monitoring Instrument

TV8	TOMS (Total Ozone Mapping Spectrometer) Version 8
UFS	UmweltForschungsstation Schneefernerhaus (Environment Research Station Schneefernerhaus)
UV	UltraViolet
VCD	Vertical Column Density
VMR	Volume Mixing Ratio
VIS	VISible
WHO	World Health Organization
WPS	Wide-range Particle Spectrometer
ZSL-DOAS	Zenith Scattered Light Differential Optical Absorption Spectroscopy

Acknowledgment

References

Aben, I., Stam, D., and Helderman, F.: The Ring effect in skylight polarisation, Geophysical research letters, 28, 519–522, 2001.

Ahrens, C. D. and Henson, R.: Meteorology today: an introduction to weather, climate, and the environment, Cengage Learning, 2021.

Alicke, B., Hebestreit, K., Stutz, J., and Platt, U.: Iodine oxide in the marine boundary layer, Nature, 397, 572, 1999.

Aliwell, S. R., Roozendael, M. V., Johnston, P. V., Richter, A., Wagner, T., Arlander, D. W., Burrows, J. P., Fish, D. J., Jones, R. L., Tørnkvist, K. K., Lambert, J.-C., Pfeilsticker, K., and Pundt, I.: Analysis for BrO in zenith-sky spectra: An intercomparison exercise for analysis improvement, Journal of Geophysical Research: Atmospheres, 107, ACH 10–1–ACH 10–20, doi:10.1029/2001JD000329, 2002.

Almeida-Silva, M., Almeida, S. M., Freitas, M. C., Pio, C. A., Nunes, T., and Cardoso, J.: Impact of Sahara Dust Transport on Cape Verde Atmospheric Element Particles, Journal of Toxicology and Environmental Health, Part A, 76, 240–251, doi:10.1080/15287394.2013.757200, 2013.

Anderson, G. P., Clough, S. A., Kneizys, F., Chetwynd, J. H., and Shettle, E. P.: AFGL atmospheric constituent profiles (0.120 km), Tech. rep., AIR FORCE GEOPHYSICS LAB HANSCOM AFB MA, 1986.

Ångström, A.: On the atmospheric transmission of sun radiation. II, Geografiska Annaler, 12, 130–159, 1930.

Ball, S. M., Langridge, J. M., and Jones, R. L.: Broadband cavity enhanced absorption spectroscopy using light emitting diodes, Chemical Physics Letters, 398, 68–74, doi:http://dx.doi.org/10.1016/j.cplett.2004.08.144, 2004.

Bassford, M. R., McLinden, C. A., and Strong, K.: Zenith-sky observations of stratospheric gases: the sensitivity of air mass factors to geophysical parameters and the influence of tropospheric clouds, Journal of Quantitative Spectroscopy and Radiative Transfer, 68, 657–677, 2001.

Beirle, S., Kühl, S., Puķīte, J., and Wagner, T.: Retrieval of tropospheric column densities of NO_2 from combined SCIAMACHY nadir/limb measurements, Atmospheric Measurement Techniques, 3, 283–299, 2010.

Bellouin, N., Boucher, O., Haywood, J., and Reddy, M. S.: Global estimate of aerosol direct radiative forcing from satellite measurements, Nature, 438, 1138–1141, doi:doi:10.1038/nature04348, 2005.

Bhartia, P. K., Wellemeyer, C. G., Taylor, S. L., Nath, N., and Gopolan, A.: Solar Backscatter Ultraviolet (SBUV) version 8 profile algorithm, in: Proceedings of the Quadrennial Ozone Symposium, pp. 295–296, 2004.

Bogumil, K., Orphal, J., Homann, T., Voigt, S., Spietz, P., Fleischmann, O., Vogel, A., Hartmann, M., Kromminga, H., Bovensmann, H., Frerick, J., and Burrows, J.: Measurements of molecular absorption spectra with the SCIAMACHY pre-flight model: instrument characterization and reference data for atmospheric remote-sensing in the 230-2380 nm region, Journal of Photochemistry and Photobiology A: Chemistry, 157, 167–184, doi:http://dx.doi.org/10.1016/S1010-6030(03)00062-5, atmospheric Photochemistry, 2003.

Bösch, T., Rozanov, V., Richter, A., Peters, E., Rozanov, A., Wittrock, F., Merlaud, A., Lampel, J., Schmitt, S., de Haij, M., Berkhout, S., Henzing, B., Apituley, A., den Hoed, M., Vonk, J., Tiefengraber, M., Müller, M., and Burrows, J. P.: BOREAS — a new MAX-DOAS profile retrieval algorithm for aerosols and trace gases, Atmospheric Measurement Techniques, 11, 6833–6859, doi:10.5194/amt-11-6833-2018, URL `https://www.atmos-meas-tech.net/11/6833/2018/`, 2018.

Bovensmann, H., Burrows, J., Buchwitz, M., Frerick, J., Noël, S., Rozanov, V., Chance, K., and Goede, A.: SCIAMACHY: Mission objectives and measurement modes, Journal of the Atmospheric Sciences, 56, 127–150, 1999.

Brook, R. D., Rajagopalan, S., Pope, C. A., Brook, J. R., Bhatnagar, A., Diez-Roux, A. V., Holguin, F., Hong, Y., Luepker, R. V., Mittleman, M. A., Peters,

A., Siscovick, D., Smith, S. C., Whitsel, L., and Kaufman, J. D.: Particulate Matter Air Pollution and Cardiovascular Disease, Circulation, 121, 2331–2378, doi:10.1161/CIR.0b013e3181dbece1, 2010.

Brown, S. S.: Absorption Spectroscopy in High-Finesse Cavities for Atmospheric Studies, Chemical Reviews, 103, 5219–5238, doi:10.1021/cr020645c, 2003.

Burrows, J., Platt, U., Chance, K., Vountas, M., Rozanov, V., Richter, A., Haug, H., and Marquard, L.: Study of the Ring Effect, Noordivijk, The Netherlands: European Space Agency, 1996.

Burrows, J. P., Weber, M., Buchwitz, M., Rozanov, V., Ladstätter-Weißenmayer, A., Richter, A., DeBeek, R., Hoogen, R., Bramstedt, K., Eichmann, K.-U., et al.: The global ozone monitoring experiment (GOME): Mission concept and first scientific results, Journal of the Atmospheric Sciences, 56, 151–175, 1999.

Callies, J., Corpaccioli, E., Eisinger, M., Hahne, A., and Lefebvre, A.: GOME-2-Metop's second-generation sensor for operational ozone monitoring, ESA bulletin, 102, 28–36, 2000.

Chan, K., Wiegner, M., Wenig, M., and Pöhler, D.: Observations of tropospheric aerosols and NO_2 in Hong Kong over 5 years using ground based MAX-DOAS, Science of The Total Environment, doi:https://doi.org/10.1016/j.scitotenv.2017.10.153, 2017.

Chan, K. L.: Biomass burning sources and their contributions to the local air quality in Hong Kong, Science of The Total Environment, 596-597, 212–221, doi:https://doi.org/10.1016/j.scitotenv.2017.04.091, 2017.

Chan, K. L. and Chan, K. L.: Aerosol optical depths and their contributing sources in Taiwan, Atmospheric Environment, 148, 364–375, doi:http://dx.doi.org/10.1016/j.atmosenv.2016.11.011, 2017.

Chan, K. L., Hartl, A., Lam, Y. F., Xie, P. H., Liu, W. Q., Cheung, H. M., Lampel, J., Pöhler, D., Li, A., Xu, J., Zhou, H. J., Ning, Z., and Wenig, M. O.: Observations of tropospheric NO_2 using ground based MAX-DOAS and OMI measurements during the Shanghai World Expo 2010, Atmospheric Environment, 119, 45–58, doi:http://dx.doi.org/10.1016/j.atmosenv.2015.08.041, 2015.

Chan, K. L., Wiegner, M., Flentje, H., Mattis, I., Wagner, F., Gasteiger, J., and Geiß, A.: Evaluation of ECMWF-IFS (version 41R1) operational model forecasts of aerosol transport by using ceilometer network measurements, Geoscientific Model Development, 11, 3807–3831, doi:10.5194/gmd-11-3807-2018, URL https://www.geosci-model-dev.net/11/3807/2018/, 2018.

Chance, K. and Kurucz, R.: An improved high-resolution solar reference spectrum for earth's atmosphere measurements in the ultraviolet, visible, and near infrared, Journal of Quantitative Spectroscopy and Radiative Transfer, 111, 1289–1295, doi:https://doi.org/10.1016/j.jqsrt.2010.01.036, 2010.

Chance, K. and Orphal, J.: Revised ultraviolet absorption cross sections of H_2CO for the HITRAN database, Journal of Quantitative Spectroscopy and Radiative Transfer, 112, 1509–1510, doi:https://doi.org/10.1016/j.jqsrt.2011.02.002, 2011.

Chance, K. V. and Spurr, R. J.: Ring effect studies: Rayleigh scattering, including molecular parameters for rotational Raman scattering, and the Fraunhofer spectrum, Applied optics, 36, 5224–5230, 1997.

Chandrasekhar, S.: Radiative Transfer Dover Publications Inc, New York, 1960.

Chapman, S.: On ozone and atomic oxygen in the upper atmosphere, Philosophical Magazine Series 7, 10, 369–383, doi:10.1080/14786443009461588, 1930.

Chappuis, J.: Sur le spectre d'absorption de l'ozone, CR Acad Sci Paris, 91, 985–986, 1880.

Charlson, R. J., Schwartz, S. E., Hales, J. M., Cess, R. D., Coakley, J. A., Hansen, J. E., and Hofmann, D. J.: Climate Forcing by Anthropogenic Aerosols, Science, 255, 423–430, doi:10.1126/science.255.5043.423, 1992.

Chen, D.: Study on Atmospheric Trace Gas Measurements Using Zenith-sky Scattered Light - DOAS Technique, Master's thesis, Fudan University, 2008.

Chen, D., Zhou, B., Beirle, S., Chen, L. M., and Wagner, T.: Tropospheric NO_2 column densities deduced from zenith-sky DOAS measurements in Shanghai, China, and their application to satellite validation, Atmospheric Chemistry and Physics, 9, 3641–3662, doi:10.5194/acp-9-3641-2009, 2009.

Clémer, K., Van Roozendael, M., Fayt, C., Hendrick, F., Hermans, C., Pinardi, G., Spurr, R., Wang, P., and De Mazière, M.: Multiple wavelength retrieval of tropospheric aerosol optical properties from MAXDOAS measurements in Beijing, Atmospheric Measurement Techniques, 3, 863–878, doi: 10.5194/amt-3-863-2010, 2010.

Coldewey-Egbers, M., Weber, M., Lamsal, L. d., Beek, R. d., Buchwitz, M., and Burrows, J.: Total ozone retrieval from GOME UV spectral data using the weighting function DOAS approach, Atmospheric Chemistry and Physics, 5, 1015–1025, 2005.

Constantin, D.-E., Merlaud, A., Van Roozendael, M., Voiculescu, M., Fayt, C., Hendrick, F., Pinardi, G., and Georgescu, L.: Measurements of Tropospheric NO_2 in Romania Using a Zenith-Sky Mobile DOAS System and Comparisons with Satellite Observations, Sensors, 13, 3922–3940, doi:10.3390/s130303922, 2013.

Crutzen, P. J.: The influence of nitrogen oxides on the atmospheric ozone content, Quarterly Journal of the Royal Meteorological Society, 96, 320–325, doi:10.1002/qj.49709640815, 1970.

Czerny, M. and Turner, A. F.: Über den Astigmatismus bei Spiegelspektrometern, Zeitschrift für Physik, 61, 792–797, doi:10.1007/BF01340206, URL `https://doi.org/10.1007/BF01340206`, 1930.

Deutschmann, T.: Atmospheric radiative transfer modelling with Monte Carlo methods, Institute of Environmental Physics, University of Heidelberg, p. 3935, 2008.

Dubovik, O., Smirnov, A., Holben, B., King, M., Kaufman, Y., Eck, T., and Slutsker, I.: Accuracy assessments of aerosol optical properties retrieved from Aerosol Robotic Network (AERONET) Sun and sky radiance measurements, Journal of Geophysical Research: Atmospheres, 105, 9791–9806, 2000.

Dubovik, O., Holben, B., Eck, T. F., Smirnov, A., Kaufman, Y. J., King, M. D., Tanré, D., and Slutsker, I.: Variability of Absorption and Optical Properties of Key Aerosol Types Observed in Worldwide Locations, Journal of the Atmospheric Sciences, 59, 590–608, doi:10.1175/1520-0469(2002)059$\langle$0590:VOAAOP$\rangle$2.0.CO;2, 2002.

Eisinger, M., Richter, A., Ladstatter-Weißenmayer, A., and Burrows, J.: DOAS Zenith Sky Observations: 1. BrO Measurements over Bremen (53 °N) 1993–1994, Journal of Atmospheric Chemistry, 26, 93–108, doi:10.1023/A: 1005776629692, 1997.

Emeis, S., Forkel, R., Junkermann, W., Schäfer, K., Flentje, H., Gilge, S., Fricke, W., Wiegner, M., Freudenthaler, V., Groß, S., Ries, L., Meinhardt, F., Birmili, W., Münkel, C., Obleitner, F., and Suppan, P.: Measurement and simulation of the 16/17 April 2010 Eyjafjallajökull volcanic ash layer dispersion in the northern Alpine region, Atmospheric Chemistry and Physics, 11, 2689–2701, doi:10.5194/acp-11-2689-2011, URL https://www.atmos-chem-phys.net/11/2689/2011/, 2011.

Engeln, R., Berden, G., Peeters, R., and Meijer, G.: Cavity enhanced absorption and cavity enhanced magnetic rotation spectroscopy, Review of Scientific Instruments, 69, 3763–3769, doi:http://dx.doi.org/10.1063/1.1149176, 1998.

Erle, F., Pfeilsticker, K., and Platt, U.: On the influence of tropospheric clouds on zenith-scattered-light measurements of stratospheric species, Geophysical Research Letters, 22, 2725–2728, doi:10.1029/95GL02789, 1995.

Eskes, H., Brinksma, E., Veefkind, J., De Haan, J., Valks, P., et al.: Retrieval and validation of ozone columns derived from measurements of SCIAMACHY on Envisat, Atmospheric Chemistry and Physics Discussions, 5, 4429–4475, 2005.

Fernald, F. G.: Analysis of atmospheric lidar observations: some comments, Appl. Opt., 23, 652–653, doi:10.1364/AO.23.000652, URL http://ao.osa.org/abstract.cfm?URI=ao-23-5-652, 1984.

Fiedler, S. E., Hese, A., and Ruth, A. A.: Incoherent broad-band cavity-enhanced absorption spectroscopy, Chemical Physics Letters, 371, 284–294, doi:http://dx.doi.org/10.1016/S0009-2614(03)00263-X, 2003.

Fish, D. J. and Jones, R. L.: Rotational Raman scattering and the Ring effect in zenith-sky spectra, Geophysical Research Letters, 22, 811–814, doi:10.1029/95GL00392, 1995.

Franco, B., Hendrick, F., Van Roozendael, M., Müller, J.-F., Stavrakou, T., Marais, E. A., Bovy, B., Bader, W., Fayt, C., Hermans, C., Lejeune, B., Pinardi, G., Servais, C., and Mahieu, E.: Retrievals of formaldehyde from

ground-based FTIR and MAX-DOAS observations at the Jungfraujoch station and comparisons with GEOS-Chem and IMAGES model simulations, Atmospheric Measurement Techniques, 8, 1733–1756, doi:10.5194/amt-8-1733-2015, URL https://www.atmos-meas-tech.net/8/1733/2015/, 2015.

Frieß, U., Monks, P. S., Remedios, J. J., Rozanov, A., Sinreich, R., Wagner, T., and Platt, U.: MAX-DOAS O_4 measurements: A new technique to derive information on atmospheric aerosols: 2. Modeling studies, Journal of Geophysical Research: Atmospheres, 111, doi:10.1029/2005JD006618, 2006.

Frieß, U., Sihler, H., Sander, R., Pöhler, D., Yilmaz, S., and Platt, U.: The vertical distribution of BrO and aerosols in the Arctic: Measurements by active and passive differential optical absorption spectroscopy, Journal of Geophysical Research: Atmospheres, 116, doi:10.1029/2011JD015938, URL https://agupubs.onlinelibrary.wiley.com/doi/abs/10.1029/2011JD015938, 2011.

Frieß, U., Klein Baltink, H., Beirle, S., Clémer, K., Hendrick, F., Henzing, B., Irie, H., de Leeuw, G., Li, A., Moerman, M. M., van Roozendael, M., Shaiganfar, R., Wagner, T., Wang, Y., Xie, P., Yilmaz, S., and Zieger, P.: Intercomparison of aerosol extinction profiles retrieved from MAX-DOAS measurements, Atmospheric Measurement Techniques, 9, 3205–3222, doi:10.5194/amt-9-3205-2016, URL https://www.atmos-meas-tech.net/9/3205/2016/, 2016.

Ganor, E. and Mamane, Y.: Transport of Saharan dust across the eastern Mediterranean, Atmospheric Environment (1967), 16, 581–587, doi:http://dx.doi.org/10.1016/0004-6981(82)90167-6, 1982.

Ghio, A. J. and Devlin, R. B.: Inflammatory lung injury after bronchial instillation of air pollution particles, American journal of respiratory and critical care medicine, 164, 704–708, 2001.

Gielen, C., Van Roozendael, M., Hendrick, F., Pinardi, G., Vlemmix, T., De Bock, V., De Backer, H., Fayt, C., Hermans, C., Gillotay, D., and Wang, P.: A simple and versatile cloud-screening method for MAX-DOAS retrievals, Atmospheric Measurement Techniques, 7, 3509–3527, doi:10.5194/amt-7-3509-2014, 2014.

Grainger, J. F. and Ring, J.: Anomalous Fraunhofer Line Profiles, Nature, 193, 762, doi:10.1038/193762a0, 1962.

Grebenshchikov, S. Y., Qu, Z.-W., Zhu, H., and Schinke, R.: New theoretical investigations of the photodissociation of ozone in the Hartley, Huggins, Chappuis, and Wulf bands, Phys. Chem. Chem. Phys., 9, 2044–2064, doi: 10.1039/B701020F, URL http://dx.doi.org/10.1039/B701020F, 2007.

Halla, J. D., Wagner, T., Beirle, S., Brook, J. R., Hayden, K. L., O'Brien, J. M., Ng, A., Majonis, D., Wenig, M. O., and McLaren, R.: Determination of tropospheric vertical columns of NO_2 and aerosol optical properties in a rural setting using MAX-DOAS, Atmospheric Chemistry and Physics, 11, 12 475–12 498, doi:10.5194/acp-11-12475-2011, 2011.

Hansen, J., Sato, M., and Ruedy, R.: Radiative forcing and climate response, Journal of Geophysical Research: Atmospheres, 102, 6831–6864, doi:10.1029/96JD03436, 1997.

Haug, H.: Raman-Streuung von sonnenlicht in der Erdatmosphäre, Diploma thesis, University of Heidelberg, 1996.

Haywood, J. and Boucher, O.: Estimates of the direct and indirect radiative forcing due to tropospheric aerosols: A review, Reviews of Geophysics, 38, 513–543, doi:10.1029/1999RG000078, 2000.

Heald, C. L., Ridley, D. A., Kroll, J. H., Barrett, S. R. H., Cady-Pereira, K. E., Alvarado, M. J., and Holmes, C. D.: Contrasting the direct radiative effect and direct radiative forcing of aerosols, Atmospheric Chemistry and Physics, 14, 5513–5527, doi:10.5194/acp-14-5513-2014, 2014.

Hendrick, F., Van Roozendael, M., Chipperfield, M. P., Dorf, M., Goutail, F., Yang, X., Fayt, C., Hermans, C., Pfeilsticker, K., Pommereau, J.-P., Pyle, J. A., Theys, N., and De Mazière, M.: Retrieval of stratospheric and tropospheric BrO profiles and columns using ground-based zenith-sky DOAS observations at Harestua, 60°N, Atmospheric Chemistry and Physics, 7, 4869–4885, doi: 10.5194/acp-7-4869-2007, 2007.

Hendrick, F., Pommereau, J.-P., Goutail, F., Evans, R. D., Ionov, D., Pazmino, A., Kyrö, E., Held, G., Eriksen, P., Dorokhov, V., Gil, M., and Van Roozendael, M.: NDACC/SAOZ UV-visible total ozone measurements: improved retrieval and comparison with correlative ground-based and satellite observations, Atmospheric Chemistry and Physics, 11, 5975–5995, doi:10.

5194/acp-11-5975-2011, URL https://www.atmos-chem-phys.net/11/5975/
2011/, 2011.

Hendrick, F., Müller, J.-F., Clémer, K., Wang, P., De Mazière, M., Fayt, C.,
Gielen, C., Hermans, C., Ma, J. Z., Pinardi, G., Stavrakou, T., Vlemmix, T.,
and Van Roozendael, M.: Four years of ground-based MAX-DOAS observations
of HONO and NO_2 in the Beijing area, Atmospheric Chemistry and Physics,
14, 765–781, doi:10.5194/acp-14-765-2014, 2014.

Henyey, L. G. and Greenstein, J. L.: Diffuse radiation in the galaxy, The Astro-
physical Journal, 93, 70–83, 1941.

Hermans, C., Vandaele, A., Fally, S., Carleer, M., Colin, R., Coquart, B., Je-
nouvrier, A., and Merienne, M.-F.: Absorption cross-section of the collision-
induced bands of oxygen from the UV to the NIR, in: Weakly interacting
molecular pairs: unconventional absorbers of radiation in the atmosphere, pp.
193–202, Springer, 2003.

Hilboll, A., Richter, A., Rozanov, A., Hodnebrog, O., Heckel, A., Solberg, S.,
Stordal, F., and Burrows, J.: Improvements to the retrieval of tropospheric
NO_2 from satellite – stratospheric correction using SCIAMACHY limb/nadir
matching and comparison to Oslo CTM2 simulations, Atmospheric Measure-
ment Techniques, 6, 565–584, 2013.

Hinds, W. C.: Aerosol technology: properties, behavior, and measurement of
airborne particles, John Wiley & Sons, 2012.

Holben, B., Eck, T., Slutsker, I., Tanre, D., Buis, J., Setzer, A., Vermote,
E., Reagan, J., Kaufman, Y., Nakajima, T., Lavenu, F., Jankowiak, I., and
Smirnov, A.: AERONET—A Federated Instrument Network and Data Archive
for Aerosol Characterization, Remote Sensing of Environment, 66, 1–16, doi:
http://dx.doi.org/10.1016/S0034-4257(98)00031-5, 1998.

Hönninger, G. and Platt, U.: Observations of BrO and its vertical distribution
during surface ozone depletion at Alert, Atmospheric Environment, 36, 2481–
2489, doi:http://dx.doi.org/10.1016/S1352-2310(02)00104-8, 2002.

Hönninger, G., von Friedeburg, C., and Platt, U.: Multi axis differential optical
absorption spectroscopy (MAX-DOAS), Atmospheric Chemistry and Physics,
4, 231–254, doi:10.5194/acp-4-231-2004, 2004.

Hsu, S.-C., Liu, S. C., Huang, Y.-T., Chou, C. C. K., Lung, S. C. C., Liu, T.-H., Tu, J.-Y., and Tsai, F.: Long-range southeastward transport of Asian biosmoke pollution: Signature detected by aerosol potassium in Northern Taiwan, Journal of Geophysical Research: Atmospheres, 114, doi:10.1029/2009JD011725, 2009.

IPCC: IPCC, 2012: Managing the Risks of Extreme Events and Disasters to Advance Climate Change Adaptation. A Special Report of Working Groups I and II of the Intergovernmental Panel on Climate Change, Cambridge University Press, Cambridge, UK, and New York, NY, USA, 2012.

Irie, H., Kanaya, Y., Akimoto, H., Iwabuchi, H., Shimizu, A., and Aoki, K.: First retrieval of tropospheric aerosol profiles using MAX-DOAS and comparison with lidar and sky radiometer measurements, Atmospheric Chemistry and Physics, 8, 341–350, doi:10.5194/acp-8-341-2008, 2008.

Irie, H., Takashima, H., Kanaya, Y., Boersma, K. F., Gast, L., Wittrock, F., Brunner, D., Zhou, Y., and Van Roozendael, M.: Eight-component retrievals from ground-based MAX-DOAS observations, Atmospheric Measurement Techniques, 4, 1027–1044, doi:10.5194/amt-4-1027-2011, URL `https://www.atmos-meas-tech.net/4/1027/2011/`, 2011.

Irie, H., Nakayama, T., Shimizu, A., Yamazaki, A., Nagai, T., Uchiyama, A., Zaizen, Y., Kagamitani, S., and Matsumi, Y.: Evaluation of MAX-DOAS aerosol retrievals by coincident observations using CRDS, lidar, and sky radiometer inTsukuba, Japan, Atmospheric Measurement Techniques, 8, 2775–2788, doi:10.5194/amt-8-2775-2015, URL `https://www.atmos-meas-tech.net/8/2775/2015/`, 2015.

Isaacs, R., Wang, W.-C., Worsham, R., and Goldenberg, S.: Multiple scattering LOWTRAN and FASCODE models, Applied optics, 26, 1272–1281, 1987.

Jin, J., Ma, J., Lin, W., Zhao, H., Shaiganfar, R., Beirle, S., and Wagner, T.: MAX-DOAS measurements and satellite validation of tropospheric NO_2 and SO_2 vertical column densities at a rural site of North China, Atmospheric Environment, 133, 12–25, doi:http://dx.doi.org/10.1016/j.atmosenv.2016.03.031, 2016.

Jin, X., Cai, X., Huang, Q., Wang, X., Song, Y., and Zhu, T.: Atmospheric Boundary Layer-Free Troposphere Air Exchange in the North China Plain

and its Impact on PM 2.5 Pollution, Journal of Geophysical Research: Atmospheres, 126, doi:10.1029/2021JD034641, 2021.

Johnston, P.: Making UV/Vis Cross sections, reference Fraunhofer and synthetic spectra, Unpublished Manuscript, NIWA, Lauder, 1996.

Johnston, P. V., McKenzie, R. L., Keys, J. G., and Matthews, W. A.: Observations of depleted stratospheric NO_2 following the Pinatubo volcanic eruption, Geophysical Research Letters, 19, 211–213, doi:10.1029/92GL00043, 1992.

Jurgschat, M.: Measurements of free-tropospheric trace gases with the MAX-DOAS method at the Environmental Research Station Schneefernerhaus, Master's thesis, University of Cologne, 2011.

Kanaya, Y., Irie, H., Takashima, H., Iwabuchi, H., Akimoto, H., Sudo, K., Gu, M., Chong, J., Kim, Y. J., Lee, H., Li, A., Si, F., Xu, J., Xie, P.-H., Liu, W.-Q., Dzhola, A., Postylyakov, O., Ivanov, V., Grechko, E., Terpugova, S., and Panchenko, M.: Long-term MAX-DOAS network observations of NO_2 in Russia and Asia (MADRAS) during the period 2007–2012: instrumentation, elucidation of climatology, and comparisons with OMI satellite observations and global model simulations, Atmospheric Chemistry and Physics, 14, 7909–7927, doi:10.5194/acp-14-7909-2014, URL `https://acp.copernicus.org/articles/14/7909/2014/`, 2014.

Klett, J. D.: Stable analytical inversion solution for processing lidar returns, Appl. Opt., 20, 211–220, doi:10.1364/AO.20.000211, URL `http://ao.osa.org/abstract.cfm?URI=ao-20-2-211`, 1981.

Koelemeijer, R., De Haan, J., and Stammes, P.: A database of spectral surface reflectivity in the range 335–772 nm derived from 5.5 years of GOME observations, Journal of Geophysical Research: Atmospheres, 108, 2003.

Kreher, K., Keys, J. G., Johnston, P. V., Platt, U., and Liu, X.: Ground-based measurements of OClO and HCl in austral spring 1993 at Arrival Heights, Antarctica, Geophysical Research Letters, 23, 1545–1548, doi:10.1029/96GL01318, 1996.

Kreher, K., Johnston, P. V., Wood, S. W., Nardi, B., and Platt, U.: Ground-based measurements of tropospheric and stratospheric BrO at Ar-

rival Heights, Antarctica, Geophysical Research Letters, 24, 3021–3024, doi: 10.1029/97GL02997, 1997.

Kreher, K., Van Roozendael, M., Hendrick, F., Apituley, A., Dimitropoulou, E., Frieß, U., Richter, A., Wagner, T., Abuhassan, N., Ang, L., Anguas, M., Bais, A., Benavent, N., Bösch, T., Bognar, K., Borovski, A., Bruchkouski, I., Cede, A., Chan, K. L., Donner, S., Drosoglou, T., Fayt, C., Finkenzeller, H., Garcia-Nieto, D., Gielen, C., Gómez-Martín, L., Hao, N., Herman, J. R., Hermans, C., Hoque, S., Irie, H., Jin, J., Johnston, P., Khayyam Butt, J., Khokhar, F., Koenig, T. K., Kuhn, J., Kumar, V., Lampel, J., Liu, C., Ma, J., Merlaud, A., Mishra, A. K., Müller, M., Navarro-Comas, M., Ostendorf, M., Pazmino, A., Peters, E., Pinardi, G., Pinharanda, M., Piters, A., Platt, U., Postylyakov, O., Prados-Roman, C., Puentedura, O., Querel, R., Saiz-Lopez, A., Schönhardt, A., Schreier, S. F., Seyler, A., Sinha, V., Spinei, E., Strong, K., Tack, F., Tian, X., Tiefengraber, M., Tirpitz, J.-L., van Gent, J., Volkamer, R., Vrekoussis, M., Wang, S., Wang, Z., Wenig, M., Wittrock, F., Xie, P. H., Xu, J., Yela, M., Zhang, C., and Zhao, X.: Intercomparison of NO_2, O_4, O_3 and HCHO slant column measurements by MAX-DOAS and zenith-sky UV–Visible spectrometers during the CINDI-2 campaign, Atmospheric Measurement Techniques Discussions, 2019, 1–58, doi:10.5194/amt-2019-157, URL `https://www.atmos-meas-tech-discuss.net/amt-2019-157/`, 2019.

Lambert, J.-C., Granville, J., Van Roozendael, M., Sarkissian, A., Goutail, F., Müller, J.-F., Pommereau, J.-P., and Russel, J.: A climatology of NO_2 profile for improved air mass factors for ground-based vertical column measurements, in: Stratospheric Ozone 1999, N.R.P. Harris, M. Guirlet, and G.T. Amanatidis (Eds.), Air Pollution Research Report 73 (CEC DG XII), pp. 703–736, 1999.

Lambert, J.-C., Granville, J., Van Roozendael, M., Müller, J.-F., Goutail, F., Pommereau, J.-P., Sarkissian, A., Johnston, P., and Russell III, J.: Global Behaviour of Atmospheric NO_2 as derived from the integrated use of Satellite, Ground-based Network and Balloon Observations, in: Proceedings 19th Quad. Ozone Symp., Sapporo, Japan, pp. 201–202, 2000.

Lampel, J.: Measurements of reactive trace gases in the marine boundary layer using novel DOAS methods, Ph.D. thesis, Heidelberg University, 2014.

Langridge, J. M., Ball, S. M., and Jones, R. L.: A compact broadband cavity

enhanced absorption spectrometer for detection of atmospheric NO_2 using light emitting diodes, Analyst, 131, 916–922, doi:10.1039/B605636A, 2006.

Lee, D. S., Kohler, I., Grobler, E., Rohrer, F., Sausen, R., Gallardo-Klenner, L., Olivier, J. G. J., Dentener, F. J., and Bouwman, A. F.: Estimations of global NO_x emissions and their uncertainties, Atmospheric Environment, 31, 1735–1749, doi:http://dx.doi.org/10.1016/S1352-2310(96)00327-5, 1997.

Lee, H., Irie, H., Kim, Y. J., Noh, Y., Lee, C., Kim, Y., and Chun, K. J.: Retrieval of Aerosol Extinction in the Lower Troposphere Based on UV MAX-DOAS Measurements, Aerosol Science and Technology, 43, 502–509, doi:10.1080/02786820902769691, URL https://doi.org/10.1080/02786820902769691, 2009.

Lee, Y. C., Lam, Y. F., Kuhlmann, G., Wenig, M. O., Chan, K. L., Hartl, A., and Ning, Z.: An integrated approach to identify the biomass burning sources contributing to black carbon episodes in Hong Kong, Atmospheric Environment, 80, 478–487, doi:http://dx.doi.org/10.1016/j.atmosenv.2013.08.030, 2013.

Levelt, P., Van den Oord, G. H. J., Dobber, M., Malkki, A., Visser, H., de Vries, J., Stammes, P., Lundell, J., and Saari, H.: The ozone monitoring instrument, Geoscience and Remote Sensing, IEEE Transactions on, 44, 1093–1101, doi:10.1109/TGRS.2006.872333, 2006.

Levine, R.: McGraw-Hill Encyclopedia of Science and Technology, 1984.

Li, N., Harkema, J. R., Lewandowski, R. P., Wang, M., Bramble, L. A., Gookin, G. R., Ning, Z., Kleinman, M. T., Sioutas, C., and Nel, A. E.: Ambient ultrafine particles provide a strong adjuvant effect in the secondary immune response: implication for traffic-related asthma flares, American Journal of Physiology — Lung Cellular and Molecular Physiology, 299, L374–L383, doi:10.1152/ajplung.00115.2010, 2010a.

Li, X., Brauers, T., Shao, M., Garland, R. M., Wagner, T., Deutschmann, T., and Wahner, A.: MAX-DOAS measurements in southern China: retrieval of aerosol extinctions and validation using ground-based in-situ data, Atmospheric Chemistry and Physics, 10, 2079–2089, doi:10.5194/acp-10-2079-2010, 2010b.

Li, X., Brauers, T., Hofzumahaus, A., Lu, K., Li, Y. P., Shao, M., Wagner, T., and Wahner, A.: MAX-DOAS measurements of NO_2, HCHO and CHOCHO

at a rural site in Southern China, Atmospheric Chemistry and Physics, 13, 2133–2151, doi:10.5194/acp-13-2133-2013, 2013.

Li, Z.: Influence of absorbing aerosols on the inference of solar surface radiation budget and cloud absorption, Journal of Climate, 11, 5–17, doi:http://dx.doi. org/10.1175/1520-0442(1998)011$\langle$0005:IOAAOT$\rangle$2.0.CO;2, 1998.

Li, Z. and Kou, L.: The direct radiative effect of smoke aerosols on atmospheric absorption of visible sunlight, Tellus B, 50, 2011.

Lydolph, P. E., Temple, D., and Temple, D.: The climate of the earth, Government Institutes, 1985.

Ma, J. Z., Beirle, S., Jin, J. L., Shaiganfar, R., Yan, P., and Wagner, T.: Tropospheric NO_2 vertical column densities over Beijing: results of the first three years of ground-based MAX-DOAS measurements (2008–2011) and satellite validation, Atmospheric Chemistry and Physics, 13, 1547–1567, doi: 10.5194/acp-13-1547-2013, 2013.

Marenco, F.: On Langley plots in the presence of a systematic diurnal aerosol cycle centered at noon: A comment on recently proposed methodologies, Journal of Geophysical Research: Atmospheres, 112, 2007.

Mayer, B. and Kylling, A.: Technical note: The libRadtran software package for radiative transfer calculations — description and examples of use, Atmospheric Chemistry and Physics, 5, 1855–1877, doi:10.5194/acp-5-1855-2005, URL https://acp.copernicus.org/articles/5/1855/2005/, 2005.

McPeters, R. D., Labow, G. J., and Logan, J. A.: Ozone climatological profiles for satellite retrieval algorithms, Journal of Geophysical Research: Atmospheres, 112, doi:https://doi.org/10.1029/2005JD006823, URL https://agupubs. onlinelibrary.wiley.com/doi/abs/10.1029/2005JD006823, 2007.

Merlaud, A., Van Roozendael, M., Theys, N., Fayt, C., Hermans, C., Quennehen, B., Schwarzenboeck, A., Ancellet, G., Pommier, M., Pelon, J., Burkhart, J., Stohl, A., and De Mazière, M.: Airborne DOAS measurements in Arctic: vertical distributions of aerosol extinction coefficient and NO_2 concentration, Atmospheric Chemistry and Physics, 11, 9219–9236, doi:10.5194/acp-11-9219-2011, URL https://acp.copernicus.org/articles/11/9219/2011/, 2011.

Mie, G.: Beiträge zur Optik trüber Medien, speziell kolloidaler Metallösungen, Annalen der physik, 330, 377–445, 1908.

Mount, G. H., Sanders, R. W., Schmeltekopf, A. L., and Solomon, S.: Visible spectroscopy at McMurdo Station, Antarctica: 1. Overview and daily variations of NO_2 and O_3, Austral Spring, 1986, Journal of Geophysical Research: Atmospheres, 92, 8320–8328, doi:10.1029/JD092iD07p08320, 1987.

Munro, R., Lang, R., Klaes, D., Poli, G., Retscher, C., Lindstrot, R., Huckle, R., Lacan, A., Grzegorski, M., Holdak, A., et al.: The GOME-2 instrument on the Metop series of satellites: instrument design, calibration, and level 1 data processing — an overview, Atmospheric Measurement Techniques, 9, 1279–1301, 2016.

Murtagh, D., Frisk, U., Merino, F., Ridal, M., Jonsson, A., Stegman, J., Witt, G., Eriksson, P., Jimenez, C., Megie, G., Noe, J. d. l., Ricaud, P., Baron, P., Pardo, J. R., Hauchcorne, A., Llewellyn, E. J., Degenstein, D. A., Gattinger, R. L., Lloyd, N. D., Evans, W. F., McDade, I. C., Haley, C. S., Sioris, C., Savigny, C. v., Solheim, B. H., McConnell, J. C., Strong, K., Richardson, E. H., Leppelmeier, G. W., Kyrola, E., Auvinen, H., and Oikarinen, L.: An overview of the ODIN atmospheric mission, Canadian Journal of Physics, 80, 309–319, doi:10.1139/p01-157, 2002.

Niebling, S.: Langzeit-Messungen von Spurengasen und Aerosolen mittels Multi-Axis-DOAS auf dem Hohenpeißenberg, Master's thesis, Heidelberg University, 2010.

Otten, C., Ferlemann, F., Platt, U., Wagner, T., and Pfeilsticker, K.: Ground-based DOAS UV/visible measurements at Kiruna (Sweden) during the sesame winters 1993/94 and 1994/95., Journal of Atmospheric Chemistry, 30, 141–162, doi:10.1023/A:1005810732347, 1998.

Perner, D. and Platt, U.: Detection of nitrous acid in the atmosphere by differential optical absorption, Geophysical Research Letters, 6, 917–920, doi: 10.1029/GL006i012p00917, URL https://agupubs.onlinelibrary.wiley.com/doi/abs/10.1029/GL006i012p00917, 1979.

Perner, D., Ehhalt, D. H., Pätz, H. W., Platt, U., Röth, E. P., and Volz, A.: OH-Radicals in the lower troposphere, Geophysical Research Letters, 3, 466–

468, doi:10.1029/GL003i008p00466, URL https://agupubs.onlinelibrary.
wiley.com/doi/abs/10.1029/GL003i008p00466, 1976.

Perner, D., Klupfel, T., Parchatka, U., Roth, A., and Jorgensen, T.: Ground-based UV-VIS spectroscopy: Diurnal OClO-profiles during January 1990 above Sondre Stromfjord, Greenland, Geophysical Research Letters, 18, 787–790, doi:10.1029/91GL00171, 1991.

Platt, U. and Perner, D.: Measurements of Atmospheric Trace Gases by Long Path Differential UV/Visible Absorption Spectroscopy, Optical and Laser Remote Sensing, 39, 97–105, doi:10.1007/978-3-540-39552-2_13, 1983.

Platt, U. and Stutz, J.: Differential optical absorption spectroscopy — principles and applications, Springer, 2008.

Platt, U., Perner, D., and Patz, H. W.: Simultaneous measurement of atmospheric CH_2O, O_3, and NO_2 by differential optical absorption, Journal of Geophysical Research: Oceans, 84, 6329–6335, doi:10.1029/JC084iC10p06329, 1979.

Platt, U., Perner, D., Winer, A. M., Harris, G. W., and Pitts Jr., J. N.: Detection of NO_3 in the polluted troposphere by differential optical absorption, Geophysical Research Letters, 7, 89–92, doi:10.1029/GL007i001p00089, URL https://agupubs.onlinelibrary.wiley.com/doi/abs/10.1029/GL007i001p00089, 1980.

Platt, U., Meinen, J., Pöhler, D., and Leisner, T.: Broadband Cavity Enhanced Differential Optical Absorption Spectroscopy (CE-DOAS) — applicability and corrections, Atmospheric Measurement Techniques, 2, 713–23, doi:10.5194/amt-2-713-2009, 2009.

Pommereau, J. P.: Observation of NO_2 diurnal variation in the stratosphere, Geophysical Research Letters, 9, 850–853, doi:10.1029/GL009i008p00850, 1982.

Pujadas, M., Nunez, L., and Lubrani, P.: Assessment of NO_2 satellite observations for en-route aircraft emissions detection, Remote Sensing of Environment, 115, 3298–3312, doi:http://dx.doi.org/10.1016/j.rse.2011.07.013, 2011.

Ramanathan, V. and Crutzen, P.: New Directions: Atmospheric Brown "Clouds", Atmospheric Environment, 37, 4033–4035, doi:http://dx.doi.org/10.1016/S1352-2310(03)00536-3, 2003.

Rayleigh, L.: XXXIV. On the transmission of light through an atmosphere containing small particles in suspension, and on the origin of the blue of the sky, The London, Edinburgh, and Dublin Philosophical Magazine and Journal of Science, 47, 375–384, 1899.

Richter, A., Eisinger, M., Ladstatter-weisenmayer, A., and Burrows, J.: DOAS Zenith Sky Observations: 2. Seasonal Variation of BrO Over Bremen (53 °N) 1994–1995, Journal of Atmospheric Chemistry, 32, 83–99, doi:10.1023/A: 1006077725894, 1999.

Richter, A., Burrows, J. P., Nüß, H., Granier, C., and Niemeier, U.: Increase in tropospheric nitrogen dioxide over China observed from space, Nature, 437, 129–132, 2005.

Risius, S., Xu, H., Di Lorenzo, F., Xi, H., Siebert, H., Shaw, R. A., and Bodenschatz, E.: Schneefernerhaus as a mountain research station for clouds and turbulence, Atmospheric Measurement Techniques, 8, 3209–3218, doi: 10.5194/amt-8-3209-2015, 2015.

Rodgers, C. D.: Inverse methods for atmospheric sounding: Theory and practice, vol. 2, World scientific, 2000.

Roscoe, H. K., Van Roozendael, M., Fayt, C., du Piesanie, A., Abuhassan, N., Adams, C., Akrami, M., Cede, A., Chong, J., Clémer, K., Friess, U., Gil Ojeda, M., Goutail, F., Graves, R., Griesfeller, A., Grossmann, K., Hemerijckx, G., Hendrick, F., Herman, J., Hermans, C., Irie, H., Johnston, P. V., Kanaya, Y., Kreher, K., Leigh, R., Merlaud, A., Mount, G. H., Navarro, M., Oetjen, H., Pazmino, A., Perez-Camacho, M., Peters, E., Pinardi, G., Puentedura, O., Richter, A., Schönhardt, A., Shaiganfar, R., Spinei, E., Strong, K., Takashima, H., Vlemmix, T., Vrekoussis, M., Wagner, T., Wittrock, F., Yela, M., Yilmaz, S., Boersma, F., Hains, J., Kroon, M., Piters, A., and Kim, Y. J.: Intercomparison of slant column measurements of NO_2 and O_4 by MAX-DOAS and zenith-sky UV and visible spectrometers, Atmospheric Measurement Techniques, 3, 1629–1646, doi:10.5194/amt-3-1629-2010, 2010.

Rothman, L., Gordon, I., Barber, R., Dothe, H., Gamache, R., Goldman, A., Perevalov, V., Tashkun, S., and Tennyson, J.: HITEMP, the high-temperature molecular spectroscopic database, Journal of Quantitative Spectroscopy and

Radiative Transfer, 111, 2139–2150, doi:https://doi.org/10.1016/j.jqsrt.2010.05.001, 2010.

Sanders, R. W., Solomon, S., Mount, G. H., Bates, M. W., and Schmeltekopf, A. L.: Visible spectroscopy at McMurdo Station, Antarctica: 3. Observations of NO$_3$, Journal of Geophysical Research: Atmospheres, 92, 8339–8342, doi:10.1029/JD092iD07p08339, 1987.

Sarkissian, A., Pommereau, J. P., and Goutail, F.: Identification of polar stratospheric clouds from the ground by visible spectrometry, Geophysical Research Letters, 18, 779–782, doi:10.1029/91GL00769, 1991.

Sasano, Y., Suzuki, M., Yokota, T., and Kanzawa, H.: Improved limb atmospheric spectrometer (ILAS) project: ILAS instrument, performance, and validation plan, in: Advanced and Next-Generation Satellites, edited by Fujisada, H. and Sweeting, M. N., vol. 2583, pp. 193–204, International Society for Optics and Photonics, SPIE, doi:10.1117/12.228564, URL `https://doi.org/10.1117/12.228564`, 1995.

Schäfer, K., Thomas, W., Peters, A., Ries, L., Obleitner, F., Schnelle-Kreis, J., Birmili, W., Diemer, J., Fricke, W., Junkermann, W., Pitz, M., Emeis, S., Forkel, R., Suppan, P., Flentje, H., Gilge, S., Wichmann, H. E., Meinhardt, F., Zimmermann, R., Weinhold, K., Soentgen, J., Münkel, C., Freuer, C., and Cyrys, J.: Influences of the 2010 Eyjafjallajökull volcanic plume on air quality in the northern Alpine region, Atmospheric Chemistry and Physics, 11, 8555–8575, doi:10.5194/acp-11-8555-2011, URL `https://www.atmos-chem-phys.net/11/8555/2011/`, 2011.

Schiller, C., Wahner, A., Platt, U., Dorn, H.-P., Callies, J., and Ehhalt, D. H.: Near UV atmospheric absorption measurements of column abundances during Airborne Arctic Stratospheric Expedition, January–February 1989: 2. OClO observations, Geophysical Research Letters, 17, 501–504, doi:10.1029/GL017i004p00501, 1990.

Schütz, L., Jaenicke, R., and Pietrek, H.: Saharan dust transport over the North Atlantic Ocean, Geological Society of America Special Papers, 186, 87–100, doi:10.1130/SPE186-p87, 1981.

Seinfeld, J. H. and Pandis, S. N.: Atmospheric chemistry and physics: from air pollution to climate change, John Wiley & Sons, 2016.

Serdyuchenko, A., Gorshelev, V., Weber, M., Chehade, W., and Burrows, J. P.: High spectral resolution ozone absorption cross-sections — Part 2: Temperature dependence, Atmospheric Measurement Techniques, 7, 625–636, doi: 10.5194/amt-7-625-2014, 2014.

Shettle, E.: Models of aerosols, clouds and precipitation for atmospheric propagation studies, paper presented at Conference on Atmospheric Propagation in the UV, Visible, IR and MM-Region and Related System Aspects, NATO Adv. Group for Aerosp, Res. and Dev., Copenhagen, 1989.

Sigrist, M. W., Winefordner, J. D., Kolthoff, I., et al.: Air monitoring by spectroscopic techniques, vol. 127, John Wiley & Sons, 1994.

Sinreich, R., Frieß, U., Wagner, T., and Platt, U.: Multi axis differential optical absorption spectroscopy (MAX-DOAS) of gas and aerosol distributions, Faraday Discussions, 130, 153, doi:10.1039/b419274p, 2005.

Sinreich, R., Merten, A., Molina, L., and Volkamer, R.: Parameterizing radiative transfer to convert MAX-DOAS dSCDs into near-surface box-averaged mixing ratios, Atmospheric Measurement Techniques, 6, 1521–1532, doi:10.5194/amt-6-1521-2013, URL https://www.atmos-meas-tech.net/6/1521/2013/, 2013.

Sioris, C. E. and Evans, W. F.: Filling in of Fraunhofer and gas-absorption lines in sky spectra as caused by rotational Raman scattering, Applied optics, 38, 2706–2713, 1999.

Solomon, S., Mount, G. H., Sanders, R. W., and Schmeltekopf, A. L.: Visible spectroscopy at McMurdo Station, Antarctica: 2. Observations of OClO, Journal of Geophysical Research: Atmospheres, 92, 8329–8338, doi:10.1029/JD092iD07p08329, 1987a.

Solomon, S., Schmeltekopf, A. L., and Sanders, R. W.: On the interpretation of zenith sky absorption measurements, Journal of Geophysical Research: Atmospheres, 92, 8311–8319, doi:10.1029/JD092iD07p08311, 1987b.

Solomon, S., Miller, H. L., Smith, J. P., Sanders, R. W., Mount, G. H., Schmeltekopf, A. L., and Noxon, J. F.: Atmospheric NO_3: 1. Measurement technique and the annual cycle at 40°N, Journal of Geophysical Research: Atmospheres, 94, 11 041–11 048, doi:10.1029/JD094iD08p11041, 1989a.

Solomon, S., Sanders, R. W., Carroll, M. A., and Schmeltekopf, A. L.: Visible and near-ultraviolet spectroscopy at McMurdo Station, Antarctica: 5. Observations of the diurnal variations of BrO and OClO, Journal of Geophysical Research: Atmospheres, 94, 11393–11403, doi:10.1029/JD094iD09p11393, 1989b.

Spurr, R.: LIDORT and VLIDORT: linearized pseudo-spherical scalar and vector discrete ordinate radiative transfer models for use in remote sensing retrieval problems, Light scattering reviews, 3, 229–275, 2008.

Spurr, R., Kurosu, T., and Chance, K.: A linearized discrete ordinate radiative transfer model for atmospheric remote-sensing retrieval, Journal of Quantitative Spectroscopy and Radiative Transfer, 68, 689–735, doi:https://doi.org/10.1016/S0022-4073(00)00055-8, URL http://www.sciencedirect.com/science/article/pii/S0022407300000558, 2001.

Stamnes, K., Tsay, S.-C., Wiscombe, W., and Jayaweera, K.: Numerically stable algorithm for discrete-ordinate-method radiative transfer in multiple scattering and emitting layered media, Applied optics, 27, 2502–2509, 1988.

Stutz, J. and Platt, U.: Numerical analysis and estimation of the statistical error of differential optical absorption spectroscopy measurements with least-squares methods, Appl. Opt., 35, 6041–6053, doi:10.1364/AO.35.006041, URL http://ao.osa.org/abstract.cfm?URI=ao-35-30-6041, 1996.

Thalman, R. and Volkamer, R.: Temperature dependent absorption cross-sections of O_2-O_2 collision pairs between 340 and 630 nm and at atmospherically relevant pressure, Phys. Chem. Chem. Phys., 15, 15371–15381, doi:10.1039/C3CP50968K, 2013.

Toledano, C., Wiegner, M., Garhammer, M., Seefeldner, M., Gasteiger, J., Müller, D., and Koepke, P.: Spectral aerosol optical depth characterization of desert dust during SAMUM 2006, Tellus B, 61, 216–228, doi:10.1111/j.1600-0889.2008.00382.x, 2009.

Toledano, C., Wiegner, M., Gro, S., Freudenthaler, V., Gasteiger, J., Müller, D., Müller, T., Schladitz, A., Weinzierl, B., Torres, B., et al.: Optical properties of aerosol mixtures derived from sun-sky radiometry during SAMUM-2, Tellus B, 63, 635–648, doi:10.1111/j.1600-0889.2011.00573.x, URL https://onlinelibrary.wiley.com/doi/abs/10.1111/j.1600-0889.2011.00573.x, 2011.

Tsai, F., Tu, J.-Y., Hsu, S.-C., and Chen, W.-N.: Case study of the Asian dust and pollutant event in spring 2006: Source, transport, and contribution to Taiwan, Science of The Total Environment, 478, 163–174, doi:http://dx.doi.org/10.1016/j.scitotenv.2014.01.072, 2014.

Valavanidis, A., Fiotakis, K., and Vlachogianni, T.: Airborne Particulate Matter and Human Health: Toxicological Assessment and Importance of Size and Composition of Particles for Oxidative Damage and Carcinogenic Mechanisms, Journal of Environmental Science and Health, Part C, 26, 339–362, doi:10.1080/10590500802494538, 2008.

van de Hulst, H.: Multiple light scattering. Tables, formulas and applications, New York: Academic Press, 1980.

van der A, R. J., Eskes, H. J., Boersma, K. F., van Noije, T. P. C., Van Roozendael, M., De Smedt, I., Peters, D. H. M. U., and Meijer, E. W.: Trends, seasonal variability and dominant NO_x source derived from a ten year record of NO_2 measured from space, Journal of Geophysical Research: Atmospheres, 113, doi:10.1029/2007JD009021, 2008.

Van Roozendael, M., Soebijanta, V., Fayt, C., and Lambert, J.: Investigation of DOAS issues affecting the accuracy of the GDP version 3.0 total ozone product, ERS-2 GOME GDP, 3, 97–129, 2002.

Van Roozendael, M., Loyola, D., Spurr, R., Balis, D., Lambert, J.-C., Livschitz, Y., Valks, P., Ruppert, T., Kenter, P., Fayt, C., et al.: Ten years of GOME/ERS-2 total ozone data—The new GOME data processor (GDP) version 4: 1. Algorithm description, Journal of Geophysical Research: Atmospheres, 111, 2006.

Vandaele, A., Hermans, C., and Fally, S.: Fourier transform measurements of SO_2 absorption cross sections: II.: Temperature dependence in the 29 000–44 000cm^{-1} (227–345 nm) region, Journal of Quantitative Spectroscopy and Radiative Transfer, 110, 2115–2126, doi:https://doi.org/10.1016/j.jqsrt.2009.05.006, URL `http://www.sciencedirect.com/science/article/pii/S0022407309001800`, 2009.

Vandaele, A. C., Hermans, C., Simon, P. C., Carleer, M., Colin, R., Fally, S., Merienne, M.-F., Jenouvrier, A., and Coquart, B.: Measurements of the NO_2

absorption cross-section from 42 000 cm^{-1} to 10 000 cm^{-1} (238–1000 nm) at 220 K and 294 K, Journal of Quantitative Spectroscopy and Radiative Transfer, 59, 171–184, 1998.

Vaughan, G., Roscoe, H. K., Bartlett, L. M., O'Connor, F. M., Sarkissian, A., Van Roozendael, M., Lambert, J.-C., Simon, P. C., Karlsen, K., Kåstad Høiskar, B. A., Fish, D. J., Jones, R. L., Freshwater, R. A., Pommereau, J.-P., Goutail, F., Andersen, S. B., Drew, D. G., Hughes, P. A., Moore, D., Mellqvist, J., Hegels, E., Klupfel, T., Erle, F., Pfeilsticker, K., and Platt, U.: An intercomparison of ground-based UV-visible sensors of ozone and NO$_2$, Journal of Geophysical Research: Atmospheres, 102, 1411–1422, doi:10.1029/96JD00515, URL https://agupubs.onlinelibrary.wiley.com/doi/abs/10.1029/96JD00515, 1997.

Veefkind, J., Aben, I., McMullan, K., Förster, H., De Vries, J., Otter, G., Claas, J., Eskes, H., De Haan, J., Kleipool, Q., et al.: TROPOMI on the ESA Sentinel-5 Precursor: A GMES mission for global observations of the atmospheric composition for climate, air quality and ozone layer applications, Remote sensing of environment, 120, 70–83, 2012.

Venables, D. S., Gherman, T., Orphal, J., Wenger, J. C., and Ruth, A. A.: High sensitivity in situ monitoring of NO$_3$ in an atmospheric simulation chamber using incoherent broadband cavity-enhanced absorption spectroscopy, Environmental science & technology, 40, 6758–6763, 2006.

Vlemmix, T., Piters, A. J. M., Berkhout, A. J. C., Gast, L. F. L., Wang, P., and Levelt, P. F.: Ability of the MAX-DOAS method to derive profile information for NO$_2$: can the boundary layer and free troposphere be separated?, Atmospheric Measurement Techniques, 4, 2659–2684, doi:10.5194/amt-4-2659-2011, URL https://www.atmos-meas-tech.net/4/2659/2011/, 2011.

Vlemmix, T., Hendrick, F., Pinardi, G., De Smedt, I., Fayt, C., Hermans, C., Piters, A., Wang, P., Levelt, P., and Van Roozendael, M.: MAX-DOAS observations of aerosols, formaldehyde and nitrogen dioxide in the Beijing area: comparison of two profile retrieval approaches, Atmospheric Measurement Techniques, 8, 941–963, doi:10.5194/amt-8-941-2015, URL https://amt.copernicus.org/articles/8/941/2015/, 2015.

Volkamer, R., Molina, L. T., Molina, M. J., Shirley, T., and Brune, W. H.: DOAS measurement of glyoxal as an indicator for fast VOC chemistry in urban air, Geophysical Research Letters, 32, doi: 10.1029/2005GL022616, URL https://agupubs.onlinelibrary.wiley.com/doi/abs/10.1029/2005GL022616, 2005a.

Volkamer, R., Spietz, P., Burrows, J., and Platt, U.: High-resolution absorption cross-section of glyoxal in the UV–Vis and IR spectral ranges, Journal of Photochemistry and Photobiology A: Chemistry, 172, 35–46, doi:http://dx.doi.org/10.1016/j.jphotochem.2004.11.011, 2005b.

Wagner, T., von Friedeburg, C., Wenig, M., Otten, C., and Platt, U.: UV-visible observations of atmospheric O_4 absorptions using direct moonlight and zenith-scattered sunlight for clear-sky and cloudy sky conditions, Journal of Geophysical Research: Atmospheres, 107, AAC 3–1–AAC 3–15, doi:10.1029/2001JD001026, 2002.

Wagner, T., Dix, B., Friedeburg, C. v., Fries, U., Sanghavi, S., Sinreich, R., and Platt, U.: MAX-DOAS O_4 measurements: A new technique to derive information on atmospheric aerosols—Principles and information content, Journal of Geophysical Research: Atmospheres, 109, doi:10.1029/2004JD004904, 2004.

Wagner, T., Burrows, J. P., Deutschmann, T., Dix, B., von Friedeburg, C., Frieß, U., Hendrick, F., Heue, K.-P., Irie, H., Iwabuchi, H., Kanaya, Y., Keller, J., McLinden, C. A., Oetjen, H., Palazzi, E., Petritoli, A., Platt, U., Postylyakov, O., Pukite, J., Richter, A., van Roozendael, M., Rozanov, A., Rozanov, V., Sinreich, R., Sanghavi, S., and Wittrock, F.: Comparison of box-air-mass-factors and radiances for Multiple-Axis Differential Optical Absorption Spectroscopy (MAX-DOAS) geometries calculated from different UV/visible radiative transfer models, Atmospheric Chemistry and Physics, 7, 1809–1833, doi:10.5194/acp-7-1809-2007, URL https://www.atmos-chem-phys.net/7/1809/2007/, 2007.

Wagner, T., Deutschmann, T., and Platt, U.: Determination of aerosol properties from MAX-DOAS observations of the Ring effect, Atmospheric Measurement Techniques, 2, 495–512, doi:10.5194/amt-2-495-2009, 2009.

Wagner, T., Beirle, S., Brauers, T., Deutschmann, T., Frieß, U., Hak, C., Halla, J. D., Heue, K. P., Junkermann, W., Li, X., Platt, U., and Pundt-Gruber, I.:

Inversion of tropospheric profiles of aerosol extinction and HCHO and NO_2 mixing ratios from MAX-DOAS observations in Milano during the summer of 2003 and comparison with independent data sets, Atmospheric Measurement Techniques, 4, 2685–2715, doi:10.5194/amt-4-2685-2011, URL `https://www.atmos-meas-tech.net/4/2685/2011/`, 2011.

Wagner, T., Apituley, A., Beirle, S., Dörner, S., Friess, U., Remmers, J., and Shaiganfar, R.: Cloud detection and classification based on MAX-DOAS observations, Atmospheric Measurement Techniques, 7, 1289–1320, doi:10.5194/amt-7-1289-2014, 2014.

Wagner, T., Beirle, S., Remmers, J., Shaiganfar, R., and Wang, Y.: Absolute calibration of the colour index and O_4 absorption derived from Multi AXis (MAX-)DOAS measurements and their application to a standardised cloud classification algorithm, Atmospheric Measurement Techniques, 9, 4803–4823, doi:10.5194/amt-9-4803-2016, 2016.

Wagner, T., Beirle, S., Benavent, N., Bösch, T., Chan, K. L., Donner, S., Dörner, S., Fayt, C., Frieß, U., García-Nieto, D., Gielen, C., González-Bartolome, D., Gomez, L., Hendrick, F., Henzing, B., Jin, J. L., Lampel, J., Ma, J., Mies, K., Navarro, M., Peters, E., Pinardi, G., Puentedura, O., Pukite, J., Remmers, J., Richter, A., Saiz-Lopez, A., Shaiganfar, R., Sihler, H., Van Roozendael, M., Wang, Y., and Yela, M.: Is a scaling factor required to obtain closure between measured and modelled atmospheric O_4 absorptions? An assessment of uncertainties of measurements and radiative transfer simulations for 2 selected days during the MAD-CAT campaign, Atmospheric Measurement Techniques, 12, 2745–2817, doi:10.5194/amt-12-2745-2019, URL `https://www.atmos-meas-tech.net/12/2745/2019/`, 2019.

Wahner, A., Callies, J., Dorn, H.-P., Platt, U., and Schiller, C.: Near UV atmospheric absorption measurements of column abundances during Airborne Arctic Stratospheric Expedition, January – February 1989: 1. Technique and NO_2 observations, Geophysical Research Letters, 17, 497–500, doi:10.1029/GL017i004p00497, 1990.

Wang, S.: Study on the retrieval of NO_2 and aerosol pollution in Shanghai urban area based on the passive DOAS technique, Ph.D. thesis, Fudan University, 2012.

Wang, S., Zhao, H., Yang, S., Wang, Z., Zhou, B., and Chen, L.: Correlation between atmospheric O_4 and H_2O absorption in visible band and its implication to dust and haze events in Shanghai, China, Atmospheric Environment, 62, 164–171, doi:https://doi.org/10.1016/j.atmosenv.2012.08.011, URL `http://www.sciencedirect.com/science/article/pii/S1352231012007832`, 2012a.

Wang, S., Zhou, B., Wang, Z., Yang, S., Hao, N., Valks, P., Trautmann, T., and Chen, L.: Remote sensing of NO_2 emission from the central urban area of Shanghai (China) using the mobile DOAS technique, Journal of Geophysical Research: Atmospheres, 117, doi: 10.1029/2011JD016983, URL `https://agupubs.onlinelibrary.wiley.com/doi/abs/10.1029/2011JD016983`, 2012b.

Wang, S., Cuevas, C. A., Frieß, U., and Saiz-Lopez, A.: MAX-DOAS retrieval of aerosol extinction properties in Madrid, Spain, Atmospheric Measurement Techniques, 9, 5089–5101, doi:10.5194/amt-9-5089-2016, 2016.

Wang, T., Hendrick, F., Wang, P., Tang, G., Clémer, K., Yu, H., Fayt, C., Hermans, C., Gielen, C., Müller, J.-F., Pinardi, G., Theys, N., Brenot, H., and Van Roozendael, M.: Evaluation of tropospheric SO_2 retrieved from MAX-DOAS measurements in Xianghe, China, Atmospheric Chemistry and Physics, 14, 11 149–11 164, doi:10.5194/acp-14-11149-2014, URL `https://www.atmos-chem-phys.net/14/11149/2014/`, 2014a.

Wang, Y., Sartelet, K. N., Bocquet, M., Chazette, P., Sicard, M., D'Amico, G., Léon, J. F., Alados-Arboledas, L., Amodeo, A., Augustin, P., Bach, J., Belegante, L., Binietoglou, I., Bush, X., Comerón, A., Delbarre, H., García-Vízcaino, D., Guerrero-Rascado, J. L., Hervo, M., Iarlori, M., Kokkalis, P., Lange, D., Molero, F., Montoux, N., Muñoz, A., Muñoz, C., Nicolae, D., Papayannis, A., Pappalardo, G., Preissler, J., Rizi, V., Rocadenbosch, F., Sellegri, K., Wagner, F., and Dulac, F.: Assimilation of lidar signals: application to aerosol forecasting in the western Mediterranean basin, Atmospheric Chemistry and Physics, 14, 12 031–12 053, doi:10.5194/acp-14-12031-2014, URL `https://www.atmos-chem-phys.net/14/12031/2014/`, 2014b.

Wang, Z., Zhou, B., Wang, S., and Yang, S.: Observation on the spatial distribution of air pollutants by active multi-axis differential optical absorption spectroscopy, Acta Physica Sinica, 60, 60703, doi:10.7498/aps.60.060703, 2011.

Warneck, P.: Chemistry of the natural atmosphere, Second Edition, San Diego: Academic Press, 1999.

Warren, E., Charlton-Perez, C., Kotthaus, S., Lean, H., Ballard, S., Hopkin, E., and Grimmond, S.: Evaluation of forward-modelled attenuated backscatter using an urban ceilometer network in London under clear-sky conditions, Atmospheric Environment, 191, 532–547, doi:https://doi.org/10.1016/j.atmosenv.2018.04.045, URL `http://www.sciencedirect.com/science/article/pii/S1352231018302760`, 2018.

Wenig, M., Spichtinger, N., Stohl, A., Held, G., Beirle, S., Wagner, T., Jähne, B., and Platt, U.: Intercontinental transport of nitrogen oxide pollution plumes, Atmospheric Chemistry and Physics, 3, 387–393, doi:10.5194/acp-3-387-2003, 2003.

Wiegner, M. and Geiß, A.: Aerosol profiling with the Jenoptik ceilometer CHM15kx, Atmospheric Measurement Techniques, 5, 1953–1964, doi:10.5194/amt-5-1953-2012, URL `https://www.atmos-meas-tech.net/5/1953/2012/`, 2012.

Wiegner, M., Groß, S., Freudenthaler, V., Schnell, F., and Gasteiger, J.: The May/June 2008 Saharan dust event over Munich: Intensive aerosol parameters from lidar measurements, Journal of Geophysical Research: Atmospheres, 116, doi:10.1029/2011JD016619, d23213, 2011.

Wiegner, M., Madonna, F., Binietoglou, I., Forkel, R., Gasteiger, J., Geiß, A., Pappalardo, G., Schäfer, K., and Thomas, W.: What is the benefit of ceilometers for aerosol remote sensing? An answer from EARLINET, Atmospheric Measurement Techniques, 7, 1979–1997, doi:10.5194/amt-7-1979-2014, 2014.

Wu, F. C., Xie, P. H., Li, A., Chan, K. L., Hartl, A., Wang, Y., Si, F. Q., Zeng, Y., Qin, M., Xu, J., Liu, J. G., Liu, W. Q., and Wenig, M.: Observations of SO_2 and NO_2 by mobile DOAS in the Guangzhou eastern area during the Asian Games 2010, Atmospheric Measurement Techniques, 6, 2277–2292, doi:10.5194/amt-6-2277-2013, URL `https://www.atmos-meas-tech.net/6/2277/2013/`, 2013.

Xin, J., Wang, Y., Li, Z., Wang, P., Hao, W. M., Nordgren, B. L., Wang, S., Liu, G., Wang, L., Wen, T., Sun, Y., and Hu, B.: Aerosol optical depth (AOD) and

Ångström exponent of aerosols observed by the Chinese Sun Hazemeter Network from August 2004 to September 2005, Journal of Geophysical Research: Atmospheres, 112, doi:10.1029/2006JD007075, 2007.

Zhang, J., Wang, S., Guo, Y., Zhang, R., Qin, X., Huang, K., Wang, D., Fu, Q., Wang, J., and Zhou, B.: Aerosol vertical profile retrieved from ground-based MAX-DOAS observation and characteristic distribution during wintertime in Shanghai, China, Atmospheric Environment, 192, 193–205, doi:https://doi.org/10.1016/j.atmosenv.2018.08.051, URL `http://www.sciencedirect.com/science/article/pii/S1352231018305727`, 2018.

Zhang, Q., Streets, D. G., He, K., Wang, Y., Richter, A., Burrows, J. P., Uno, I., Jang, C. J., Chen, D., Yao, Z., and Lei, Y.: NO_x emission trends for China, 1995–2004: The view from the ground and the view from space, Journal of Geophysical Research: Atmospheres, 112, doi:10.1029/2007JD008684, 2007.

Zhang, Z., Wenig, M., Zhou, W., Diehl, T., Chan, K. L., and Wang, L.: The contribution of different aerosol sources to the Aerosol Optical Depth in Hong Kong, Atmospheric Environment, 83, 145–154, doi:http://dx.doi.org/10.1016/j.atmosenv.2013.10.047, 2014.

Zhu, Y., Kuhlmann, G., Chan, K. L., Donner, S., Schütt, A., Wagner, T., and Wenig, M.: Citywide Measurements of NO_2 Concentrations in Munich Using a Combination of Mobile and Stationary Spectroscopic Measurement Techniques, in: Light, Energy and the Environment, p. HM4E.4, Optical Society of America, doi:10.1364/HISE.2016.HM4E.4, URL `http://www.osapublishing.org/abstract.cfm?URI=HISE-2016-HM4E.4`, 2016.

Zieger, P., Weingartner, E., Henzing, J., Moerman, M., de Leeuw, G., Mikkilä, J., Ehn, M., Petäjä, T., Clémer, K., van Roozendael, M., Yilmaz, S., Frieß, U., Irie, H., Wagner, T., Shaiganfar, R., Beirle, S., Apituley, A., Wilson, K., and Baltensperger, U.: Comparison of ambient aerosol extinction coefficients obtained from in-situ, MAX-DOAS and LIDAR measurements at Cabauw, Atmospheric Chemistry and Physics, 11, 2603–2624, doi:10.5194/acp-11-2603-2011, URL `https://acp.copernicus.org/articles/11/2603/2011/`, 2011.